Centre Énergie Matériaux Télécommunications

METAL ORGANIC FRAMEWORK DERIVATIVE PHOTOELECTRODES FOR EFFICIENT WATER SPLITTING

Par

Li Shi

Thèse présentée pour l'obtention

du grade de Philosophiae Doctor (Ph.D.)

en sciences de l'énergie et des matériaux

Jury d'évaluation

Président du jury et examinateur interne	Professeur Shuhui Sun INRS-ÉMT, Université du Québec
Examinateur externe	Professeur Pablo Bianucci Concordia University
Examinateur externe	Professeur Jean-Michel Nunzi Queen's University
Directeur de recherche	Professeur Federico Rosei INRS-ÉMT, Université du Québec
Codirecteur de recherche	Professeur François Légaré INRS-ÉMT, Université du Québec
Codirecteur de recherche	Professeur Qin Wei University of Jinan

ACKNOWLEDGEMENTS

First of all, becoming a scientist is a significant part of my lifetime dream and I really appreciate my supervisor, Prof. Federico Rosei, for his continuous support during my Ph.D. study and related research during the past five years. I always received the maximum degree of freedom from him for my own ideas as well as enough support and encouragement as a push in the right direction. I still remember the first time we met at INRS. He told me three things: “First, learn some French, that will help you to good communicate with all the technicians here and better live in Montréal; Second, learn some English through reading, not the scientistic research articles, but more literary book; Last, before the paper publish, no matter how much effort you did, there is nothing.” Right now, I can speak and read a little French, which really offers me a lot of conveniences in my daily life. I read the science fiction “A Song of Ice and Fire”, part of “Holy Bible”, and so on. I can understand the meaning of some words better, which I didn’t learn from school. He taught me how to know or judge a problem from a macroscopic perspective. I am extremely grateful for his continuing, unconditional support and for providing me with great opportunities to develop myself, such as attending international conferences, appearing summer school, and competing for various awards. I feel extremely lucky to be his student.

I would also like to extend my gratitude to my group leader, Dr. Daniele Benetti, for his substantial support and guidance throughout my Ph.D. journey. He has always been patient and willing to help, when I was stuck in a problem or could not see the value of my work. He has always perfected and supplemented my raw and immature ideas, making them complete and convincing. He helped me to cope with the challenges of academic research and also the difficulties in life. I have learned so much from him, including the way of thinking, giving credit to people, valuing collaboration and reputation, and communicating ideas effectively. It is my great privilege to have had him as my group leader.

I am indebted to my previous supervisors and teachers. Before I went to Canada, my master supervisor, Prof. Bin Du, told me: “I am not going to ask you publish many papers during your Ph.D., I hope you can learn the way of their thinking and their attitude to the life, these are more important things in your whole life.” He died of liver cancer in 2019, I miss him very much and I hope he can be proud of me. Prof. Qin Wei, Prof. Wei He, Prof. Guozhu Chen and Prof. Dong Wei who brought me to this research field made me start along the path to where I am today. Being able to learn from all my supervisors, group leader and teachers has been my great fortune.

Next, I would like to thank Prof. Pablo Bianucci, Prof. Jean-Michel Nunzi, and Prof. Shuhui Sun for being the members of my thesis committee and offering their precious comments and valuable time.

I would also like to express my appreciations to all my great lab mates from the Groupe-NFL group, Prof. Haiguang Zhao, Prof. Shun Li, Prof. Xin Tong, Prof. Heng Guo, Dr. Wei Huang, Dr. Daling Cui, Dr. Lei Jin, Dr. Chao Wang, Dr. Penghui Ji, Jiabin Liu, Dr. Kanghong Wang, Dr. Min Zhang, Dr. Tingzhou Yang, Dr. Bin Luo, Dr. Selopal Gurpreet Singh, Dr. Fabrizio De Marchi, Dr. Lombardo, Maria Elena, Dr. Fabiola Navarro-Pardo, Xin Liu, Dr. Faying Li, Na Xu, Dr. Omar Abdelkarim et al., I am very honored to be part of such a supportive, hardworking, and inspiring group. I especially thank Kanghong Wang and Jiabin Liu for training me to start my research work in INRS-EMT.

I would like to thank Prof. Andreas Ruediger and Prof. Mohamedi Mohamed for the inspiring classes and presentations given by them. I would like to thank Prof. Daniel Guay, Prof. Marc A. Gauthier, Prof. Ana Tavares, Prof. Fiorenzo Vetrone, Prof. Shuhui Sun, and Prof. Jinyang Liang, for the inspiring conversations with them. I would also like to thank the nice and helpful technicians and administrative staffs in INRS-EMT, especially Christophe Chabanier and Catalin Harnagea. I feel lucky to know a lot of friends to share life and feelings with them during the past years in the INRS-EMT center, particularly, Xianglei Liu, Jiyun Chen, Qingzhe Zhang, Yong Wang, Chen Wang, Ruiqi Yang, Mengyang Fan, Minghui Hao, Qiliang Wei, Fang Dong, Xin Chai, Fan Yang, Pei You, Cheng Jiang, Yang Liu, Hao Yu, Xin Jin, Luca Zanotto, Piotr Roztocki, and many others. I would also like to thank Shanyan Jiang, ShuShu Geng, Qiaochu Ma, Feiyue Wang and Mingyu Wang for the happy dota2 time we shared together. In the last, I would like to thank all my teammates in World of Warcraft, including Jerry-Shi, Ric-Zhang, Quanquan-Jiayi Zhang, Susoo, SaSa, and Aoman-Yu Chen, who made me the top Guardian Druid in (US) Illidan.

I am also very grateful to Jean-Philippe Masse, Gwenaël Chamoulaud, Daniel Chartrand, Olivier Schott, and Galyna Shul, who provided massive help and support in the characterizations of my samples.

Last but not least, special thanks to my family, words cannot express how grateful I am to my mother and father, and all the family members for their unconditional love, understanding, and support during my life. I would like to thank Yuting Lei for the time and company. They never show up in any of my work or contribution, but it is really them who make me stand as who I am. Throughout the past five years, many people have contributed to the completion of this thesis. I apologize in advance if I forgot to mention you among the people that I am grateful to. I am very appreciative of those who are reading these lines. In the last, I would like to share a sentence I read in one paper: “The achievement stayed in the past, but the discovery leads to the future.

ABSTRACT

Water splitting via photoelectrochemical (PEC) technology is an eco-friendly and sustainable way to produce hydrogen. Semiconductor materials as the central components in PEC water splitting cells have decisive influences on the device's solar-to-hydrogen conversion efficiency. As the most common used semiconductor, metal oxide (MO) has received a lot of attention due to its outstanding (photo)-electrochemical stability, low cost, favorable band edge positions, and wide distribution of bandgaps. Despite exhibiting these attractive characteristics, its application in PEC water splitting still suffered from its instinct drawbacks, such as disorderliness and nonuniform, which are severely limited to the efficiency and performance of the PEC system. However, traditional MO synthetic methods fall short in improving these characteristics. Therefore, developing a new MO synthetic method is really urgent, which will readily provide stable porous architectures, controlled phase, as well as useful control over dimensions (1-D, 2-D, and 3-D) of the MO for enhancing their performance and efficiency in water splitting applications. As emerging crystalline porous organic-inorganic hybrid materials, metal organic framework (MOF) has been widely used as sacrificial precursors for the synthesis of MO due to their composites with tunable and controllable nanostructures and chemical compositions. In this thesis, we developed a number of MO-based photoelectrodes via MOF-template method and evaluated their performance in PEC water splitting hydrogen generation.

Titanium dioxide (TiO_2) became one of the most extensively investigated MO semiconductor for PEC water splitting since 1972. However, the control of its phase alignment and the interface structure to improve the PEC performance remains a challenge. Hence, a mixed-phase TiO_2 with octahedral structure was synthesized via MOF as sacrificial template. This method allowed us to obtain a controlled mixed-phase of TiO_2 nanoparticles in one step via solid-state pyrolysis at a specific temperature, while simultaneously retaining the MOF crystal morphology. After sensitization with core@shell CdSe@CdS quantum dots (QDs), the photoanode exhibits efficient and stable PEC performance. Compared to commercial TiO_2 film, the MOF-derived TiO_2 film sensitized with core-shell CdSe@CdS QDs showed an enhanced PEC device stability of +42.1% and PEC performance of +47.6%. This is because the presence of the mixed-phase will contribute to promoting charge separation and suppresses charge recombination inside TiO_2 nanoparticles, even if the 'internal' charge separation due to the rutile/anatase is not directly observable due to ensemble effect that hides the contributions of the single phases.

Secondly, research on photoanodes for PEC architectures is flourishing, while research on photocathode materials is far behind. This situation creates a major bottleneck for the development of highly efficient overall PEC water splitting system. Therefore, we designed a facile synthetic strategy to engineer NiO

photocathode by using nickel-based MOF (Ni-MOF). By this method, we could obtain hierarchical hollow NiO/carbon nanostructure that can be employed as the mesoporous layer of a photocathode. After sensitization with metal chalcogenide QDs, the optimized photocathode exhibited a photocurrent density of -93.6·μA cm^{-2} at 0 V vs. RHE (reversible hydrogen electrode). This value is obtained at neutral pH (6.8) and without any sacrificial reagent, cocatalyst, or molecular linker. Compared with pure NiO, the enhancement is almost three-fold. In addition, the presence of core@shell QDs resulted in an increase of more than 80% in photocurrent compared to single QDs (CdSe). We further investigated the mechanism that underlies this photocurrent enhancement. We found that the superior performance can be jointly attributed to the high surface area for loading sensitizers, light scattering of the nanohybrid, as well as the presence of a carbon matrix that conducts electrons rapidly.

Thirdly, in order to avoid the heavy metal QDs and use the solar energy in a more environmentally friendly way, a MOF-on-MOF heterostructure was designed as the precursor to synthesize In_2O_3/CuO p-n heterojunction composite for PEC water splitting. By incorporation of small amounts of graphene nanoribbons (GNRs) in In_2O_3/CuO (In_2O_3/CuO-GNRs) photoanode, the designed film exhibited an enhanced efficiency for PEC H_2 generation. The optimized device based on the In_2O_3/CuO-0.03 wt% GNRs photoanode exhibited a remarkable photocurrent density as high as 1.51·mA cm^{-2} at 1.6 V vs RHE under one sun illumination, which is 70% higher than the device based on pure In_2O_3/CuO photoanode (0.89·mA cm^{-2}) and good stability as long as 5 hours. The improvement in the performance of this hybrid anodes is not only due to the p-n heterojunction promotes the separation efficiency of photogenerated electron-hole pairs and suppressed charge recombination, but also the incorporation of GNRs offers better path for electron transport (reduces charge transfer resistance).

Keywords: photoelectrochemical, hydrogen generation, phase/hetero-junction, metal organic framework, metal oxide, quantum dots, photoelectrode, water splitting

RÉSUMÉ

La séparation de l'eau par la technologie photoélectrochimique (PEC) est un moyen écologique et durable de produire de l'hydrogène. Les matériaux semi-conducteurs, en tant que composants centraux des cellules de fractionnement de l'eau PEC, ont une influence décisive sur l'efficacité de la conversion solaire-hydrogène du dispositif. En tant que semi-conducteur le plus courant, l'oxyde métallique (MO) a fait l'objet d'une grande attention en raison de sa remarquable stabilité (photo)-électrochimique, de son faible coût, de la position favorable de ses bords de bande et de la large distribution de ses bandes interdites. Malgré ces caractéristiques attrayantes, son application dans la séparation de l'eau PEC souffre toujours de ses inconvénients intrinsèques, tels que le désordre et la non-uniformité, qui limitent sérieusement l'efficacité et les performances du système PEC. Cependant, les méthodes traditionnelles de synthèse de la MO ne parviennent pas à améliorer ces caractéristiques. Par conséquent, il est vraiment urgent de développer une nouvelle méthode de synthèse de MO, qui fournira facilement des architectures poreuses stables, une phase contrôlée, ainsi qu'un contrôle utile des dimensions (1-D, 2-D et 3-D) de la MO pour améliorer leurs performances et leur efficacité dans les applications de séparation de l'eau. En tant que matériaux hybrides organiques-inorganiques cristallins émergents, les cadres métallo-organiques (MOF) ont été largement utilisés comme précurseurs sacrificiels pour la synthèse de MO en raison de leurs composites aux nanostructures et compositions chimiques accordables et contrôlables. Dans cette thèse, nous avons développé un certain nombre de photoélectrodes à base de MO par la méthode du modèle MOF et évalué leurs performances dans la génération d'hydrogène par séparation d'eau PEC.

Le dioxyde de titane (TiO_2) est devenu l'un des semi-conducteurs MO les plus étudiés pour la séparation de l'eau PEC depuis 1972. Cependant, le contrôle de l'alignement de ses phases et de la structure de l'interface pour améliorer les performances de la PEC reste un défi. Par conséquent, un TiO_2 à phases mixtes avec une structure octaédrique a été synthétisé via un MOF comme modèle sacrificiel. Cette méthode nous a permis d'obtenir une phase mixte contrôlée de nanoparticules de TiO_2 en une seule étape par pyrolyse à l'état solide à une température spécifique, tout en conservant simultanément la morphologie cristalline du MOF. Après sensibilisation avec des points quantiques (QDs) CdSe@CdS core@shell, la photoanode présente une génération d'hydrogène solaire efficace et stable. Comparé aux films de TiO_2 commerciaux, le film de TiO_2 dérivé du MOF sensibilisé par des QDs CdSe@CdS core-shell, a montré une meilleure stabilité du dispositif PEC de +42,1% et une performance PEC de +47,6%. Cela est dû au fait que la présence de la phase mixte contribue à promouvoir la séparation des charges et supprime la recombinaison des charges entre les nanoparticules de TiO_2, même si la séparation des charges " interne " due au rutile/anatase n'est pas directement observable en raison de l'effet d'ensemble qui masque les contributions des phases uniques.

Deuxièmement, alors que la recherche sur les photanodes pour les architectures PEC est florissante, celle sur les matériaux des photocathodes est loin derrière. Cette situation crée un goulot d'étranglement majeur pour le développement de systèmes PEC hautement efficaces. Nous avons donc conçu une stratégie de synthèse facile pour fabriquer une photocathode en NiO en utilisant des MOF à base de nickel (Ni-MOF) comme modèles sacrificiels. Cette méthode nous a permis d'obtenir des nanostructures creuses hiérarchisées de NiO/carbone qui peuvent être utilisées comme couche mésoporeuse d'une photocathode. Après avoir été sensibilisées avec des QDs de chalcogénures métalliques, les performances PEC optimisées ont présenté une densité de photocourant de -93,6 μA cm^{-2} à 0 V vs RHE (électrode à hydrogène réversible). Cette valeur est obtenue à pH neutre (6,8) et sans aucun réactif sacrificiel, cocatalyseur ou lieur moléculaire. Par rapport au NiO nu, l'amélioration est presque triplée. En outre, la présence de QDs core@shell a entraîné une augmentation de plus de 80 % du photocourant par rapport aux QDs simples (CdSe). Nous avons étudié plus avant le mécanisme qui sous-tend cette augmentation du photocourant. Nous avons découvert que la performance supérieure peut être attribuée conjointement à la surface élevée pour le chargement des sensibilisateurs et la diffusion de la lumière du nanohybride ainsi qu'à la présence d'une matrice de carbone qui conduit rapidement les électrons.

Troisièmement, afin d'éviter les QDs comme sensibilisateur, une hétérostructure MOF-sur-MOF a été conçue comme précurseur pour synthétiser un composite à hétérojonction p-n In_2O_3/CuO pour la séparation de l'eau par PEC. En incorporant de petites quantités de nanorubans de graphène (GNR) dans la photoanode In_2O_3/CuO (In_2O_3/CuO-GNRs), le film synthétisé présente une efficacité accrue pour la génération de H_2 par PEC. Le dispositif optimisé basé sur la photoanode In_2O_3/CuO-GNRs a montré une remarquable densité de photocourant aussi élevée que 1,51 mA cm^{-2} à 1,6 V vs RHE sous une illumination solaire, ce qui est 70% plus élevé que le dispositif basé sur des photoanodes In_2O_3/CuO pures (0,89 mA cm^{-2}) et une bonne stabilité jusqu'à 5 heures. L'amélioration des performances de ces anodes hybrides n'est pas seulement due à l'hétérojonction p-n qui améliore l'efficacité de séparation des paires électron-trou photogénérées et supprime la recombinaison des charges, mais aussi à l'incorporation de GNR qui offre un meilleur chemin pour le transport des électrons (résistance de transfert de charge réduite).

Mots-clés: photoélectrochimique, génération d'hydrogène, phase/hétérojonction, les cadres métallo-organiques, oxydes métalliques, points quantiques, photoélectrode, séparation d'eau

TABLE OF CONTENTS

LIST OF FIGURES

Figure 3.5 XRD patterns of the NH_2-MIL-125(Ti) precursor (a); and that of the M-TiO_2 (red), C-TiO_2 (blue) and M-TiO_2-575 (black) (b) (green triangle: anatase-phase TiO_2; purple dot: rutile-phase TiO_2).

Figure 3.6 (a) Plots of transmittance versus wavelength for FTO, FTO/C-TiO_2 and FTO/M-TiO_2; (b) DRS-UV spectra of C-TiO_2, M-TiO_2, M-TiO_2/CdSe and M-TiO_2/CdSe@CdS; (c) PL spectra of C-TiO_2, M-TiO_2, M-TiO_2/CdSe and M-TiO_2/CdSe@CdS; (d) XRD of CdSe QDs or core@shell CdSe@CdS QDs, the Joint Committee on Powder Diffraction Standards (JCPDS) card files for CdSe (00190191, black for ZB and 08-459, green for WZ) and CdS (01-077-2306, Magenta for WZ) are shown for identification.

Figure 3.7 XPS survey spectra of C-TiO_2 (a) and M-TiO_2 (b); High resolution Ti 2p spectra for (c) C-TiO_2 and (d) M-TiO_2. High resolution O 1s spectra for (e) C-TiO_2 and (f) M-TiO_2.

Figure 3.8 (a) UV adsorption and PL intensity of CdSe and CdSe@CdS; (b) TEM image of CdSe. The inset image exhibits the average size of CdSe; (c) TEM image of CdSe@CdS. The inset image exhibits the average size of CdSe@CdS; (d) CdSe@CdS QDs in the TiO_2 film, highlighted in the circle.

Figure 3.9 (a) Photocurrent density potential dependence of M-TiO_2 and C-TiO_2 sensitized by CdSe and CdSe@CdS; (b) Stability measurements (photocurrent density as a function of time) of M-TiO_2 and C-TiO_2 sensitized by CdSe and CdSe@CdS photoanodes at 0.4 V versus RHE under AM 1.5 G illumination (100 mW/cm^2); (c) Transient PL spectra of ZrO_2/CdSe, C-TiO_2/CdSe, M-TiO_2/CdSe, C-TiO_2/CdSe@CdS and M-TiO_2/CdSe@CdS; (d) Summary of the energy levels obtained from UPS measuraments. The CdSe and CdS energy levels are taken from.

Figure 3.10 All the samples PEC performance under dark, continuous and chopped illumination. (a) C-TiO_2; (b) M-TiO_2; (c) C-TiO_2/CdSe(d) M-TiO_2/CdSe(e) C-TiO_2/CdSe@CdS and (f) M-TiO_2/CdSe@CdS.

Figure 3.11 (a) Photocurrent density potential dependence of M-TiO_2-575/CdSe and (b) IPCE spectra of PEC devices based on M-TiO_2/QDs and C-TiO_2/QDs photoanodes measured at 0.9 V vs RHE under one sun illumination (AM 1.5 G, 100 $mW \cdot cm^{-2}$).

Figure 3.12 The extrapolation of Tauc plots $((\alpha h\nu)^{1/2}$ versus photon energy ($h\nu$)) for the M-TiO_2 and C-TiO_2 films (a); High binding energy cut-off (b) and low binding energy cut-off (c) of UPS spectra of M-TiO_2 and C-TiO_2.

Figure 3.13 (a) EIS Nyquist plots of all samples and (b) The magnified EIS spectra of M-TiO_2/CdSe@CdS, M-TiO_2/CdSe, C-TiO_2/CdSe@CdS, C-TiO_2/CdSe and the inset is the equivalent circuit diagram.

Figure 5.17 Raman spectra of bare GNRs (red line), In_2O_3/CuO composite (blue line), and In_2O_3/CuO-GNRs hybrid mesoporous film (cyan line).

Figure 5.18 Plain-view and cross-sectional SEM image of In_2O_3/CuO-0.03 wt% GNRs (a and b); EDS mapping analysis of all the elements in relevant In_2O_3/CuO-0.03 wt% GNRs electrode including (c) In, (d) Cu, (e) O, and (f) C.

Figure 5.19 Photocurrent density-potential curves of PEC devices based on In_2O_3/CuO-GNRs hybrid photoanodes with different concentrations of GNRs under dark, continuous and chopped illumination (AM 1.5G, 100 $mW \cdot cm^{-2}$): (a) 0.00 wt%;(b) 0.01 wt%; (c) 0.02 wt%; (d) 0.03 wt%; (e) 0.04 wt% and (f) 0.05 wt%. (g) Variation of current density at 1.6 V vs. RHE under $100 \cdot mW \cdot cm^{-2}$ illumination with the concentration of GNRs.

Figure 5.20 Photocurrent density of (a) In_2O_3 and (b) In_2O_3-0.03 wt% GNRs.

Figure 5.21 (a) Comparative LSV curve of bare In_2O_3, In_2O_3/CuO, and In_2O_3/CuO-0.03 wt% GNRs. (d) chopped illumination of bare In_2O_3, In_2O_3/CuO, and In_2O_3/CuO-0.03 wt% GNRs (Electrolyte 1M NaOH). (b) Nyquist plots of In_2O_3, In_2O_3/CuO composite, and In_2O_3/CuO-0.03 wt% GNRs. (d) Stability measurements (chronoamperometry) of In_2O_3/CuO-0.03 wt% GNRs in NaOH and Na_2SO_4 electrolyte, respectively (All experiments ran at 1.4 V versus RHE under AM 1.5 G illumination (100 mW cm^{-2})).

Figure 5.22 TEM images of the In_2O_3/CuO-0.03 wt% GNRs after the stability test from different directions.

Figure 5.23. H_2 evolution of In_2O_3/CuO-0.03wt GNRs as a function of time at 1.4 V vs RHE under 100 mW/cm^2 illumination with AM 1.5 G filter. The evolution of H_2 exhibits a nearly linear increase over time (solid red curve). H_2 evolution is also calculated from the measured current (solid black curve).

LIST OF TABLES

LIST OF ABBREVIATIONS AND ACRONYMS

0D	Zero-dimensional
1D	One-dimensional
2D	Two-dimensional
3D	Three-dimensional
MOF	Metal organic framework
MO	Metal oxide
MMOs	Mixed metal oxide
PEC	Photoelectrochemical
CB	Conduction band
VB	Valance Band
DMF	*N*,*N*-dimethylformamide
EDX	Energy dispersive X-ray spectroscopy
QDs	Quantum dots
GNRs	Graphene nanoribbons
TW	Terawatts
H_2	Hydrogen
N_2	Nitrogen
Ar	Argon
PVs	Photovoltaics
CO_2	Carbon dioxide
MB	Methylene blue
E_F	Fermi Level
E_g	Bandgap energy
ΔG^0	Gibbs free energy change

NHE	Normal hydrogen electrode
RHE	Reversible hydrogen electrode
P25	Evonik-Degussa Aeroxide TiO_2 P25
A/R	Anatase/rutile
NH_2-BDC	2-Amino-1,4-benzenedicarboxylic acid
H_3BTC	1,3,5-benzenetricarboxylic acid
H_2BDC	1,4-benzenedicarboxylic acid
OLA	Oleylamine
ODE	1-octadecene
CdO	Cadmium oxide
TOP	Trioctyl phosphine
TOPO	Trioctyl phosphine oxide
PVP	Polyvinylpyrrolidone
NaOH	Sodium hydroxide
FTO	Fluorine doped tin oxide
TOPT	Titanium isopropoxide
DI	Deionized
C	Carbon
P	Phosphorus
N	Nitrogen
S	Sulfur
Se	Selenium
DC	Direct current
EPD	Electrophoretic deposition
CBD	Chemical bath deposition
IPCE	Incident photon-to-current efficiency

EIS	Electrochemical impedance spectroscopy
SEM	Scanning electron microscope
TEM	Transmission electron microscopy
UPS	Ultraviolet photoelectron spectroscopy
UV	Ultraviolet
XPS	X-ray photoelectron spectroscopy
PL	Photoluminescence
XRD	X-ray diffraction
GC	Gas chromatography
TCD	Thermal conductivity detector
GC	Gas chromatography
SILAR	Successive ionic layer adsorption and reaction
JCPDS	Joint committee on powder diffraction standards
$\eta_{Faradaic}$	Faradaic efficiency
BET	Brunauer-Emmett-Teller
DSSCs	Dye-sensitized solar cells
OCP	Open circuit potential
LSV	Linear sweep voltammetry
J_{ph}	Photocurrent density
TGA	Thermogravimetric analysis
HAADF-STEM	High-angle annular dark-field scanning transmission electron microscope

1 INTRODUCTION

1.1 General background

Since the industrial revolution, our lives are crucially dependent on energy and currently the dominant source of global energy is mainly supplied by carbon-based fossil fuels (~79%), e.g., petroleum, natural gas, and coal[1]. Figure 1.1 illustrates the world total primary energy consumption by only commercially-traded fuels in 2020, with 79% of net-emission fossil fuels including 11% of coal, 37% of petroleum, and 31% of natural gas, respectively. Forecasts predict that in 2050 the worldwide energy consumption will be 25-27 Terawatts, 10^{12}W, (TW), over 80% of which will still depend on fossil fuels. However, they are neither renewable nor sustainable, and will emit greenhouse gases (such as methane, carbon dioxide, and nitrous oxide) in large quantities during the combustion process. This can result in weather changes, severe health problems, sea-level rise, and changes in the ecosystem[2, 3]. Owing to the excessive using of fossil fuels, ever-increasing environmental issues, and a globally growing population, the seeking of green and renewable energy sources is imperative and urgent.

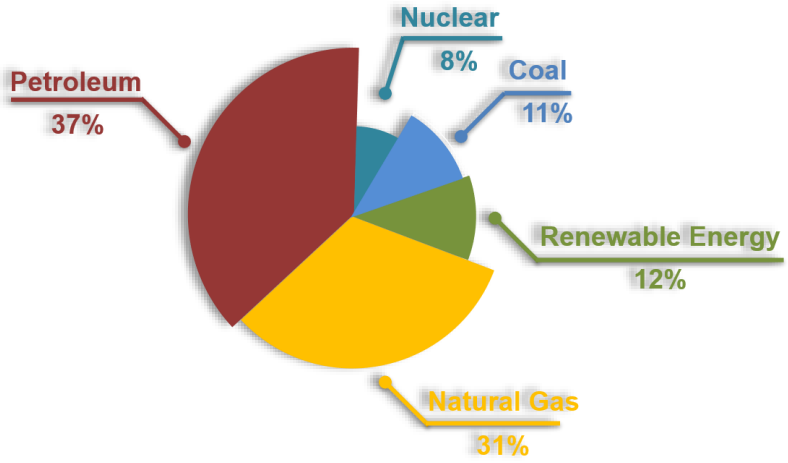

Figure 1.1 The world total primary energy supply by fuels in 2022. The data is collected from Our World in Data, Enerdata, OECD iLibrary.

Because of unmatched resource potential, solar energy utilization has been the subject of intense research, development, and deployment efforts that have accelerated during the past decade[4]. The sun irradiance reaching the Earth is plentiful enough to fulfill the humankind's energy consumption more than ten thousand times over (120 PW (Petawatts, 10^{15}W) strikes the surface of the Earth, out of which 36 PW is on land)[5, 6]. Efforts have focused on developing photovoltaics (PVs) for the production of electricity,

converting solar energy into electricity or heat, and developing artificial photosynthetic systems that directly produce fuels from sunlight.

Hydrogen (H_2), sitting at the top of the periodic table, offers an alternative energy source with several benefits. It contains more energy per unit of weight than fossil fuels and in particular, which can release energy either through direct combustion or in a hydrogen fuel cell with the only by-product being water as well as the emissions-free of CO_2 and other toxic gases. 1 kg of hydrogen (kg/H_2) contains 33.33 kWh (kilowatt hour (kWh)) of usable energy, whereas the traditional fossil fuels, like petrol and diesel, only hold about 12 kWh/kg[7]. In achieving net-zero emissions, hydrogen is a powerful enabler and vital component, however, it will require investment and a large scaling up of its production and use to reduce costs to make it viable. Moreover, hydrogen is versatile and can be used in many modern chemical processes, such as the Fischer-Tropsch reaction and ammonia synthesis (Haber-Bosch reaction)[8]. However, up to 96% of the hydrogen used in the world is derived from steam reforming of huge amounts of hydrocarbons (e.g., methane), and only about 4% of the hydrogen is produced from water decomposition[9, 10]. Even though steam reforming is currently the cheapest way to produce hydrogen, the large quantities of CO_2 emissions prevent a significant increase in this production technology. Therefore, the efficient and sustainable generation of hydrogen is necessary for the development of a sustainable society. Figure 1.2 highlights various avenues for producing hydrogen, derived from carbon systems, through renewable sources, and finally to nuclear.

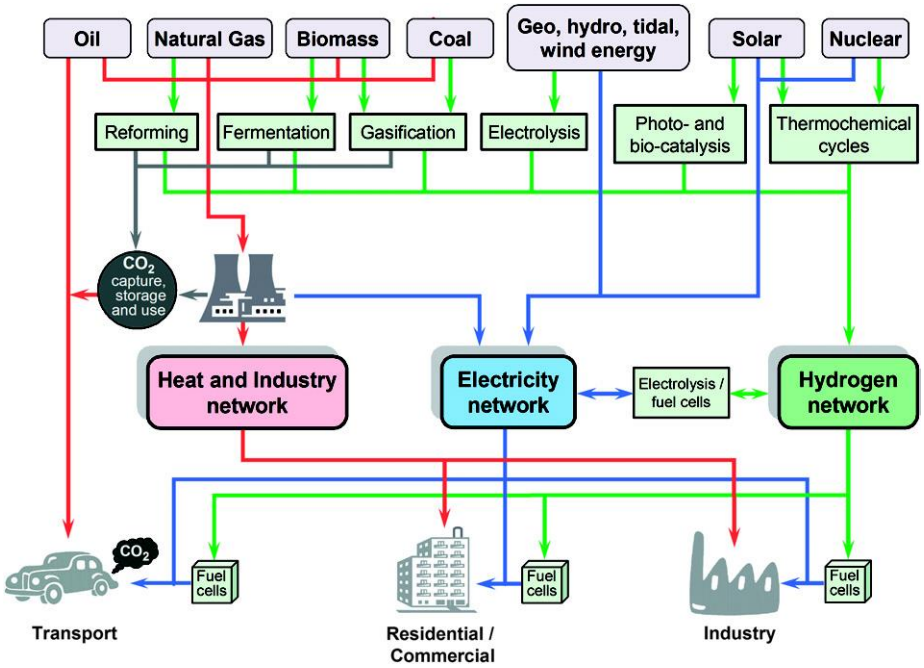

Figure 1.2 Hydrogen nexus: a possible model for a hydrogen energy economy. Reprinted with permission[11]. Copyright 2008, The Royal Society of Chemistry.

Among many paths for H_2 production above, the photoelectrochemical (PEC) cell is a highly promising system to produce hydrogen and oxygen from water using solar energy. In this process, the energy imparted by solar radiation is stored in the chemical bonds of diatomic hydrogen with water as the only emission or as a reactant. Efficiency values exceeding 10% have been reported for the best PEC cells based on low-cost and stable metal oxide absorbers[7, 12, 13]. Although PEC cells are still less efficient than PV-driven electrolyzes, they also have important advantages: in PEC cells, for example, the heat from sunlight can be used to further accelerate the reactions. And because current densities are ten to a hundred times lower with this approach, it is possible to use abundant and very inexpensive materials as catalysts. Since the pioneering discovery of photo-assisted electrochemical water oxidation on an n-type titanium dioxide (TiO_2) single-crystal electrode in 1972 by Fujishima and Honda[14], the semiconductor photocatalytic materials and fabrication techniques into photoelectrodes have been considered essential for high efficiency and have become the subjects of intensive research worldwide.

1.2 Fundamentals of PEC water splitting

PEC water splitting works by converting solar energy to hydrogen by applying an external bias to photovoltaic materials immersed in an electrolyte containing a redox couple. A simple PEC configuration (Figure 1.3a-c) consists of two electrodes: a photoactive semiconductor electrode and a metal counter electrode, both immersed in an electrolyte solution that allows ionic species transport. In addition, to characterize the externally applied voltage, a reference electrode is connected to the working electrode.

The applied external bias overcomes the slow kinetics and provides enough voltage for the PEC cell to drive the reaction at the desired rate/current density. When a semiconductor electrode is immersed in an electrolyte solution in dark, equilibration takes place at the interface by shifting the Fermi Level (E_f) of the semiconductor to match with the redox potential of the electrolyte[15]. For establishing the thermodynamic equilibrium, the majority charge carriers (electrons in an n-type semiconductor and holes in a p-type semiconductor) are transferred to the second phase upon contact to equalize the E_f. Since the density of electrons in a semiconductor is finite and the potentials of the band positions at the interfaces can be assumed to be pinned, the electron transfer causes band bending. This band bending is more pronounced for interfaces in close, intimate contact but less so when the space charge layer width is greater than the particle size, in the case of nanoparticles[16]. For a n-type semiconductor electrode, the E_f is normally higher than the redox potential of the electrolyte and then electrons are transferred from the electrode into the solution. Therefore, a positive space charge layer is formed, also called depletion layer since the region is depleted of majority charge carriers (Figure 1.3a). On the other hand, a p-type semiconductor has an initial E_f below that of the electrolyte. Then, a negative space charge layer is then formed as holes are transferred

into the electrolyte (Figure 1.3b). A charged layer of opposite sign is induced in the electrolyte adjacent to the interface with the solid electrode - Helmholtz layer. This layer consists of charged ions from the adsorbed electrolyte on the solid electrode surface. The Helmholtz layer width (few angstroms) is usually smaller than the space charge layer width[17]. At zero kelvin, the valence band (VB) is filled with electrons, whereas the conduction band (CB) is mostly empty.

Under illumination, as shown in Figure 1.3d, there are five main processes occurring[18, 19]:

1) Solar light absorption by the photoelectrode;
2) Upon excitation by an external energy source (e.g., a photon), charge carriers are generated and an electron in the VB is excited to the CB, leaving a hole in the valence band, creating electron-hole pairs;
3) The excited electrons flow from the back contact of the semiconductor, via the external circuit, to the counter electrode; The excited holes or OH^- ions diffuse back to react with holes at the surface of the photoelectrode;
4) Charge recombination occurs inside the semiconductor;
5) Reducing water to hydrogen or oxidizing holes to oxygen.

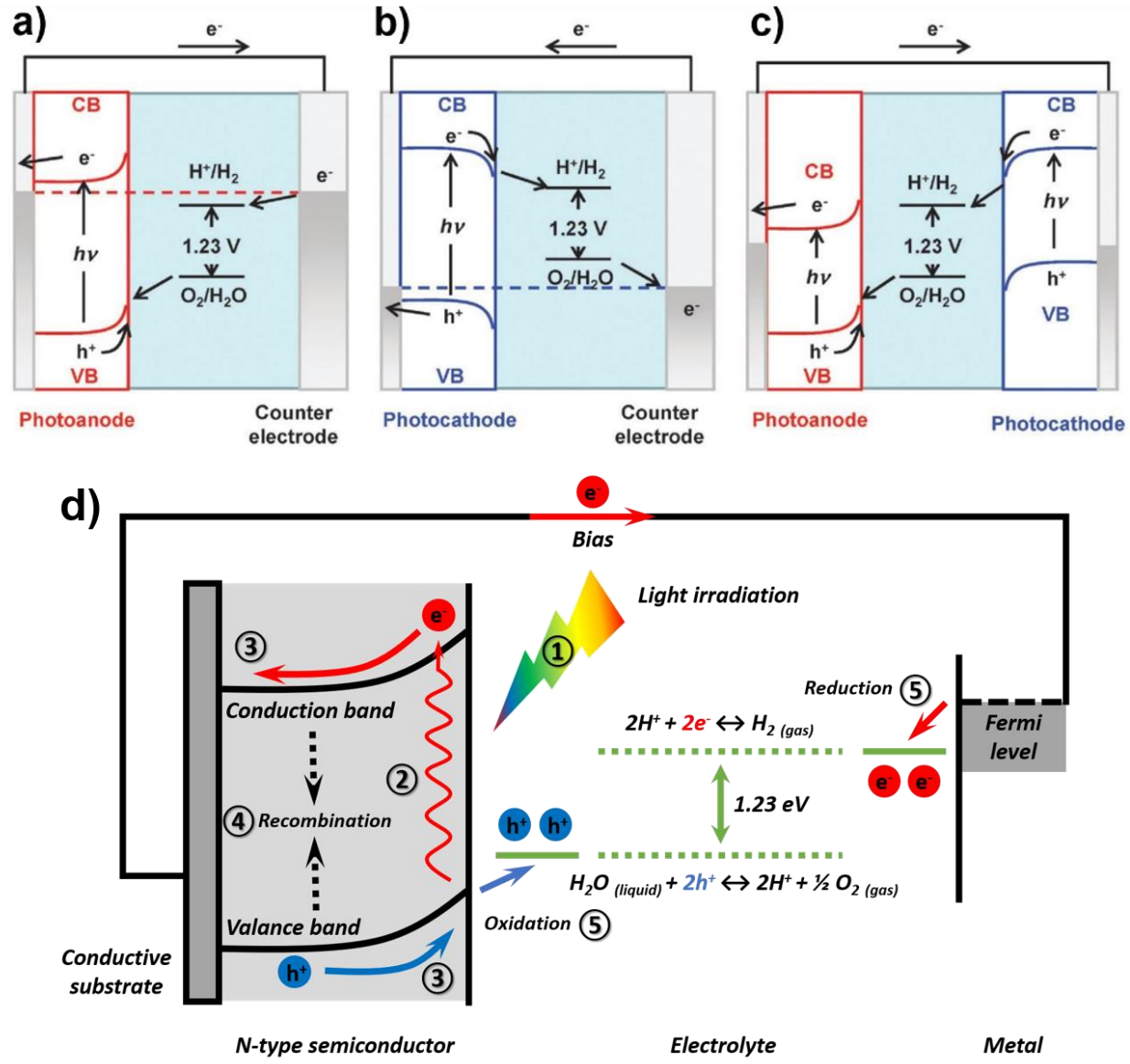

Figure 1.3 PEC water splitting using (c) a photoanode, (d) photocathode, and (e) photoanode and photocathode in tandem configuration. (d) A photoelectrochemical (PEC) cell under illumination based on a n-type photoelectrode and a metal cathode.

The PEC systems do not require gas separation due to their structure, which entails one or two conductive electrodes and a small bias. The two different gases are sequentially generated and remain at the opposite electrodes[20]. In order to remain competitive, efficiency, durability, and cost need to be further improved. The ongoing research and development of PEC materials, devices, and systems is making significant progress, benefitting from strong synergies with contemporary research in photovoltaics, nanotechnologies, and computational materials. (1) Sunlight absorption and surface catalysis are being improved to improve efficiency. (2) Durability and lifetime are being improved with more rugged materials and protective

surface coatings. (3) Hydrogen production costs are being lowered through reduced materials and materials processing costs.

1.3 Requirements of PEC materials

The key component of a PEC water splitting cell is the semiconductor photoelectrode, which must enable light absorption, charge separation, migration, and transfer to the electrolyte solution for redox reactions. This leads to high demand of light absorption, redox capability, efficient charge transport, high chemical stability, and low cost on the semiconductor as follows[8, 19, 21]:

1.3.1 Light absorption

Bandgap energy (E_g) is the basic parameter that determines the spectral region in which the semiconductor absorbs light. The water splitting reaction is thermodynamically nonspontaneous, and therefore is an uphill reaction. It needs the standard Gibbs free energy change ΔG^0 of 237.18 kJ mol^{-1} or 1.23 eV, as shown in Eq. 1.1:

$$H_2O \rightarrow \frac{1}{2}O_2 + H_2;\ \Delta G^0 = 237.18\ kJ/mol \quad (1.1)$$

$$Photocathode: 2H^+ + 2e^- = H_2; E(red) = 0\ V \quad (1.2)$$

$$Photoanode: H_2O + 2h^+ = \frac{1}{2}O_2 + 2H^+; E(ox) = 1.23\ eV \quad (1.3)$$

Therefore, the E_g of the photocatalyst should be large than 1.23 eV (~1008 nm) to achieve energy required for water splitting. However, due to the thermodynamic energy losses (0.3-0.4 eV)[22] occurring during charge carrier transportation and overpotentials required for acceptable surface reaction kinetics (0.4-0.6 eV)[23, 24], there are significant back processes involved during the solar water splitting[25, 26]. Therefore: A minimum E_g of ~1.9 eV is required, corresponding to an absorption onset at ca. 650 nm[27]. The maximum value of the bandgap is determined by the solar spectrum shown in Figure. 1.4. The upper limit on the E_g is ~3.1 eV, because of the rapid drop in sunlight intensity below 390 nm. Hence, the optimal value of the bandgap should be somewhere between 1.9 and 3.1 eV, which is within the visible range of the solar spectrum.

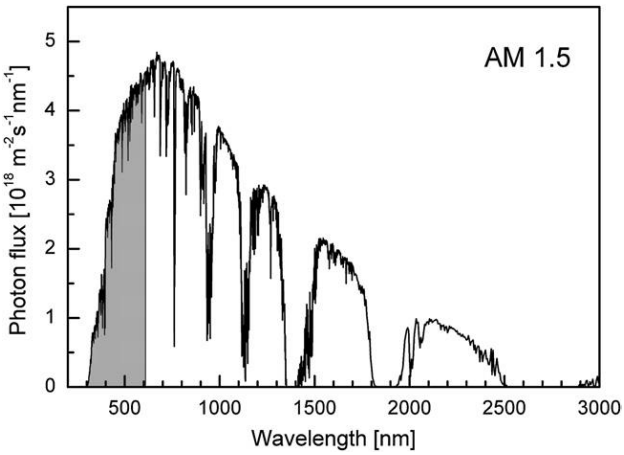

Figure 1.4 Intensity of sunlight versus wavelength for AM 1.5 (100 mW·cm^{-2}) conditions. Reprinted with permission[27]. Copyright 2008, The Royal Society of Chemistry.

1.3.2 Redox capability

The CB and VB edges of semiconductors should 'straddle' the reduction and oxidation potentials. For solar water splitting, the valence band potential must be more positive than the O_2/H_2O redox potential of 1.23 eV versus Normal hydrogen electrode (NHE, pH = 0) to permit water oxidation, and the conduction band must be more negative than the H_+/H_2 redox potential of 0 V versus NHE to facilitate water reduction[28, 29]. The flat band potential of most metal oxide (MO) semiconductors (and even some non-oxide semiconductors) varies by pH value [30-32]. It should be noted that the data in Figure 1.5 are drawn for a pH of 0, most non-oxide semiconductors are able to reduce, but not oxidize water. In contrast, most MO semiconductors are able to oxidize, but not reduce water. Since the stability criterion and suitable band gap position favors MO semiconductors, the reduction of water appears to be challenging[33-35].

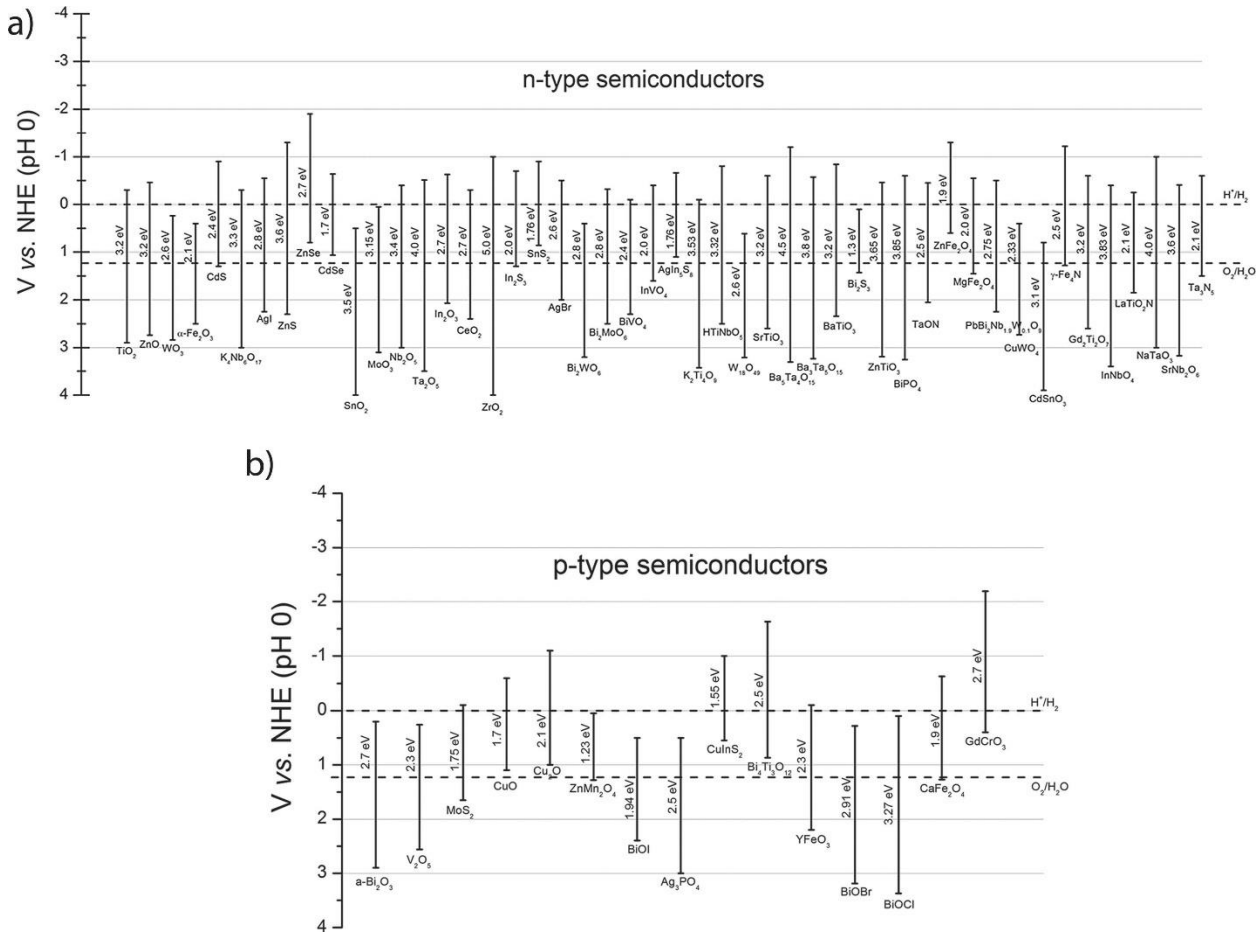

Figure 1.5 Band gaps and band positions of a) n-type semiconductors and b) p-type semiconductors. Reprinted with permission[36]. Copyright 2013, Wiley.

1.3.3 Efficient charge transport

Efficient charge transport is easily fulfilled by some materials, while in others it is the main cause of poor overall conversion efficiencies. After excited electron-hole pairs are created, charge recombination and migration take place simultaneously inside the semiconductor photocatalyst that largely affects the solar energy conversion efficiency of the photocatalytic reaction for water splitting[37]. The electronic structure of the material determines the mobilities of electron and hole[38]. The conduction and valence band of most (but not all) MOs are primarily composed of metal 3d orbitals and oxygen 2 p orbitals, respectively[39]. Hence, extensive overlap of the metal 3d orbitals will lead to high electron mobilities, while the amount of overlap between the O-2p orbitals determines the hole mobility. Even though orbital overlap arguments may provide some initial guidelines for evaluating the charge transport properties of a material, extrinsic factors such as the presence of defects often play a much more important role. Appropriate amounts of defects mainly enhance the conductivity and conductivity type of a semiconductor to promote charge

transfer[40-42]. Based on the defects generated energy levels, they can be separated into shallow level and deep level. Shallow level means that a donors or acceptors energy level closes to the CB or VB in the semiconductor, and basically all ionization is achieved at room temperature, thereby improving the conductivity of the semiconductor and changing the conductivity type. On the contrary, deep level refers to the donor or acceptors energy level far away from the CB or VB that of a semiconductor, which needs a large ionization energy, so no shallow energy-level impurity can affect the carrier concentration and conductivity type. Therefore, the deep level defects will act as effective recombination centers, reducing the carrier lifetime, known as a nonradiative recombination center. When this type of defect introduces into the semiconductor for water splitting, it will affect the luminous efficiency and increase the resistivity of the material as a compensating impurity[42, 43]. Generally, the higher the semiconductor crystalline quality is, the smaller the number of defects is. If the photocatalysts size becomes small in some dimension, such as zero-dimensional (0D) nanodots[44-46], one-dimensional (1D) nanowires or fibers[47-49], two-dimensional (2D) nanosheets[50-53], the distance that photogenerated electrons and holes have to migrate to reaction sites on the surface becomes short and consequently lower their recombination rate.

1.3.4 High chemical stability and low cost

The semiconductor must be highly stable in order to withstand both chemical and photocorrosion. Normally, the stability against corrosion increases with E_g of semiconductor, but larger value of E_g limits the ability of light absorption. Non-oxide semiconductors, such as Si, GaAs, GaP, CdS, etc. either dissolve or form a thin oxide film which prevents electron transfer across the semiconductor/electrolyte interface[27]. However, if the kinetics of charge transfer across the interface (oxidation of water) are faster than the anodic decomposition reaction, photo-corrosion can be avoided. Only scalable thin film technology and earth-abundant materials can meet the aim price of 5 € kg^{-1} H_2 set by the European Commission[26], and the target cost of \$2 to \$4 kg^{-1} set by the department of energy USA for future solar hydrogen production[54]. Last but not the least, for the global sustainable development, the semiconductor employed should be synthesized via “green” processes.

Due to the aforementioned stringent requirements, no single photo-active semiconductor has yet been discovered that meets all of them. Unless this challenge can be met, PEC water splitting technology might not be viable. During the last decades, various MO (TiO_2[55-57] ,ZnO[58-60], a-Fe_2O_3[61], WO_3[62, 63], $BiVO_4$[64-66], Cu_2O[67, 68], etc.) and non-oxides (silicon[69, 70], GaAs[71, 72], GaP[73], CdS[74-76], InP[77, 78], TaON[79, 80], Ta_3N_5[81, 82], etc) semiconductor have been extensively explored and reported.

Among the commonly used semiconductors for photoelectrode, MO is often considered as the class of material suitable for solar water splitting, mainly due to their excellent chemical stability in aqueous

solution, suitable band edge position, and relatively low cost[33, 34]. However, on one side, some of them do not have very good semiconducting properties, such as carrier mobility problems, compared to III-V semiconductors or even Si. The challenge is then to overcome these limitations while taking advantage of the MO properties. On the other side, current strategies to optimize the separation of electron-hole pairs in photoelectrodes mainly focus on chemical and structural optimization (e.g., control of morphology and crystallography), which are limited by the synthesis techniques currently in use. In oxide materials synthesis, many metals have problems with source oxidation or low oxidation potentials, such as Ti and Sn[83]. As a matter of fact, the traditional synthetic methods of these MOs are mainly produced via using wet chemical routes which involve complex processes and need high reaction temperature (e.g., hydrothermal/solvothermal methods)[84-86]. Despite many advances, these conventional synthetic techniques are insufficient in synthesizing materials with the desired water splitting properties, like tailoring the morphology in an easily scalable way with a high degree of reproducibility[87].

1.4 Metal-organic framework (MOF) and their derivatives

During the last two decades, metal-organic framework (MOF), a new type of inorganic-organic hybrid and crystalline materials of high porosity, has attracted intense academic interest. Due to the diversity of the metal ions and organic ligands, immeasurable combinations of MOF can be developed to suit the targeted application, such as gas sorption/separation[88-90], catalysis[91-93], chemical sensing[94, 95], energy storage and conversion[96-99], etc. MOF can be synthesized in one-dimension (1-D), two-dimension (2-D), or three-dimension (3-D) structure based on the different organic and inorganic units. Furthermore, due to the well-defined crystalline structures, adjustable pore topology, ultrahigh surface areas, and excellent tailor-ability, MOF materials can be designed for some specific application. However, due to the lability of ligand-metal bonds, the instability in aqueous solutions has considerably limited these MOFs' further application and commercialization, since water or moisture is usually present in most industrial processes as mentioned[100-102]. On the other hand, poor electrical conductivity further impedes the application of pristine MOF in the in the field of electrochemistry and electrocatalysis[103, 104].

The good thing is that, other than their direct use, the thermal transformation of MOF creates a variety of much more stable and conductive nanostructured materials, including carbon-based materials, MOs, metal chalcogenides, metal phosphides and metal carbides[105]. In addition, considering that most MOFs are constructed by transition metals and organic ligands containing C, H, O, N, S, etc., which are usually necessary elements in catalytic applications, their derivatives with the same elementary compositions as parent MOFs would possess great potentials in catalysis. These derivatives of MOF share many of the same characteristics as pristine MOF, including large surface area, composition diversity and dispersion, as well

as tailored porosity[106-109], which makes them have more advantages compared with traditional catalysts. Therefore, MOF-template synthetic method offers an alternative method for preparing diversity MOs that has numerous advantages over traditional chemical and physical synthetic methods, mainly in the following points: (1) simple method to fabricate variety of MOs; (2) ordered porous structure and adjustable pore size; (3) high surface area with more active sites; (4) controllable size and inherited morphology from MOF precursors (benefitting the optimization of catalytic performance); (5) facile doping of highly dispersed heteroatoms; (6) predesign of MOF precursors allows accurate control of active sites. Given all the aforementioned advantages, MOF-derived MO and MO composite (See Figure 1.6), with diverse morphologies and structures, are very promising candidates for photocatalysis[110-113]. It is worth pointing out that a lot of hybrid micro-/nano-structures MO with complex compositions, unique structures and specify functions have also been synthesized by using MOF as precursors/templates. These mixed MOs usually possess enhanced properties as compared to their individual counterparts, which is due to the synergistic effect among different components, making them more attractive for high-performance energy storage/conversion applications[107].

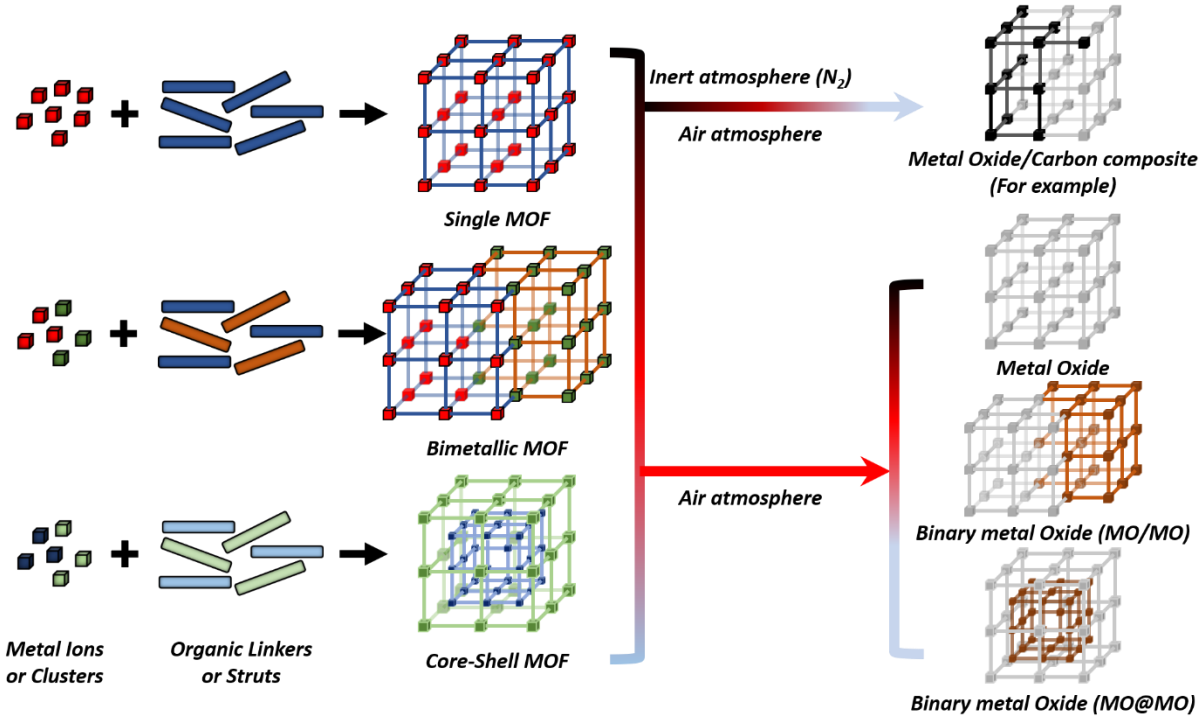

Figure 1.6 Strategic concepts for the preparation of porous nanostructured MO and MO composite from MOFs

1.4.1 MOF-derived pure MO

To date, a lot of MOs have been successfully derived from MOF, including titanium dioxide (TiO_2)[114-118], zinc oxide (ZnO)[119-121], cobalt oxide (Co_3O_4)[122-125], iron oxide (Fe_xO_y)[126-128], magnesium oxide (MgO)[129], nickel oxide (NiO)[130, 131], cupric oxide (Cu_xO)[132], and indium oxide (In_2O_3)[133-135]. In recently years, mixed MOs (MMOs, general formula: AB_2O_4) have received increasing attention[136-138]. Due to the synergistic effect of various metallic species inside and the multiple valences of the contributing metals, they exhibit enhanced electronic activity and conductivity compared to single component MO[139]. While numerous reports have been published on the fabrication of MO via MOF-template method, efforts to develop water splitting applications using these materials are limited. Several factors may contribute to this, including: (1) without pre-nitrogen treatment, the inherent morphology of the parent MOF will be destroyed that leads a significant decrease in both surface area and porosity; (2) when the annealing temperature is low, a high resistance is introduced into the sample as a result of unwanted carbon bonding. Thus, in order to make highly water splitting efficient out of MOF-derived MO nanomaterials, we must address these issues.

1.4.2 MOF-derived MO/carbon composites

When used as photoelectrodes, either pure MO or MMOs suffer from two major drawbacks: poor electrical conductivity and low surface area. Pure MO as high crystalline materials has hole diffusion length ~20 nm that would increase the recombination possibility and thus limits their water splitting performance[33, 139]. However, by matching the pore size of the MOF-derived MO with the electrolyte ion size through optimization of the heating conditions, some amorphous materials which the electrolyte can diffuse for a larger distance (∼50 nm) will improve the efficiency of water splitting through suppressing the recombination rate. For poor electrical conductivity and low surface area, these problems may also be solved by combining the MO material with a carbon-based material or by depositing the MO material on a conductive carbon matrix[140, 141]. However, if we employ conventional chemical synthetic methods to fabricate the MO/carbon composite, it is hard to control the resulting MO particles sizes due to the self-agglomeration, which severely affects their functional performance.

MOF has been demonstrated as suitable precursors for derivation of porous MO/carbon composites due to the presence of metal nodes which can be oxidized to form MO along with the existence of organic linkers which can be decomposed to form porous carbons[105]. On one side, MOF-template strategies can also produce carbon-coated MO particles with better dispersion than traditional methods. On the other side, the incorporation of heteroatoms, such as nitrogen (N), phosphorus (P), and/or sulfur (S), into the carbon

frameworks can allow effective tuning of their intrinsic properties, including electronic characteristics, surface and local chemical features, as well as their mechanical properties[142, 143].

1.4.3 MOF-derived MO composites

Apart from the pure MO, MMOs, and MO/carbon, MOF has also been utilized as precursors or template for fabricating porous MO composites (MO/MO or MO@MO), which consists two MOs constituents. These designed MO composites combine the unique properties of the individual oxide and enhance the synergistic effect through the interaction between two MOs[86]. They can not only provide the multiple redox reaction but also exhibit better electrical conductivity though the relatively low activation energy or fast electron transfer between metal cations[105]. So far, the MOF derived MO composites are obtained via two main methods: (1) by coating a secondary layer of MOF on the core MOF's surface, to form core-shell structure of MOF composites; (2) by making bimetallic MOF composed of two different metal ions. Nevertheless, it remains challenging to produce MO composites from MOF.

With the exception of all the above, MOF-template method can also be used to synthesize complex ternary M/MO/C and MO/MMO/C composites. This could be ascribed to the metal nodes in MOF can be transformed in situ into metal nanoparticles during the carbonization process, whereas the organic linkers are converted to porous carbon materials[144].

1.5 Research objectives and thesis organizations

1.5.1 Research objectives

Due to the intensive consumption of fossil fuels, the problems of energy shortage and environmental pollution have become the most pressing issues that must be resolved for the sustainable development of modern society. As the most abundant renewable energy resource, solar energy is regarded as the ultimate solution to these issues. PEC water splitting on semiconductor-based photoelectrode is an attractive method for capturing and storing the solar energy in the form of chemical energy (e.g., H_2). Among the various semiconductors, MOs have attracted tremendous interest of material scientists by virtue of its fascinating merits, such as good physicochemical stability, low cost, and wide distribution. Nevertheless, traditional wet chemical synthesis routes for MOs are complex and require a high reaction temperature. Furthermore, conventionally synthesized MOs are insufficient for the synthesis of materials with the desired water splitting properties. Therefore, it would be highly desirable to develop a straightforward MO synthesis method that meets all requirements. To date, even though many MO nanostructures have been successfully

derived from MOF, their applications in solar water splitting are still limited. Thus, the objectives of this thesis are as follows:

(1) ***Building an-type photoanode based on MOF with improved charge separation.*** PEC systems are highly efficient when photogenerated charge carriers are separated and transported efficiently. The design of semiconductor heterojunctions has proven to be one of the most effective strategies. For this reason, I decided to design a controlled mixed-phase of TiO_2 photoanode.

i. Synthesizing an anatase/rutile mixed-phase TiO_2 by MOF-template.
ii. Characterization of this mixed-phase TiO_2 structure. The morphology and optical properties of the different photoanodes is investigated.
iii. Device fabrication and evaluation of the performance.
iv. Charge transfer investigation. Electrochemical Impedance Spectroscopy (EIS) and Ultraviolet Photoelectron Spectroscopy are used to investigate the role of phase junction in the charge kinetics in the photoanode.

(2) ***Design a p-type NiO-based photocathode.*** Photocathode materials are far behind photoanode materials for PEC architectures, which are flourishing. As a result, highly efficient PEC systems are hindered by this situation. In order to address these issues, we developed a low-cost alternative solution based on p-type NiO and quantum dots.

i. Preparation of the hierarchical hollow NiO/carbon nanostructures by using nickel-based MOFs (Ni-MOFs) as sacrificial template. Introducing carbon materials inside the NiO-based photocathode via MOF-template, which will overcome all the drawbacks of traditional NiO photocathode
ii. Characterization of the composite structure. The morphology and optical properties of the NiO/carbon photocathode is investigated.
iii. Device fabrication and evaluation of the performance.
iv. The role of the NiO/carbon composite is investigated and the presence carbon materials promotes fast charge transfer.

(3) ***Employing a MOF-on-MOF structure to build a p-n junction nanocomposite photoanode.*** An improved synthesis method could provide a heterojunction interface that facilitates electron and hole separation and migration. Moreover, I decided to use metal oxide for light absorption instead of QDs as the sensitizer. Thus, I synthesize In_2O_3/CuO p-n heterojunction composite.

i. Preparation of p-n heterojunction In_2O_3/CuO composites with hollow hexagonal rod-shaped structure by using MOF-on-MOF as sacrificial template.

ii. Characterization of the composite structure. The morphology and optical properties of the the In_2O_3/CuO-GNRs photoanode is investigated.

iii. Device fabrication and evaluation of the performance.

iv. The role of the In_2O_3/CuO composite in charge transfer and band energy alignment was determined.

1.5.2 Thesis organizations

This thesis is composed of 6 chapters and the structures are as follows:

Chapter 1 introduces the basic background and work fundamental of PEC water splitting for hydrogen generation. Subsequently, it also presents the motivation and the main goals of my research. Furthermore, a literature review is offered focusing on the development of MOF-derived MO. The publications related to this chapter are:

L. Shi, D. Benetti, Q. Wei, F. Rosei, Metal-Organic Framework Derived Nanoporous Metal Oxide for Solar Water Splitting, *Materials Today, (TBD)*.

Chapter 2 provides the experimental details. Synthetic methods of all the MOF and related MO samples, characterization information, PEC test, and H_2 production. All the devices are also described in this chapter.

Chapter 3 corresponds to ***my first project***. an anatase/rutile mixed phase TiO_2 with octahedral structure was subtly designed and synthesized by using MOF as sacrificial template. After sensitization with quantum dots, the PEC performance of the MOF-derived TiO_2 photoanode is systematically investigated. The publication related to this chapter is:

L. Shi, D. Benetti, F. Li, Q. Wei, F. Rosei, Phase-junction design of MOF-derived TiO_2 photoanodes sensitized with Quantum Dots for efficient hydrogen generation. *Applied Catalysis B: Environmental*, 263 (2020) 118317.

Chapter 4 corresponds to ***my second project***. A nickel-based MOFs was used as the precursor to synthesis a hollow ball-in-ball structure NiO/carbon nanohybrid photocathode. After sensitization with quantum dots, the PEC performance of this photocathodes was investigated at neutral pH and without any sacrificial reagent, cocatalyst, or molecular linker. The publication related to this chapter is:

L. Shi, D. Benetti, F. Li, Q. Wei, F. Rosei, Design of MOF-Derived NiO/carbon Nanohybrids Photocathodes Sensitized with Quantum Dots for Solar Hydrogen Production. *Small*, (2022) 2201815.

Chapter 5 corresponds to ***my third project***. we developed a facile synthesis of p-n heterojunction junction In_2O_3/CuO composite with hollow hexagonal rod-shaped structure by using MOF-on-MOF structure as

sacrificial template. By incorporation of small amounts of graphene nanoribbons, the optimal photoanode shown a remarkable photocurrent density and good stability. The publication related to this chapter is:

L. Shi, D. Benetti, F. Li, Q. Wei, F. Rosei, MOF-derived In_2O_3/CuO p-n heterojunction photoanode incorporating with graphene nanoribbon for solar hydrogen generation, *Small* (2023) 2300606.

Chapter 6 briefly summarizes the main conclusions and discusses future challenges and perspectives in this field.

Following the main body of this thesis is a synopsis of this thesis in French as per the INRS requirements.

2 EXPERIMENTAL

2.1 Materials

2-Amino-1,4-benzenedicarboxylic acid (NH_2-BDC), 1,3,5-benzenetricarboxylic acid (H_3BTC), 1,4-benzenedicarboxylic acid (H_2BDC), titanium isopropoxide ($C_{12}H_{28}O_4Ti$, TOPT), *N*,*N*-Dimethylformamide (DMF), ethyl cellulose, alpha-terpineol, oleylamine (OLA), selenium (Se) powder, sulfur (S) powder, iodine, oleic acid (OA), 1-octadecene (ODE), cadmium oxide (CdO), trioctyl phosphine (TOP) (97%), trioctyl phosphine oxide (TOPO), nickel (II) acetate tetrahydrate ($Ni(COOCH_3)_2{\cdot}4H_2O$), ethanolamine, polyvinylpyrrolidone (Mw = 40000), nickel (II) nitrate hexahydrate ($Ni(NO_3)_2{\cdot}6H_2O$), copper (II) acetate monohydrate ($Cu(COOCH_3)_2{\cdot}H_2O$), copper(II) nitrate trihydrate ($Cu(NO_3)_2{\cdot}3H_2O$), zinc (II) acetate dihydrate ($Zn(COOCH_3)_2{\cdot}2H_2O$), cadmium (II) acetate dihydrate ($Cd(COOCH_3)_2{\cdot}2H_2O$), cadmium (II) nitrate tetrahydrate ($Cd(NO_3)_2{\cdot}4H_2O$) indium(III) nitrate hydrate ($In(NO_3)_3{\cdot}xH_2O$), sodium hydroxide (NaOH), graphene nanoribbons (GNRs) of several micrometers length and below100 nm width, acetone, methanol, ethanol, toluene, isopropanol, Triton X-100, sodium sulfide nonahydrate ($Na_2S{\cdot}9H_2O$), sodium borohydride ($NaBH_4$), sodium sulfite (Na_2SO_3), zirconium(IV) oxide (ZrO_2) nanopowder (particle size < 100 nm), and sodium sulfate (Na_2SO_4) were purchased from Sigma-Aldrich Inc. Ti-Nanoxide BL/SC was obtained from Solaronix. Titania paste containing ~20 nm nanoparticles in diameter (18 NR-T) and larger light-scattering anatase particles (~450 nm) paste (18 NR-AO) were purchased from Dyesol (Queanbeyan, Australia). Fluorine doped tin oxide (FTO) coated glass substrates with sheet resistance 10 Ω/square were bought from South China Xiang Science & Technology Company Limited. The absolute pure water, purified by a Millipore Ultrapure water system and having a resistivity of 18.2 MΩ cm at 25 ^{o}C, was used in the current investigation. All chemicals were used as received without further purification.

2.2 Synthesis anatase/rutile mixed phase TiO_2

2.2.1 Synthesis of NH_2-MIL-125(Ti) precursor

The NH_2-MIL-125(Ti) as a sacrificial template was synthesized according to a solvothermal method described by Su et al. with slight modifications[116]. Typically, a mixture solution of TPOT (1.5 mL, 5 mmol), H_2BDC-NH_2 (3.0 g, 16.55 mmol), DMF (54.0 mL) and CH_3OH (6.0 mL) were transferred to a 100 of mL Teflon-lined stainless-steel autoclave and heated at 150 ℃ for 24 h. Upon cooling down, the yellow suspension of NH_2-MIL-125(Ti) was centrifuged and washed with DMF and CH_3OH three times, respectively.

2.2.2 Synthesis of anatase/rutile TiO_2 (M-TiO_2)

0.5 g of the as-prepared NH_2-MIL-125(Ti) was annealed in air at 500 ℃ with a ramping speed of 10 ℃ min^{-1} from room temperature and maintained at the temperature for 4 h. After naturally cooling, pale white powder of M-TiO_2 was obtained. For comparison, the NH_2-MIL-125(Ti) was also annealed in air at 575 °C following the same procedure. This sample is named M-TiO_2-575.

2.2.3 Synthesis of CdSe QD

CdSe QDs were first synthesized via a hot injection approach[145]. Typically, TOPO (1 g) was mixed with Cd-oleate (0.38 mmol, 1 mL) and ODE (8 mL) in a flask and purged by N_2 at room temperature for 30 min. After the degassing processing 30 min at 100 °C, the mixture heated to 300 °C. A mixture of TOP-Se (4 mmol, 4 mL), OLA (3 mL), and ODE (1 mL) was quickly injected into the reaction system under vigorous stirring. The temperature then dropped to 270 °C for CdSe growth. After several minutes, the solution was quenched with cold water after injection. The as-synthesized QDs were precipitated with ethanol, centrifuged to eliminate unreacted precursors, and finally dispersed in toluene.

2.2.4 Synthesis of core-shell CdSe@CdS QDs

The synthesis of core-shell CdSe@CdS QDs followed the familiar successive ionic layer adsorption and reaction (SILAR) approach pioneered by Rosei and co-workers with fine-tuned modifications[146]. A 100 mL flask was charged with OLA (5 mL), ODE (5 mL), and CdSe QDs (~ 2×10^{-7} mol in toluene) and was degassed for 30 min at 110 °C. The reaction temperature was set at 240 °C under N_2. Subsequently, the $Cd(OA)_2$ dispersed in ODE (0.25 mL, 0.2 m) was injected dropwise via syringe and the reaction proceeded for 2.5 h, followed by dropwise injection of 0.2 m sulfur in ODE with same volume. The shell was then annealed for 10 min. The reaction was cooled to room temperature using cold water. Ethanol was added, then the suspension was centrifuged and the supernatant was removed. The QDs were then dispersed in toluene.

2.3 Synthesis of hollow ball-in-ball NiO/carbon composite

2.3.1 Synthesis of Ni-MOFs precursor

The Ni-MOFs as a sacrificial template was synthesized according to a solvothermal method described by Zhu et al[147]. with some modifications. Typically, a mixture light green solution of $Ni(NO_3)_2 \cdot 6H_2O$ (432 mg), 1,3,5-benzenetricarboxylic acid (H_3BTC, 150 mg), PVP (Mw = 40000, 1.5 g), water (10 mL), ethanol

(10 mL) and N,N-dimethylformamide (DMF, 10 mL) were transferred to a 50 of mL Teflon-lined stainless-steel autoclave and then heated at 150 °C for 10 h. Upon cooling down, the final light green products were centrifuged and washed with DMF and ethanol three times, respectively. The collected materials were then dried in an oven overnight at 80 °C.

2.3.2 Synthesis of Ni/carbon composite and pure NiO nanoparticles

For Ni/carbon nanocomposite: 0.5 g of the Ni-MOF powder was annealed in a tube furnace in Ar atmosphere to 450 °C with a ramp-rate of 5 °C/min and held for 120 min. After naturally cooling, black powders of Ni/C were obtained.

For pure NiO nanoparticles: 0.5 g of the Ni-MOF powder was annealed to 450 °C for 360 min with a ramp-rate of 10 °C/min. The whole heating process was carried out in a tube furnace in Air atmosphere. After naturally cooling, black powders of NiO were obtained.

2.3.3 Synthesis of NiO/C composite

0.5 g of the Ni/C powder was annealed to 450 °C for 360 min with a ramp-rate of 10 °C/min. The whole heating process was carried out in a tube furnace in Air atmosphere. After naturally cooling, black powders of NiO/C were obtained.

2.3.4 Preparation of compact blocking layer of 5% Cu-NiO film

5% Cu-NiO thin film were prepared via a sol-gel solution process. Nickel (II) acetate tetrahydrate ($Ni(COOCH_3)_2 \cdot 4H_2O$, 0.3 M) precursors were dissolved in ethanolamine. Copper (II) acetate monohydrate ($Cu(CH_3COO)_2 \cdot H_2O$, 0.02 M) was used as dopant. This light blue solution was stirred at 80 °C for 12 h, then aged for 12 h at room temperature.

2.4 Synthesis of In_2O_3/CuO composite

2.4.1 Synthesis of MIL-68(In) and Cu-BDC

For MIL-68(In) MOF: A modified version of MIL-68(In) was prepared according to previous literature[148]. Typically, a mixture milky solution was prepared by mixing 1,4-benzenedicarboxylic acid (H_2BDC, 0.4 mol, 32 mg) and $In(NO_3)_3 \cdot xH_2O$ (0.4 mol, 7.8 mg) in 18 mL of DMF. Afterwards, the mixture was heated in an oil bath (100 °C) for 15 minutes. Upon cooling down, the final white products were centrifuged and

washed with DMF and methanol three times, respectively. The collected materials were then dried in an oven overnight at 80 °C.

For Cu-BDC MOF: 96.8 (0.4 mol) mg of the $Cu(NO_3)_2 \cdot 3H_2O$ and 32 mg (0.4 mol) H_2BDC were dissolved in 18 mL DMF. The resulting mixture was placed in an oil bath (100 °C) for 10 min. Light blue Cu-BDC generated in this time were isolated by cooling the reaction mixture to room temperature, collecting the precipitate by centrifugation, and washing three times with DMF and methanol. The collected materials were then dried in an oven overnight at 80 °C.

2.4.2 Synthesis of MIL-68(In)/Cu-BDC hexagonal rods precursor

100 mg of the obtained MIL-68(In) hexagonal rod powders, and 96.8 mg (0.4 mol) of $Cu(NO_3)_2 \cdot 3H_2O$ were dispersed in 18 mL DMF. After stirring continuously at room temperature for 30 min, the mixture was heated in an oil bath (100 °C) for 15 minutes. After cooling down, the final products were centrifuged and washed with DMF and methanol three times, respectively. The collected materials were then dried in an oven overnight at 80 °C.

2.4.3 Synthesis of pure In_2O_3, pure CuO and In_2O_3/CuO composite

For pure In_2O_3: 0.5 g of the MIL-68(In) powder was annealed in a tube furnace in Air atmosphere to 500 °C with a ramp-rate of 5 °C/min and held for 60 min. After naturally cooling, white powders of pure In_2O_3 were obtained.

For pure CuO: 0.5 g of the Cu-BDC powder was annealed in a tube furnace in Air atmosphere to 350 °C with a ramp-rate of 5 °C/min and held for 60 min. After naturally cooling, black powders of pure CuO were obtained.

For In_2O_3/CuO: 0.5 g of the MIL-68(In)/Cu-BDC hexagonal rods precursor powder was annealed in a tube furnace in Air atmosphere to 500 °C with a ramp-rate of 5 °C/min and held for 60 min. After naturally cooling, light brown powders of In_2O_3/CuO were obtained.

2.5 Device fabrication

2.5.1 Preparation of MO paste

For the first and third project, we employ the doctor-blade method to fabricate the photoelectrode. Therefore, before coat the MO on FTO glass, we need to prepare the MO paste. Typically, 0.5 g

corresponding MO (e.g., M-TiO_2) was mixed with 2.5 ml ethanol as a solvent, 0.5 ml alpha-terpineol as dispersant, 0.25 g ethyl cellulose which acts as a thickener, and 0.5 ml of water. The mixture solution was transferred into a beaker and stirred overnight. The solvent was removed by connecting it to a vacuum pump during continuous magnetic stirring until the volume of the mixture reduced to half of the starting volume.

2.5.2 Preparation of blocking layer

Due to the sensitizer is QD in our work, a back-illuminated configuration is used, thus more holes are photogenerated at the back contact and be exposed to recombination centers. For this reason, in order to reduce the charge recombination at the back contact, a blocking layer of was used as interlayer between the FTO and the films[149-151]. FTO glass substrates were cleaned ultrasonically for 15 min with acetone, ethanol, isopropanol (1:1:2), and then rinsed in deionized (DI) water and dried in N_2 gaseous flow. The cleaned FTO glass substrates were then treated in a UV-ozone cleaner for 10 min to further eliminate surface organic contaminations.

For the first project: a thin and compact TiO_2 layer was deposited on cleaned FTO substrates by spin coating at 6000 rpm for 30 s using the solution Ti-Nanoxide BL/SC, followed by annealing in air at 500 °C with a heating rate of 10 °C /min for 30 min and cooled down to room temperature.

For the second project: the prepared 5% Cu-NiO solution was spin-cast onto FTO glass substrates at a speed of 4000 rpm for 40 s. The substrate was then post-annealed at 450 °C in ambient air for 30 min with a heating rate of 10 °C /min.

For the third project: due to we did not employ any QDs in this project, there is no difference for front or back illumination. Therefore, blocking layer is not necessary.

2.5.3 Preparation of MO film

For the first and third project, we employed a simple doctor-blade (tape-casting) method to prepare the film. As shown in Figure 2.1 (e.g., TiO_2), the doctor blade is one of the widely used techniques for producing thin films on a smooth substrate. In a typical procedure, first, the conductive side of the FTO-coated glass was taped with tape to reserve a conductive part for conduction and to secure the thickness of the MO on the surface of the substrate. Second, one drop of the paste was then put onto the surface of a glass rod. Third, the MO paste was spread to provide a homogeneous paste on the substrate by uniformly moving a glass rod through the surface of the substrate. When a constant relative movement is established between

the glass rod and the substrate, the paste spreads on the substrate to form a thin film. Finally, the tape was removed from the edges of the substrate carefully for further drying and annealing treatment.

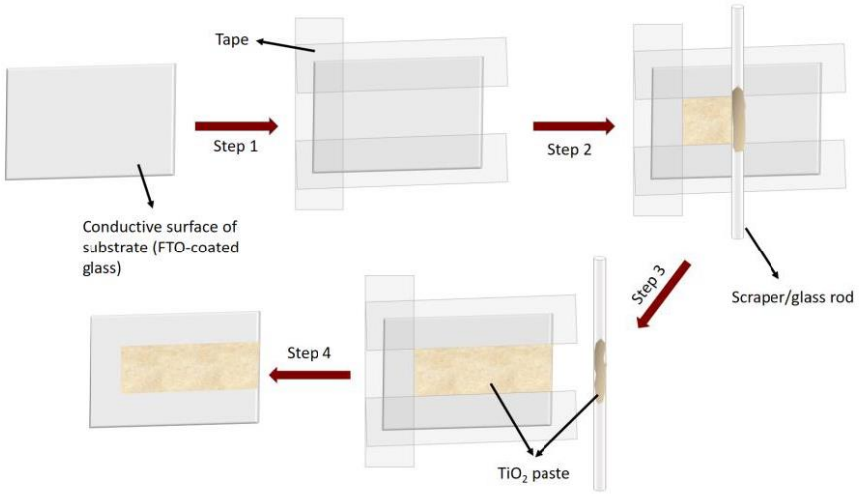

Figure 2.1 Schematic illustration of a flowchart for the doctor-blade method.

For TiO_2 film: after preparation of the blocking layer, the transparent paste containing ~20 nm nanoparticles in diameter (18 NR-T) were deposited onto FTO substrates using the doctor blade technique and kept in air for 12 min to completely spread out. The electrodes were subsequently dried at 120 °C for 6 min. A second layer of M-TiO_2 paste was then deposited on the top, following the same procedure. For comparison, a TiO_2 film was fabricated using anatase TiO_2 particles (~450 nm) paste (18 NR-AO) as the second layer, which was marked as C-TiO_2. The photoanodes were later sintered at 500 °C for 30 min in a furnace and cooled down to obtain the different photoanodes.

For NiO/carbon film: in this project, we prepared the film through the electrophoretic deposition (EPD) method which is considered to simple and inexpensive in a constant voltage mode[80, 152]. Briefly, 20 mg of the obtained Ni/C black powders, and 5 mg of iodine were dispersed in 20 mL of acetone. Then, a pair of FTO glasses with blocking layer were vertically immersed in the solution face-to-face and the distance between them was adjusted at 1.0 cm. A direct current (DC) bias of 20 V was applied for 5 min. The deposited area was about 1.0 × 1.0 cm^2. The Ni/C electrode was achieved after a drying process with N_2. Finally, the NiO/C photocathode was obtained by annealing the Ni/C electrode in air with a ramping speed of 10 °C/min at 450 °C for 30 min.

For In_2O_3/CuO film: a pure In_2O_3 layer was deposited onto FTO substrates using the doctor blade technique and kept in air for 12 min to completely spread out. The electrodes were subsequently dried at 120 °C for 6 min. A second layer of In_2O_3/CuO paste was then deposited on the top, following the same procedure.

The photoanodes were later sintered at 500 °C for 30 min in a furnace and cooled down to obtain the different photoanodes. A good dispersion of graphene nanoribbons (GNRs) in ethanol was prepared by mixing 4 mg of GNRs in 10 mL of ethanol and sonicated for 6 hours. In_2O_3/CuO-GNRs hybrid pastes with different concentration of GNRs were prepared by mixing the precise amount of ethanolic suspension of GNRs into a known weight of In_2O_3/CuO paste. The electrode was fabricated with similar procedures except that the first layer paste was used In_2O_3-GNRs instead of pure In_2O_3 paste and the second layer paste was used In_2O_3/CuO-GNRs instead of In_2O_3/CuO paste. Pure In_2O_3 electrode was also fabricated with similar procedures as those for the fabrication of the In_2O_3/CuO photoanode electrode except that the second layer paste was also used In_2O_3 instead of In_2O_3/CuO paste.

2.5.4 Sensitization of MO film with QDs

There are two main methods to sensitize the MO film, *in-situ* (SILAR) approach and *ex-situ* approach. In the *in-situ* method, the QDs are directly grown on the surface of the scaffold in the MO mesoporous films[153]. As shown in Figure 2.2, the sensitization process is completed simultaneously with the synthetic procedure. In both principle and practice, the SILAR process could now be considered as a best way to allow deposition of well-defined composition−modulated (doped, alloyed, or multilayered) QD layers onto mesoporous MO in the solution process, as demonstrated recently with colloidal QDs, where very precisely controlled multilayers were deposited over QD cores by alternating injection of cationic and anionic precursors[154-156]. However, the *ex-situ* method enables pre-synthesized QDs, making individually monodispersed QDs in the solvent. In order to apply them into the PEC cell, QDs need to be employed to sensitize the MO-based photoelectrode, via EPD or drop-casting[157-159]. The EPD approach is a technique that exploiting an electrical field to drive the deposition of colloidal QDs in solution upon the surface of the scaffold in MO mesoporous film. It was reported that there is an equilibrium existing between the population of non-charged majority and positively/negatively charged minority in colloidal QDs. These positively/negatively charged QDs enable the deposition of QDs in an electrical field[160].

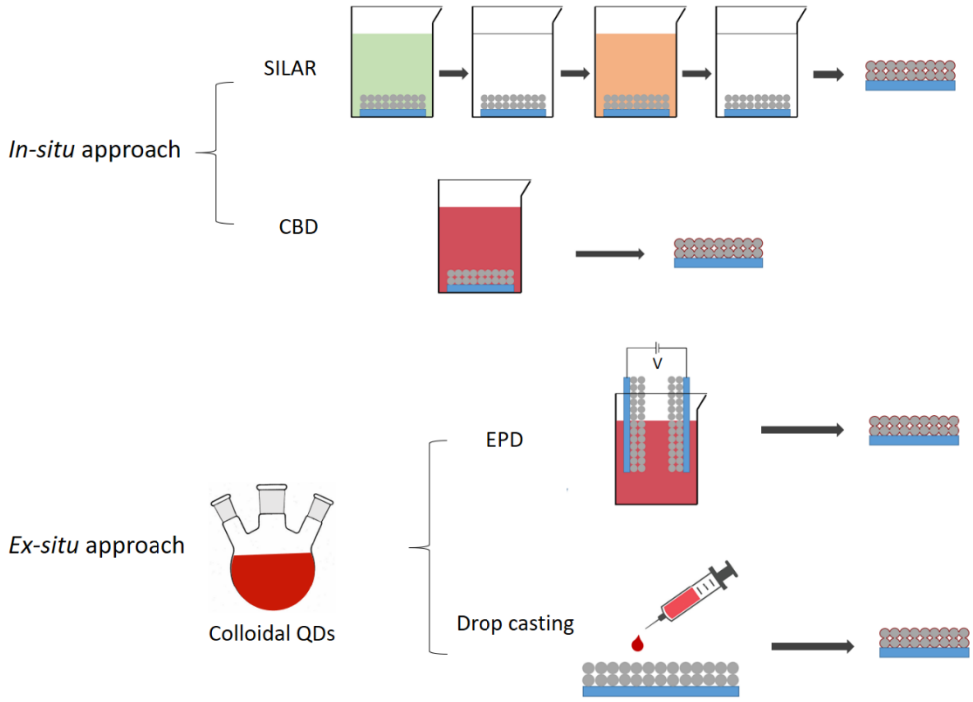

Figure 2.2 Schematic illustration of the sensitization of MO film with QDs prepared through in-situ or ex-situ approach.

For the M-TiO_2 film: A pair of TiO_2 (M-TiO_2 or C-TiO_2) films were vertically immersed in the QDs (detailed information for fabrication QDs is shown in 2.2.3 and 2.2.4) solution face-to-face and the distance between them was adjusted at 1 cm. A direct current (DC) bias of 200 V was applied for 120 min. To wash off the absorbed QDs from the surface of the TiO_2 film after the EPD process, the samples were rinsed several times with toluene to remove the excess of QDs and then dried with N_2 at room temperature. The ZnS capping layer was formed using a SILAR process to passivate the surface and prevent photocorrosion. In a typical SILAR deposition cycle, the QDs-sensitized TiO_2 electrode was immersed into $Zn(Ac)_2$ solution (0.1 M) for 1 min and then Na_2S solution (0.1 M) for 1 min, respectively. After immersing, the electrode was rinsed with corresponding solvents of methanol and methanol/DI water (1:1 v/v), separately, and dried with a N_2 gun. Two SILAR cycles were applied to form the capping ZnS layer. After the SILAR procedure, the surface (excluding the active area) of the photoanode was covered with epoxy resin to complete device fabrication.

For NiO/carbon film: CdSe was deposited on the surface of NiO/carbon film by SILAR method[161](Figure 2.3). To carry out the SILAR process for the deposition of metal selenides, it is essential to prepare selenide ions in solution and keep them stable for a long period. $NaBH_4$ was selected to reduce the Se in ethanol, as described by Eq 2.1.

$$Se + 2NaBH_4 + 6C_2H_5OH \rightarrow Se^{2-} + 2Na + 2B(OC_2H_5)_3 + 7H_2 \quad (2.1)$$

When an appropriate excess amount of $NaBH_4$ (2 mol) was added to a solution of 1 mol Se in 6 mol ethanol under inert atmosphere (N_2 purging), the color of the solution changed from deep red to transparent. It is indicated that Se^0(0) was being reduced to Se^{2-}(-2). The SILAR process was performed by following the usual procedure.

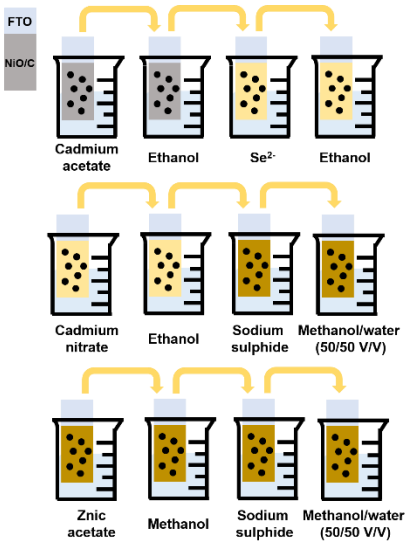

Figure 2.3 Schematic illustration of SILAR method.

For each CdSe SILAR cycle, the optimized NiO/C/FTO electrode was successively immersed into two different solutions for about 60 s each, one consisting of 0.03 mol/L^{-1} $Cd(COOCH_3)_2 \cdot 2H_2O$ dissolved in ethanol and the other containing the in situ generated 0.03 mol/L^{-1} Se^{2-} in ethanol. After each immersion, the photocathodes were rinsed for 1 min using pure ethanol to remove excess amounts of precursor and the electrode was dried under N_2 flux before the next dipping. CdS layers were deposited via SILAR approach[153]. Briefly, a 0.05 mol/L^{-1} ethanolic solution of $Cd(NO_3) \cdot 4H_2O$ and a 0.05 mol/L^{-1} solution of $Na_2S \cdot 9H_2O$ in methanol/water (50/50 V/V) were used as sources of Cd^{2+} and S^{2-}, respectively. 1 min dipping for the Cd^{2+} substrate precursor was applied. Subsequently, the same process was applied to the sulfide precursor. The sample was then washed with the corresponding solvent, to remove unabsorbed chemicals, and dried in N_2 flow. The CdSe was grown with two cycles of SILAR while the composite CdSe/CdS was grown using first two CdSe SILAR cycles followed by two CdS SILAR cycles. Finally, the QD-sensitized electrode was passivated with ZnS capping layer to prevent photocorrosion. In general, the QDs-sensitized NiO electrode was immersed into 0.1 M $Zn(CH_3COO)_2 \cdot 2H_2O$ for 1 min and then $Na_2S \cdot 9H_2O$ solution (0.1 M) for 1 min, respectively. After immersion, the electrode was rinsed with corresponding solvents of methanol and methanol/DI water (1:1 v/v), separately, and dried with a N_2 gun.

This cycle was repeated twice. After the SILAR procedure, the surface (excluding the active area) of the photocathode was covered with epoxy resin, leaving exposed to the electrolyte an active area of ~0.15 cm^2.

2.5.5 PEC devices fabrication and characterization

The MO films with/without the QDs were used to assess the PEC performance in a typical three-electrode configuration with a Pt counter electrode and an Ag/AgCl reference electrode (saturated with 3M KCl). A Gamry 1000E electrochemical workstation was employed to test the electrochemical measurements and the Eq 2.2 formula was used to convert the measured potentials (vs Ag/AgCl) to the potentials with respect to the RHE.

$$V_{RHE} = V_{Ag/AgCl} + 0.197 + pH \times 0.059 \quad (2.2)$$

Photocurrent density-voltage (J-V) curves were measured by linear sweep voltammetry (LSV, with sweep rate of 20 mV/s) and a Compact Solar Simulator Class AAA (Sciencetech SLB-300A) with a 150 W Xenon lamp as light source with an AM 1.5G filter at 1 sun light intensity (100 mW/cm^2). All the samples were back-illuminated (from the FTO glass side). Prior to each measurement, a Si reference diode (Sciencetech) was used to adjust the distance between photoanode and solar simulator to guarantee the standard 1 sun illumination (100 mW/cm^2) on the photoanode or photocathode in our three-electrode system. The distance from sun simulator to PEC cell was fixed at 15 cm.

The incident photon-to-current efficiency (IPCE) measurement was conducted using a home-made setup qualitatively. To derive the IPCE values, current-voltage measurements were performed with the use of different band-pass optical filters (10 nm band pass). The wavelength-dependent qualitative IPCE values can be calculated according to the following Eq 2.3:

$$IPCE(\%) = \frac{c \times h}{e} \times \frac{J}{\lambda \times I} = \frac{1240 \times J\ (mA/cm^2)}{\lambda(nm) \times I\ (mW/cm^2)} \times 100\% \quad (2.3)$$

where c is the speed of light (m/s), h is Planck's constant (J·s), e is the elementary electric charge (C), J represents the photocurrent density (mA/cm^2), λ is the wavelength of the incident photon (nm), and I is the intensity of the incident radiation (mW/cm^2) at a given wavelength, respectively. Electrochemical impedance spectroscopy (EIS) was carried by using a Gamry 1000E electrochemical workstation. All impedance measurements were analysed using an appropriate equivalent circuit model with Z-View software (v3.5, Scribner Associate, Inc.).

H_2 evolution was measured by online gas chromatography (GC). A gas-tight cell (total volume: 50 mL) was used for GC and it was filled with 20 mL electrolyte in a three-electrode cell configuration, using a

photoanode or photocathode as working electrode, an Ag/AgCl saturated reference electrode and a Pt plate as working electrode. Ar (Praxair, 99.999%) was used as carrier gas at a flow rate of 20 sccm and the electrolyte was continuously stirred. Before the measurements, the electrolyte was saturated with Ar gas for at least 30 minutes. A gas outlet was connected to a GC (Perkin Elmer Clarus 580 GC) for periodical sampling. A thermal conductivity detector (TCD) was used for detecting H_2. A gas aliquot was automatically injected into the GC every 150 s. During the online GC, a chronoamperometric measurement was performed by applying a different voltage vs RHE potential for 1 h.

The theoretical number of moles of hydrogen evolved can be calculated from Faraday's 2nd law of electrolysis according to the following equation 2.4:

$$n_{H_2}(\text{theoretical}) = \frac{Q}{zF} = \frac{I \times t}{zF} \quad (2.4)$$

Where n_{H_2} is the number of moles of hydrogen produced, Q is the total charge passed during electrolysis in coulombs (C), z is the number of electrons transferred during HER (i.e. $z = 2$), I is the applied current, t is the electrolysis time in seconds, and F is the Faraday constant 96 485.33 C mol^{-1}.

The Faradaic efficiency was calculated as follows Eq 2.5:

$$\eta_{Faradaic} = \frac{n_{H_2}(\text{experimental})}{n_{H_2}(\text{theoretical})} \times 100\% \quad (2.5)$$

2.6 Characterizations

The crystal structure of as-obtained products was characterized by X-ray diffraction (XRD) on a Bruker D8 X-ray diffractometer with Cu-Kα radiation (λ = 1.54178 Å). The absorption spectra were collected with a Cary 5000 UV-Vis-NIR spectrophotometer (Varian). High resolution transmission electron microscopy (HRTEM) images and EDS were collected by using a JEOL 2100F TEM and an Xplore model. SEM was collected by Tescan LYRA 3 XMH. TGA was obtained via Thermogravimetric Analyzer (Q500). X-ray photoelectron spectroscopy (XPS) was performed in a VG Escalab 220i-XL equipped with hemispherical analyzer, applying a Twin Anode X-Ray Source, calibration by carbon at 284.4 eV, and ultraviolet photoelectron spectroscopy (UPS) measurements were performed on a VG ESCALAB 3 Mark II high vacuum system. The specific surface area and porous structures were characterized by an accelerated surface area and porosimetry analyzer (Micromeritics Instrument Corp, ASAP 2020, analysis adsorptive: Nitrogen). The produced H_2 gas was detected using a gas chromatograph (GC) (Perkin Elmer Clarus 580 GC) equipped with a thermal conductivity detector. Argon gas was used as the carrier gas for GC analysis.

An air tight syringe was used for sampling from the vacuum sealed chamber. The Raman spectra of the photoanode were recorded using a Renishaw InVia spectrometer coupled with a 514 nm excitation source. The bandgap energy (E_g) of the prepared samples were determined from Tauc plots, *i.e.* $(\alpha h\nu)^{2 \text{ or } 1/2}$ as a function of $h\nu$. Steady-state photoluminescence (PL) and time-resolved PL (TRPL) spectra were obtained by a Horiba Jobin Yvon Fluorolog-3 fluorescence spectrometer.

3 PHASE-JUNCTION FOR IMPROVING THE PEC EFFICIENCY

This chapter is based on the paper "*Phase-junction design of MOF-derived TiO_2 photoanodes sensitized with Quantum Dots for efficient hydrogen generation*" published on *Applied Catalysis B: Environmental, 263 (2020) 118317*.

Due to enhanced carrier transfer and separation in the interface region of two different phases in close contact, heterojunction formation is a highly effective strategy for designing highly active photocatalyst systems. If a composite consisting of different phases of one material (e.g., rutile, anatase, and brookite, all crystal phases of TiO_2) will be called "multiphase" heterojunction material, different crystal phases can exhibit different band positions and/or E_g. A lot of multiphase heterojunctions have been recently reported that can dramatically increase the photocatalytic activities of the corresponding particulate semiconductors due to efficient separation and transfer of photogenerated charges between the different phases, such as anatase/rutile[162, 163], α-Ga_2O_3/β-Ga_2O_3[164], α-Bi_2O_3/β-Bi_2O_3[165], and β-TaON/γ-TaON[166].

Since 1972, TiO_2 became one of the most extensively investigated MO semiconductors for PEC water splitting, due to its chemical stability and nontoxicity[167]. One promising route to enhance the photocatalytic potential of TiO_2 is to engineer the polymorph composition. Anatase and rutile TiO_2 are commonly used as photocatalysts with E_g of 3.20 eV and 3.0 eV, respectively. Often, anatase is considered to be the most active due to better electron affinity[168], ionisation potential[163], and lower recombination rate[169]. Whereas rutile TiO_2 can capture more light due to a narrower band gap, anatase phase of TiO_2 has a conduction band level higher by 0.2 eV, providing higher driving force for the water reduction reaction. Both of them are composed of TiO_6 octahedra with each Ti^{4+} ion surrounded by six O^{2-} ions. However, rutile octahedra share two edges, while anatase octahedra share four edges[37, 170, 171]. This results in longer Ti-Ti distance and shorter Ti-O distance with lower symmetry in anatase TiO_2. At the anatase/rutile interface, the space charge layer is built, leading to band bending. As a result, the electric field at the interface will promote the charge separation and suppresses the charge recombination[163, 172, 173]. It is postulated that photogenerated electrons can transfer from anatase to rutile, and the holes can transfer in an opposite direction[174, 175].

Evonik-Degussa Aeroxide TiO_2 P25 (P25), as the most extensively used commercial TiO_2 photocatalyst powder materials, consists of a mixture of anatase and rutile with ratio ~80:20 phase composition (varies with different reports). It has proposed a synergetic effect between anatase and rutile to be responsible for its high photoreactivity by Bickley et al. in 1991[176]. Ohno et al. found the close contact between rutile and anatase in P25 to be prerequisite for the synergetic effect, via investigating the photocatalytic naphthalene oxidation on pure anatase, pure rutile, and P25[177, 178]. Pan et al. reported that a 30%/70% rutile/anatase

mixed powder has been found to make the best photocatalyst for the oxidation of organics when applied to treat wastewater[179]. However, due to rapid phase transition in a narrow temperature window, it is not easy to control the ratio of anatase to rutile in a material. Therefore, there has been an intensive debate about the synthetic approach to mix rutile and anatase nanoparticles in order to systematically vary the anatase-to-rutile ratio.

As seen in 1.4, through MOF-template method, we could design the MO with the desired properties. Based on this, we found that during the thermal decomposition of the NH_2-MIL-125(Ti), the phase transition of derived TiO_2 has been observed, which means that by careful controlling the parameters of annealing processing, the phase of the derived TiO_2 can be tuned[180].

Hence, in this chapter, NH_2-MIL-125(Ti) makes an excellent candidate to be used as sacrificial template to synthesize TiO_2 with tuned morphology and crystal phase. Moreover, due the large bandgap of TiO_2 (e.g. anatase: 3.2 eV) limits its absorption to wavelengths only in the ultraviolet region (which represents less than 5% of the solar spectrum), meaning that TiO_2 cannot exploit the visible and infrared light emitted by the sun. Colloidal quantum dots (QDs) were utilized as the sensitiezer to to enhance solar absorption. Therefore, we prepared a anatase/rutile (A/R) mixed phase TiO_2 and sensitized it with QDs for water splitting. The role of mixed phase TiO_2 in charge transfer was investigated and analysized.

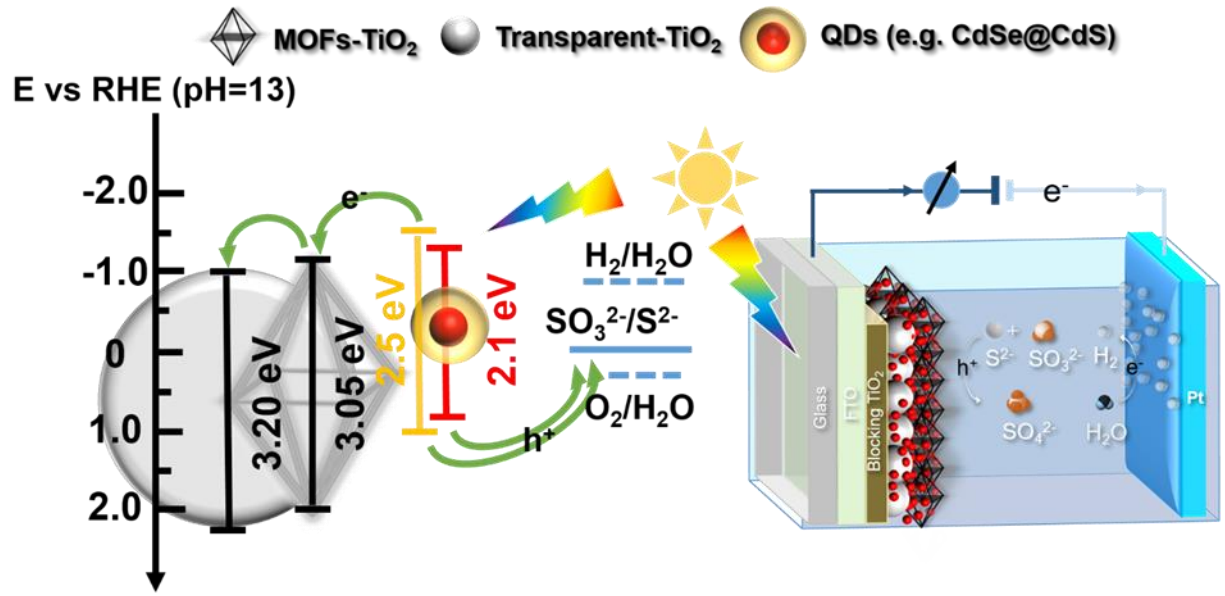

Figure 3.1 Band alignment and schematic diagram of PEC cell.

3.1 Experimental sections

See section 2.2.1, The NH_2-MIL-125(Ti) was synthesized through the solvothermal method. In comparison to the parent MIL-125, NH_2-MIL-125(Ti) exhibits higher water stability and its synthesis process is easy to prepare and highly reproducible[115]. On the other hand, Kyriakos' group employed different MOF or no MOF template methods to prepare the different kind of mixed phase TiO_2[118] and compared their photocatalytic performance. Their study demonstrated that optimum NH_2-MIL-125(Ti)-derived TiO_2 notably outperformed the commercial P25 Degussa, the conventionally synthesized TiH_4O_4, and MIL-167-derived TiO_2. Therefore, we selected the NH_2-MIL-125(Ti) as the precursor for synthesizing the mixed phase TiO_2 among several Ti-containing MOFs.

The morphology of the NH_2-MIL-125(Ti) can be controlled by simply modulating the reaction time of the reactants during crystallization, which ranges from the circular plate through tetragon to octahedron. A similar experiment was also conducted. We first heated the Teflon-lined stainless-steel autoclave for 24 hours. Upon cooling, we obtained the yellow suspension, which we then examined with SEM (Figure 3.2a). We also extended the reaction time to 72 hours as a comparison. After that, we obtained the same yellow suspension with circular plate morphology (Figure 3.2b). Finally, we picked 24 hours as our reaction time.

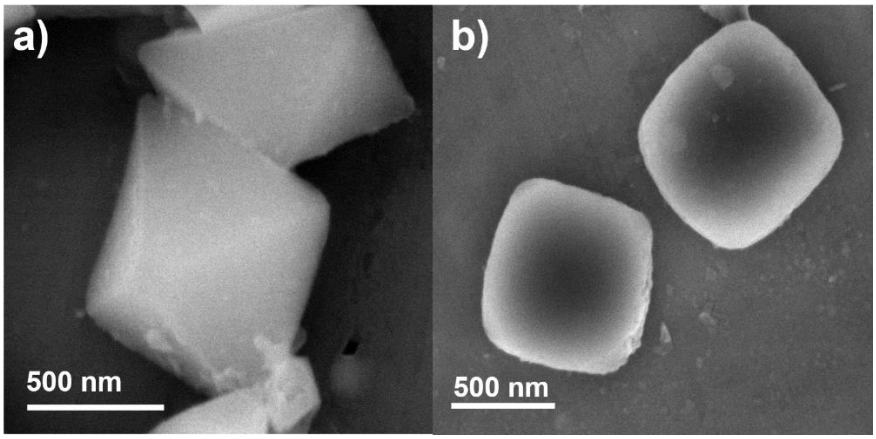

Figure 3.2 SEM images of synthesized NH_2-MIL-125(Ti) precursor (a 24 hours and b 72 hours).

In addition, we would like to design the TiO_2 with anatase and rutile mixed phase. By manipulating pyrolysis temperature, previous research indicates that amorphous, anatase, rutile, and mixture phases of TiO2 can be obtained in a controlled manner[180]. determine the optimal temperature for constructing the optimal ratio of anatase to rutile. Due to the rapid phase transition in a narrow temperature window, the anatase phase is a metastable crystalline. Thus, we conducted numerous temperature tests. We have listed average temperatures here. We selected 425 ℃, 500 ℃, and 575 ℃ to anneal the Ti-MOF for comparison. At 425 °C, we can only obtain the anatase phase. (Figure 3.3). When the temperature exceeded 425 °C, the

rutile phase appeared. At 500 °C, we then obtained the anticipated ratio of anatase and rutile, which is 70%/30%. (Figure 3.5). As the temperature continued to rise, the phase changed rapidly, and the rutile phase came to dominate the material. Finally, at 575 °C, the M-TiO_2 contained pure rutile. (Figure 3.5). We therefore set the annealing temperature to 500 °C.

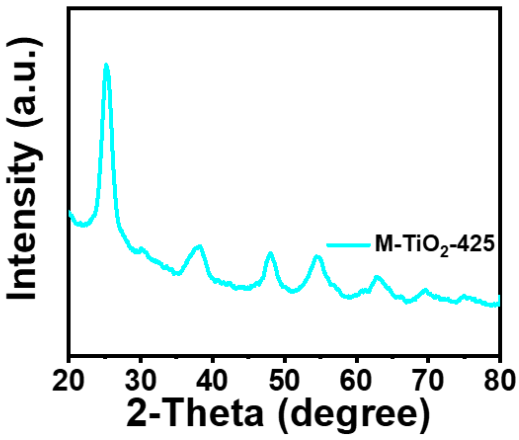

Figure 3.3 XRD patterns of the M-TiO_2-425.

At the beginning of the 2.5.4 section, we prepared two layers of photoanodes using M-TiO_2 paste. We found that no matter what kind of QDs we used, the current densities were quite low. The reason for this is the fact that photoanodes only require one direction of holes generated by light. It is quite likely that the rutile/anatase phase would act in the opposite way, reducing photocurrent density, if the anatase/rutile phase improved it[162]. As a result of this synthetic method, the phase that contacts the FTO cannot be controlled. As a result, the charge separation effect of mixed phase would tend to be zero. Based on the discussion above, we redesigned the experiment by which we used an anatase layer of 18 NR-T paste as a first layer in contact with the FTO. On top of this layer, we deposited a second layer of M-TiO_2 (or commercial TiO_2 as reference). For the M-TiO_2 paste, the final configuration of the PEC cell is A+A/R while for C-TiO_2 is A+A. In this situation, we could make sure that in our PEC system the first layer was always an anatase phase of TiO_2.

For the time-resolved PL lifetime, the measured charge carrier lifetime shows how long it takes for the electron-hole pairs to decay to their "1/e" by radiative recombination. If it is a single system contains a radiative decay and a non-radiative decay component, a longer lifetime means a higher charge separation[181]. However, if there is a composite system, a further mechanism should be considered: the charge transfer component[182]. The short lifetimes are attributed to either trapping (like QDs coupled to SiO_2) or a convolution of trapping and electron transfer (e.g., QDs coupled to SnO_2, TiO_2, and ZnO). In our

case, the short fluorescence lifetimes are caused by the electron transfer by QDs to TiO_2. With increasing time most of these injected electrons inside TiO_2 recombine with holes remaining within neighboring CdSe QDs (Reaction 4), causing the signal from this particular transient state to be nearly diminished after film excitation. The reaction undergoes 4 steps, as follows (e.g., CdSe/TiO_2):

$$\mathbf{CdSs + h\nu \rightarrow CdSe(h^+ + e^-)} \quad \textbf{(3.1)}$$

$$\mathbf{CdSe(h^+ + e^-) \rightarrow CdSe + h\nu'} \quad \textbf{(3.2)}$$

$$\mathbf{CdSe(h^+ + e^-) + TiO_2 \rightarrow CdSe(h^+) + TiO_2(\mathit{e}^-)} \quad \textbf{(3.3)}$$

$$\mathbf{CdSe(h^+) + TiO_2(\mathit{e}^-) \rightarrow CdSe + TiO_2} \quad \textbf{(3.4)}$$

If the electron transfer is thermodynamically unfavourable (e.g., CdSe/ZrO_2), the fluorescence lifetime spectrum will not show a decrease but will maintain a longer lifetime than CdSe/TiO_2.

3.2 Results and discussions

3.2.1 Morphological and optical characterizations

As shown in Figure 3.4, the synthesized NH_2-MIL-125(Ti) exhibits a well-defined octahedral morphology and its crystal structure is confirmed by XRD (Figure 3.5). The results are in accordance with previous reports confirming the formation of the MOF structure[116]. Therefore, the NH_2-MIL-125(Ti) can be used as an ideal sacrificial precursor and template to synthesize the anatase-rutile phase junctions TiO_2[180]. The anatase and rutile mix-phase M-TiO_2 was obtained through the control of the thermal decomposition of NH_2-MIL-125(Ti) at 500 °C in air.

SEM and TEM images showed that the structure of M-TiO_2 inherited the structural features of the octahedral NH_2-MIL-125(Ti) precursor (Figure 3.4d and e), but when compared to the original MOF (the Figure 3.4c and e), the M-TiO_2 has been shrunk and truncated, mainly due to the loss of C and H of organic ligands after thermolysis[116]. The surface of the M-TiO_2 became rougher compared with the NH_2-MIL-125(Ti) precursor, due to the decomposition of organic ligands and channels created by the gas released during the thermolysis process[116]. HRTEM imaging (Figure 3.4f) confirmed the high crystallinity of M-TiO_2 lattice fringes. In particular, it was possible to observe the simultaneous presence of anatase and rutile phases: the (110) plane of the rutile lattice, which corresponded to a lattice spacing of 0.32 nm, could be clearly observed. In addition, the lattice spacing of the neighboring area was 0.35 nm which can be assigned to the (101) plane of the anatase lattice[183].

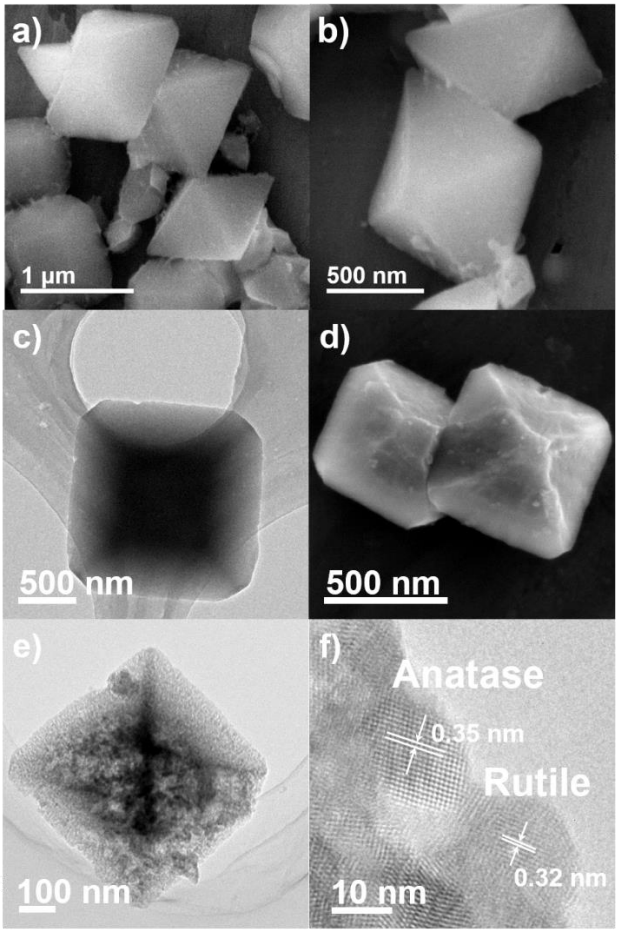

Figure 3.4 SEM images (a and b) of synthesized NH_2-MIL-125(Ti) precursor, TEM image of NH_2-MIL-125(Ti) precursor (c); SEM (d) and TEM (e) images of M-TiO_2 and HRTEM image of M-TiO_2 (f).

The crystalline phase of M-TiO_2 was also investigated by XRD. Figure 3.5 compares the crystallinity of M-TiO_2, C-TiO_2 and M-TiO_2-575. Compared to the C-TiO_2 which presented only the peaks of the anatase phase, two titania polymorphs, i.e., tetragonal rutile (JCPDS No. 21-1276) and tetragonal anatase (JCPDS No. 21-1272), were identified in the M-TiO_2. In the XRD pattern of M-TiO_2, the diffraction peak located at 2θ of 27.4° corresponded to the rutile crystalline phases. Meanwhile, it is also possible to identify the anatase phase from the peak located at 2θ of 25.3°. In addition, by comparing the peaks of the rutile (110) and anatase (101) we can estimate the percentage of the rutile TiO_2 in the sample[184]. The rutile concentration (Rut%) can be calculated by Eq 3.5, in terms of either the intensity ratio or the area ratios of the R (110) and A (101) X-ray diffraction data. In our case, the M-TiO_2 contain 30.8% of rutile TiO_2, which is the best percentage for photocatalysis[179].

$$\mathbf{Rut\%(Int)} = \frac{\boldsymbol{Int_{R(110)}}}{\boldsymbol{Int_{R(110)} + Int_{A(101)}}} \; \boldsymbol{and} \; \mathbf{Rut\%(Area)} = \frac{\boldsymbol{Area_{R(110)}}}{\boldsymbol{Area_{R(110)} + Area_{A(101)}}} \quad \mathbf{(3.5)}$$

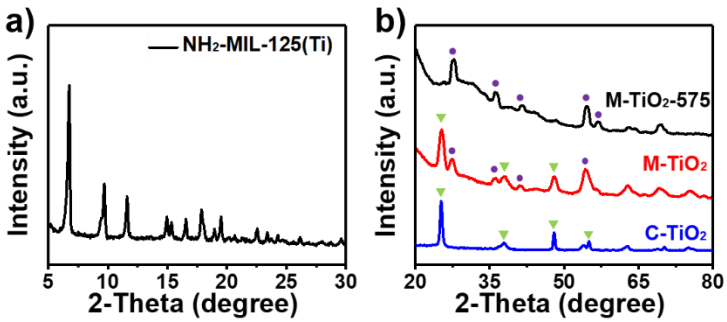

Figure 3.5 XRD patterns of the NH_2-MIL-125(Ti) precursor (a); and that of the M-TiO_2 (red), C-TiO_2 (blue) and M-TiO_2-575 (black) (b) (green triangle: anatase-phase TiO_2; purple dot: rutile-phase TiO_2).

Based on the results of HRTEM and XRD, the presence of an anatase-rutile phase junction in the M-TiO_2 can be confirmed. During the experimental process, it was found that the presence of the MOF as well as the control of the temperature were both critical factors to obtain the mixed phase of TiO_2. In fact, if the temperature was raised to 575 °C, we observed that the TiO_2 forms only the pure rutile phase. In the meantime, C-TiO_2 exhibits only the anatase phase.

In addition, light trapping and scattering at both the front and the back sides of the nanoparticles can increase the effective optical path length as it depends on the geometry of the nanoparticles[185, 186]. Figure 3.6a displays the transmittance of M-TiO_2 and the C-TiO_2 thin film. In particular, the thin M-TiO_2 film presents a transmittance of 13.2% (at λ = 500 nm), whereas the transmittance of C-TiO_2 thin film is around 28.8%. This result suggests that the M-TiO_2 thin film possess better light scattering properties, which may be ascribed to its morphology, that can positively contribute in improving the efficiency of the M-TiO_2 based PEC cell. The PL and UV-DRS of C-TiO_2, M-TiO_2, M-TiO_2/CdSe@CdS and M-TiO_2/CdSe are also shown in Figure 3.6b and c. Figure 3.6b shows the absorption spectra of C-TiO_2 and M-TiO_2 in the UV-visible region. After EPD with QDs, the results show the presence of the first excitonic absorption peak corresponding to the QDs. The emission of pure C-TiO_2 and M-TiO_2 are almost absent while for M-TiO_2/QDs it is possible to detect the emission of QDs (even if it is quenched compared to the emission of QDs suspended in solution). In addition, the PL peak of M-TiO_2/QDs is almost at the same location of the corresponding pure QDs.

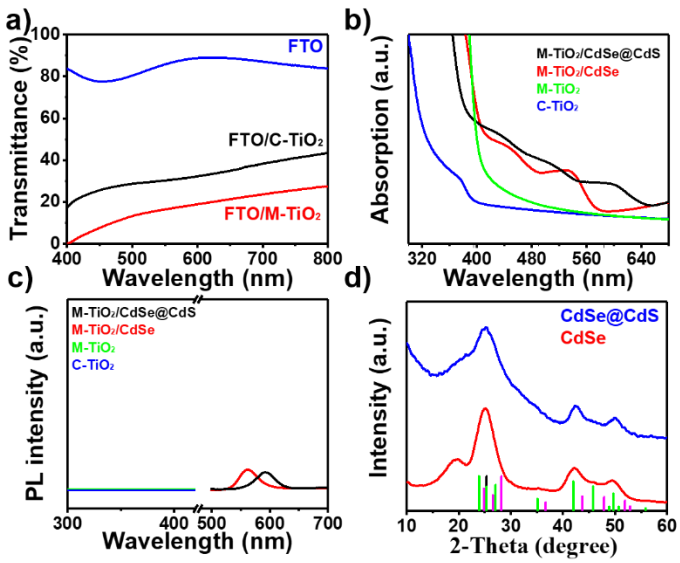

Figure 3.6 (a) Plots of transmittance versus wavelength for FTO, FTO/C-TiO_2 and FTO/M-TiO_2; (b) DRS-UV spectra of C-TiO_2, M-TiO_2, M-TiO_2/CdSe and M-TiO_2/CdSe@CdS; (c) PL spectra of C-TiO_2, M-TiO_2, M-TiO_2/CdSe and M-TiO_2/CdSe@CdS; (d) XRD of CdSe QDs or core@shell CdSe@CdS QDs, the Joint Committee on Powder Diffraction Standards (JCPDS) card files for CdSe (00190191, black for ZB and 08-459, green for WZ) and CdS (01-077-2306, Magenta for WZ) are shown for identification.

We used XPS to determine the surface chemical composition of C-TiO_2 and M-TiO_2 (Figure 3.7). For both C-TiO_2 and M-TiO_2, the survey spectra revealed the presence of Ti, O and C peaks (Figure 3.7a and b). No peak for N element was detected in the M-TiO_2, in agreement with previous reports, confirming that the amine group of the original MOF does not introduce N as dopant in the TiO_2[187, 188]. The high-resolution spectrum of Ti 2p consists of two strong peaks, 458.5 eV and 464.2 eV for C-TiO_2, 458.3 eV and 464.0 eV for M-TiO_2, can be assigned to Ti $2p_{3/2}$ and Ti $2p_{1/2}$, respectively (Figure 3.7c and d). These two symmetric peaks correspond to Ti^{4+} of TiO_2[189]. The careful comparison of the Ti $2p_{3/2}$ peak of C-TiO_2 and M-TiO_2 revealed a shift of about 0.199 eV in case of M-TiO_2. Previous reports showed that the shift of the Ti $2p_{3/2}$ peak towards lower values corresponds to oxygen vacancies or defects because the Ti-O-Ti bond would be weakened by the high temperature treatment[190]. The absence of a peak around 455-456 eV (which usually indicates the presence of Ti-N bonds) (Figure 3.7d)[191, 192], confirms that nitrogen does not act as dopant in the M-TiO_2. The peaks of O 1s were positioned at about 529.8 eV and 529.5 eV corresponding to the lattice oxygen (Ti-O) for TiO_2[193]. The peak in both samples observed at binding energies of 531.5 eV and 531.1 eV, respectively, can be assigned to surface-adsorbed hydroxyl groups (Figure 3.7e and f)[194].

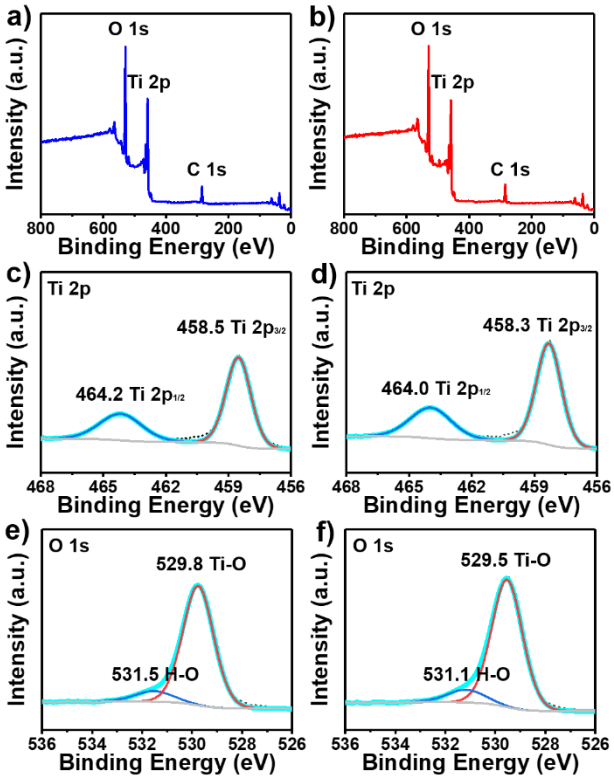

Figure 3.7 XPS survey spectra of C-TiO_2 (a) and M-TiO_2 (b); High resolution Ti 2p spectra for (c) C-TiO_2 and (d) M-TiO_2. High resolution O 1s spectra for (e) C-TiO_2 and (f) M-TiO_2.

The optical properties of the as-synthesized QDs in solution are reported in Figure 3.8. Both QDs showed a broad absorption spectrum ranging from the UV to visible region with the first-excitonic peaks located at 535 nm for CdSe while the core-shell structure, CdSe@CdS, presented a red-shift of the onset to 577 nm (Figure 3.8a). The PL emission spectra are centered at 560 nm and 603 nm for CdSe and CdSe@CdS, respectively. Figures 3.8b and c report the TEM images of CdSe and CdSe@CdS. Both samples exhibit a quasi-spherical shape with uniform size distribution, 2.95 ± 0.03 nm and 4.50 ± 0.05 nm respectively. The successful deposition of the QDs on the M-TiO_2 films after EPD process is also confirmed by the TEM images (Figure 3.8d).

The XRD patterns (see Figure 3.6d) reveal that the CdSe has a zinc blende (ZB) crystal structure, as expected from the synthesis conditions. After growing the CdS shell over the CdSe core via SILAR, in the diffraction patterns of core/shell QDs it is possible to also observe the presence also of peaks from CdS hexagonal wurtizite (WZ) phase. This XRD pattern could correspond to either CdS_xSe_{1-x} alloy or CdSe/CdS core-shell nanocrystals. However, if a CdS_xSe_{1-x} alloyed nanocrystal had formed, there would be a blue shift of absorption and PL spectra because of the larger band gap energy of CdS_xSe_{1-x} compared to pure

CdSe[195, 196]. Instead, as shown in Figure 3.8a, the absorption and emission after the growth of the CdS shell are red-shifted, indicating the formation of a core/shell structure.

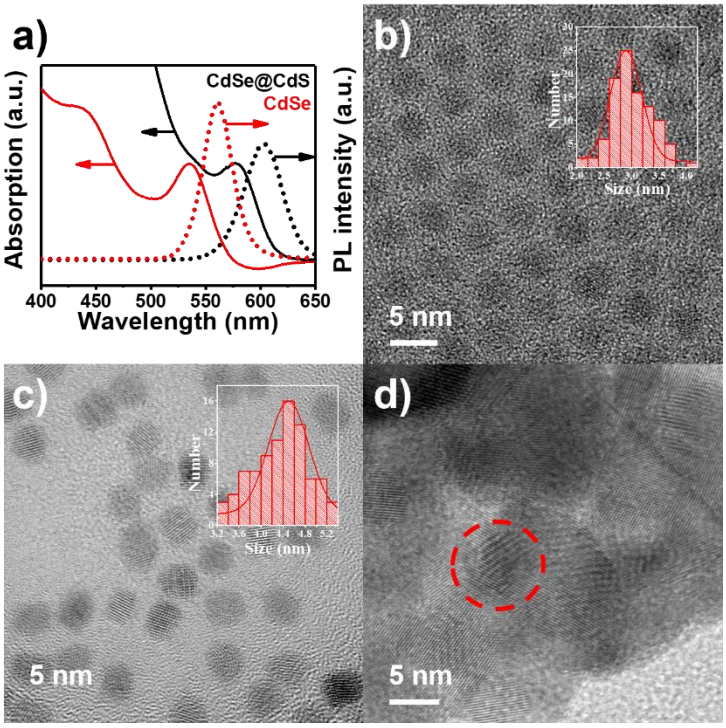

Figure 3.8 (a) UV adsorption and PL intensity of CdSe and CdSe@CdS; (b) TEM image of CdSe. The inset image exhibits the average size of CdSe; (c) TEM image of CdSe@CdS. The inset image exhibits the average size of CdSe@CdS; (d) CdSe@CdS QDs in the TiO_2 film, highlighted in the circle.

3.2.2 Properties of PEC cells

The PEC activity of the different QDs-sensitized M-TiO_2 and C-TiO_2 photoanodes was tested, as shown in Figure 3.9 and the results are summarized in Table 3.1. The N_2-purged 0.25 M Na_2S and a 0.35 M Na_2SO_3 aqueous solution (pH~13) were used as sacrificial hole scavenger to prevent QDs photocorrosion.

Table 3.1 Photocurrent density and device stability parameters.

Samples	Photocurrent density (at 0.9 V vs RHE) (mA·cm^{-2})	Retention of photocurrent (first 180 seconds) (%)	Retention of photocurrent (after 7200 seconds) (%)
M-TiO_2/CdSe@CdS	10.72	97.4	78.1
C-TiO_2/CdSe@CdS	7.24	70.8	57.5
M-TiO_2/CdSe	7.55	95.3	76.9

C-TiO_2/CdSe	6.87	69.8	42.1

All measurements were performed under dark, continuous and chopped illumination. For all the samples, under light condition (1 sun, 100 mW/cm^2) the photocurrent density (J) gradually increases with the increase in voltage, until a saturated current density is obtained (Figure 3.9a). Chopped-light linear sweep voltammetry measurements on the different photocathodes are reported in Figure 3.10. In the absence of QDs, C-TiO_2 presents a maximum photocurrent density ~0.3·mA cm^{-2} while the photoanode based on M-TiO_2 exhibits a photocurrent of 0.42 mA·cm^{-2}. This suggests that the increased photocurrent density of the QDs/TiO_2 photoanode is due to the contribution from the QDs. However, with sensitization by CdSe QDs and CdSe@CdS QDs, a photocurrent is seen immediately upon light irradiation for all photoanodes. The photocurrent from M-TiO_2/CdSe@CdS is clearly superior to those obtained from analogous photoanodes but sensitized with only CdSe QDs or made with pure anatase photoanodes, independently of the kind of QDs employed.

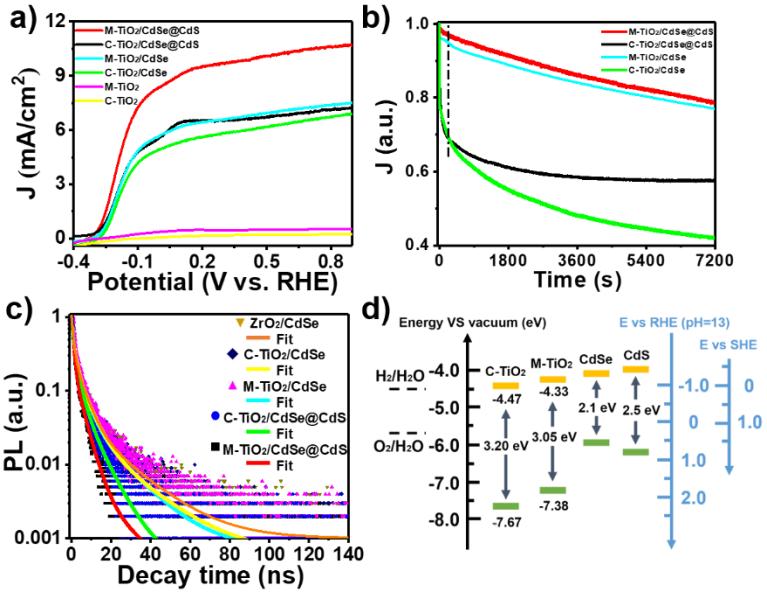

Figure 3.9 (a) Photocurrent density potential dependence of M-TiO_2 and C-TiO_2 sensitized by CdSe and CdSe@CdS; (b) Stability measurements (photocurrent density as a function of time) of M-TiO_2 and C-TiO_2 sensitized by CdSe and CdSe@CdS photoanodes at 0.4 V versus RHE under AM 1.5 G illumination (100 mW/cm^2); (c) Transient PL spectra of ZrO_2/CdSe, C-TiO_2/CdSe, M-TiO_2/CdSe, C-TiO_2/CdSe@CdS and M-TiO_2/CdSe@CdS; (d) Summary of the energy levels obtained from UPS measuraments. The CdSe and CdS energy levels are taken from[182].

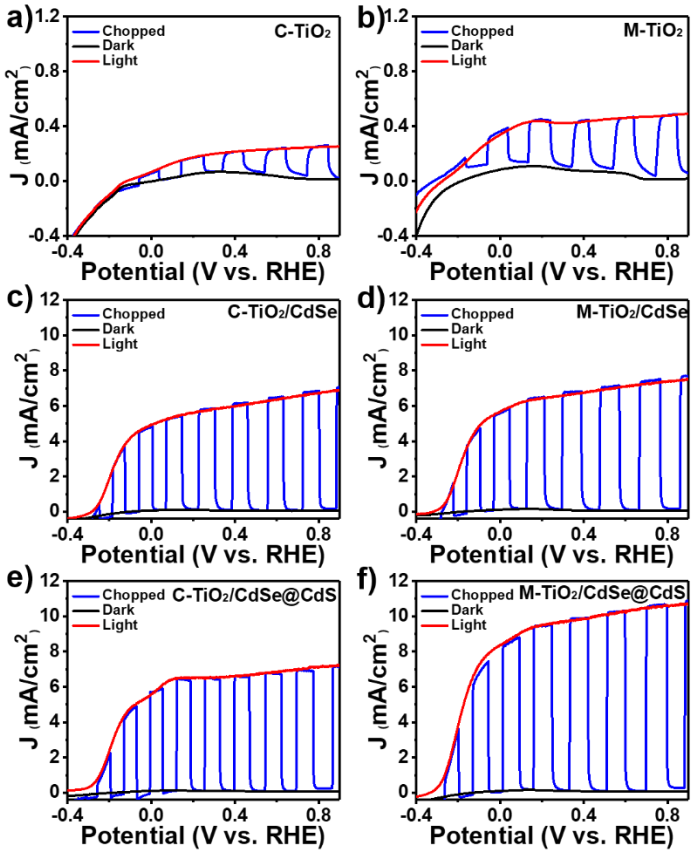

Figure 3.10 All the samples PEC performance under dark, continuous and chopped illumination. (a) C-TiO_2; (b) M-TiO_2; (c) C-TiO_2/CdSe(d) M-TiO_2/CdSe(e) C-TiO_2/CdSe@CdS and (f) M-TiO_2/CdSe@CdS.

In particular, the highest saturated photocurrent density of the PEC system based on M-TiO_2/CdSe photoanode was 7.55 mA/cm^2 (at 0.9 V vs RHE), which was around 10% higher than C-TiO_2/CdSe photoanode (6.87 mA/cm^2). By employing the core-shell QDs, the M-TiO_2/CdSe@CdS photoanode achieved 10.72 mA/cm^2 under the same conditions, a 47.6% enhancement compared to C-TiO_2/CdSe@CdS photoanode (7.24 mA/cm^2). The same experiment was also carried out for M-TiO_2-575 under same condition. The current density was only 5.26 mA/cm^2 (Figure 3.11a), value lower than both M-TiO_2 and C-TiO_2. The reason, as also reported elsewhere, is that pure-phase rutile is normally inactive to photocatalysts due to rapid recombination rates[169, 197-199]. When employing the M-TiO_2 substrate, a higher current density can be achieved. The reason could be attributed to a synergistic effect: (i) Benefiting from the favourable electronic band alignment of the M-TiO_2/QDs, a larger number of both electrons and holes can be extracted from QDs into M-TiO_2, thereby contributing to the current density. Due to the efficient electron transfer, electron accumulation and oxidation were largely suppressed. (ii) According to charge dynamics analysis, with the existence of a mixed phase TiO_2, the spatial separation of electrons and holes increases, further reducing recombination effects[175].

In addition, the IPCE measurements of representative samples of M-TiO_2/QDs and C-TiO_2/QDs photoanodes were carried out under one sun illumination (AM 1.5 G, 100 mW·cm^{-2}). A systematic comparison of the IPCE values calculated at 0.9 V vs RHE for a PEC device with the M-TiO_2/QDs and C-TiO_2/QDs photoanodes is shown in Figure 3.11b. The IPCE values of a PEC device with a M-TiO_2/QDs photoanode are clearly higher than those of a PEC device with a C-TiO_2/QDs photoanode over the whole visible spectrum. These results are consistent with the obtained differences in the photocurrent density values for the PEC devices with the M-TiO_2/QDs and C-TiO_2/QDs photoanodes.

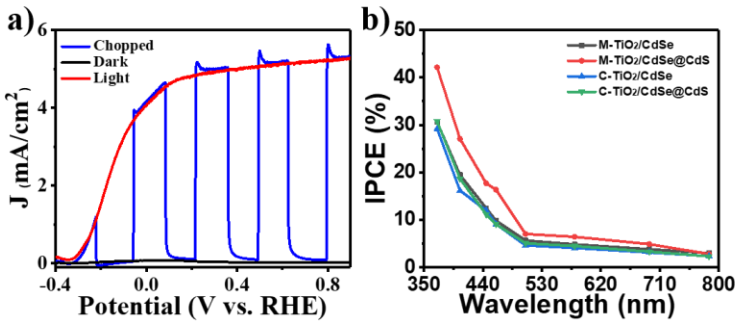

Figure 3.11 (a) Photocurrent density potential dependence of M-TiO_2-575/CdSe and (b) IPCE spectra of PEC devices based on M-TiO_2/QDs and C-TiO_2/QDs photoanodes measured at 0.9 V vs RHE under one sun illumination (AM 1.5 G, 100 mW·cm^{-2}).

Another important aspect for PEC devices is their long-term stability. The stability of the QDs sensitized TiO_2 photoanode PEC devices (photocurrent vs. time evolution) was measured at 0.4 V vs RHE under AM 1.5 G solar illumination (100 mW/cm^2) (Figure 3.9b). To better visualize the decay trends, the photocurrent densities of the photoanodes were normalized to their maximum values. The *J* of both QDs sensitized C-TiO_2 photoanodes rapidly decays within 180 s, maintaining only around 70% of the initial values. For C-TiO_2/CdSe, the decay rate was very rapid, retaining only 42.07% of its initial value after 7200 s. For C-TiO_2/CdSe@CdS, the *J* reached a fairly stable value after 3600 s, maintaining only 57.5% of its initial value after 2 h. The different stability between the core-shell QDs and pure QDs during the device operations is due to the presence of a higher amount of surface defects in the core-only QDs which act as charge traps, lowering the photoconversion and increasing the photocorrosion of QDs, thus reducing their long-term stability[200, 201]. However, a thicker shell could efficiently isolate the core material from the QDs surface chemistry and the surrounding chemical environment[202]. Therefore, core-shell structure QDs possess an enhanced photocurrent and stability due to their excellent properties such as reduced surface traps, suppressed charge recombination and enhanced photo- and chemical- stability[203, 204]. On the other hand, the photocurrent values of M-TiO_2/CdSe@CdS and M-TiO_2/CdSe, within the first 180 seconds did not decrease, maintaining 97.4% and 95.3%, of their initial values, respectively. Even after 2 h of continuous

operation, the M-TiO_2 samples remarkably retained more than 78.1% (M-TiO_2/CdSe@CdS) and 76.9% (M-TiO_2/CdSe) of their initial value.

To understand the mechanism behind the improved efficiency and stability, different experiments were performed. The carrier dynamics of the QDs after coupling with the semiconductor metal oxide were investigated through transient fluorescence spectroscopy. In this measurement, ZrO_2 was used as a benchmark system as, due to its electronic band alignment (E_g = 5 eV) electron transfer cannot occur. Thus, PL differences could be uniquely attributed to radiative/non-radiative exciton recombination[182]. To evaluate the electron lifetime and transfer rate of QDs deposited on M-TiO_2, C-TiO_2 and ZrO_2 films, the PL lifetime of the five samples was studied under excitation at λ_{ex} = 444 nm, by monitoring the emission at the PL peaks (Figure 3.9c)[205]. All the PL decay curves were well fitted by a three-component exponential decay, and all the fitted parameters were provided in Table 3.2. The intensity-weighted average lifetime ($\langle\tau\rangle$) is calculated by using the following equation 3.6[206]:

$$\langle\boldsymbol{\tau}\rangle = \frac{\boldsymbol{\alpha_1\tau_1^2 + \alpha_2\tau_2^2 + \alpha_3\tau_3^2}}{\boldsymbol{\alpha_1\tau_1 + \alpha_2\tau_2 + \alpha_3\tau_3}} \quad (\mathbf{3.6})$$

Where α_i (i = 1, 2, 3) were the coefficients of the fitting of PL decay and τ_i (i = 1, 2, 3) were the characteristic lifetimes, respectively. From Table 3.3, it can be observed that the PL decay was faster in the case of QDs deposited on M-TiO_2 compared to QDs on C-TiO_2, indicating that charge transfer is more efficient in the former film. On the other hand, when compared with the ZrO_2/QDs film, all the TiO_2/QDs exhibited faster PL decay because of the electron transfer from the QDs to TiO_2. The charge-transfer rate constant (K_{et}), with different TiO_2 films, was estimated using the following equation 3.7[203]:

$$\boldsymbol{K_{et}} = \frac{\mathbf{1}}{\boldsymbol{\tau_{QDs/TiO_2}}} - \frac{\mathbf{1}}{\boldsymbol{\tau_{QDs/ZrO_2}}} \quad (\mathbf{3.7})$$

where $\langle\ \tau\ \rangle$ QDs/TiO_2 and $\langle\ \tau\ \rangle$ QDs/ZrO_2 are the average electron lifetimes of the QDs with TiO_2 and QDs with ZrO_2, respectively. As shown in Table 3.3, the K_{et} value of M-TiO_2/CdSe and M-TiO_2/CdSe@CdS were 4.85 10^7 s^{-1} and 11.85 10^7 s^{-1} which were higher than that of C-TiO_2/CdSe and C-TiO_2/CdSe@CdS (K_{et} = 3.60 10^7 s^{-1} and 9.04 10^7 s^{-1}). This could be attributed to a more favourable electronic band alignment of the QDs with the anatase/rutile phase. In addition, the sample with core/shell QDs present the shorter average lifetime and highest charge transfer rate[207-209], confirming that the combination of MOF-derived TiO_2 and core/shell QDs can yield the highest PEC performance.

Table 3.2 Fitted parameters by a three-component exponential decay.

Parameters	M-TiO_2/ CdSe@CdS	C-TiO_2/ CdSe@CdS	M-TiO_2/CdSe	C-TiO_2/CdSe	ZrO_2/CdSe
α_1	45.81	69.47	52.91	29.61	52.82
α_2	41.24	10.23	40.98	55.00	11.76
α_3	12.96	20.31	6.11	15.96	35.43
τ_1 (10^{-8} s)	0.29	0.40	0.40	1.96	1.03
τ_2 (10^{-8} s)	0.81	1.58	1.50	0.53	5.14
τ_3 (10^{-8} s)	0.06	0.09	0.07	0.15	0.23
R-Square	0.9939	0.9972	0.9965	0.9946	0.9964
Reduced Chi-Sqr	2.80 10^{-5}	1.38 10^{-5}	1.91 10^{-5}	3.25 10^{-5}	2.09 10^{-5}

Table 3.3 Average lifetime and charge transfer rate calculated from the luminescence decay dynamics.

Samples	Average lifetime (ns)	K_{et} (10^7 s^{-1})
M-TiO_2/CdSe@CdS	6.58	11.85
C-TiO_2/CdSe@CdS	8.07	9.04
M-TiO_2/CdSe	12.2	4.85
C-TiO_2/CdSe	14.4	3.60
ZrO_2/CdSe	29.9	-

To further investigate the effect of the mixed phase on the band alignment of M-TiO_2 and C-TiO_2, UPS analysis has been carried out. The energy bandgaps of M-TiO_2 film and C-TiO_2 film were calculated to be ~3.05, and 3.20 eV, according to the classical Tauc's formula (Figure 3.12), respectively[210]. UPS with He I radiation (21.21 eV) was used to estimate the Fermi level and valance band maximum (VBM) energy level. Thus, the conduction band minimum (CBM) level values of the TiO_2 films could be determined by the VBM and bandgap (the detailed analysis are reported in Figure 3.12b and c). All of the above energy

level results are summarized in Figure 3.9d. The precise band alignment and schematic diagram of QDs-sensitized photoanode for PEC cell are illustrated in Figure 3.1.

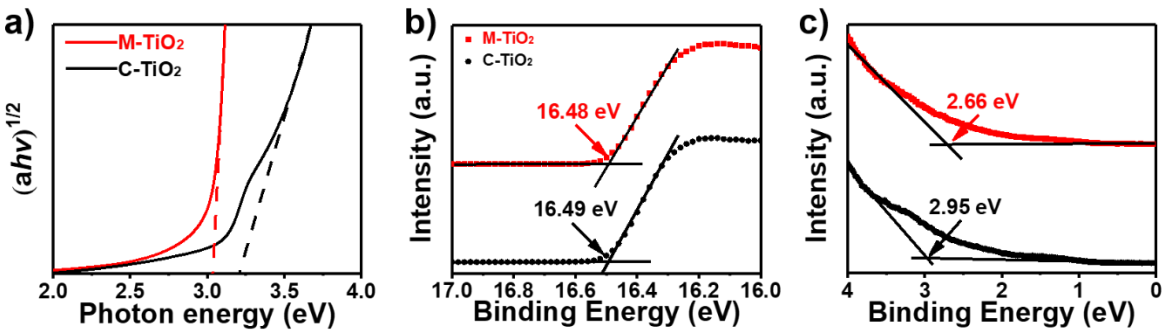

Figure 3.12 The extrapolation of Tauc plots ($(\alpha h\nu)^{1/2}$ versus photon energy ($h\nu$)) for the M-TiO_2 and C-TiO_2 films (a); High binding energy cut-off (b) and low binding energy cut-off (c) of UPS spectra of M-TiO_2 and C-TiO_2.

We observed a shift of the VBM in the A/R phase and a reduced band gap. These shifts can have a positive influence on the charge transfer. The presence of the mixed-phase will contribute to promote charge separation and suppresses charge recombination between TiO_2 nanoparticles, even if the 'internal' charge separation due to the rutile/anatase is not directly observable due to ensemble effect that hides the contributions of the single phases[183]. The main effect will be then an improved efficiency and stability because the oxidation of the QDs could be reduced by removing the generated holes and electrons more rapidly.

To fully understand the mechanism responsible for the different performances of M-TiO_2 and C-TiO_2, the charge transfer characteristics of the photoelectrodes were investigated using EIS. Figure 3.13a and b report the Nyquist plots recorded at 0.4 V versus RHE under 1 Sun (100 mW/cm^2) of representative samples of M-TiO_2 and C-TiO_2, with and without QDs. The diameter of the semicircle at the far-left correlates with the charge transfer resistance. In particular, it can give information on the charge transfer kinetics at the interface between the photoanode and the electrolyte. The data have been fitted with the following model (inset image in Figure 3.13b): A Randles equivalent circuit consisting of a series resistance (R_S), space charge capacitance and resistance (C_{SC} and R_{SC}), double layer capacitance (C_{DL}), charge transfer resistance (R_{CT}) and a Warburg element (W). Analogous models have been already developed for similar heterostructured materials[211-213].

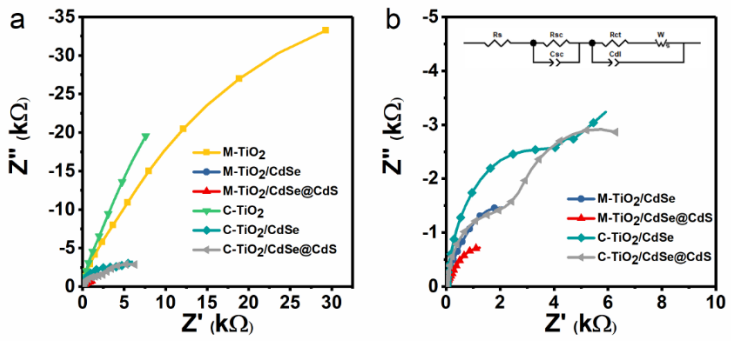

Figure 3.13 (a) EIS Nyquist plots of all samples and (b) The magnified EIS spectra of M-TiO_2/CdSe@CdS, M-TiO_2/CdSe, C-TiO_2/CdSe@CdS, C-TiO_2/CdSe and the inset is the equivalent circuit diagram.

The most interesting feature to understand the improved performance in M-TiO_2 is the R_{CT}. A smaller radius of the semicircle means a lower R_{CT} indicating an improved charge transfer for the best photoanode. As shown in Figure 3.13a, the sample made of bare C-TiO_2 presents the largest R_{CT}, even compared to the bare M-TiO_2. This data gives further indication that the presence of the A/R phase in the M-TiO_2 anode accelerates the charge transfer kinetics and thus reduces the possibility of recombination. This effect is also visible in the dynamic chopped linear sweep voltammetry under light of the two samples (Figure 3.10) in which the bare TiO_2 with the MOF-derived layer exhibits a higher current (0.42 mA/cm^2 vs 0.3 mA/cm^2) compared to the pure anatase film. Furthermore, from Figure 3.13b, the sample M-TiO_2 with CdSe/CdS presents the smallest R_{CT} compared to all the other photoanodes, confirming that the recombination of electron/hole pairs is reduced, due to the presence of the mixed anatase/rutile phase. The R_{CT} of all the samples follow a trend that closely resembles the one observed for the photocurrents. By fitting the data, the R_{CT} values follow M-TiO_2/CdSe@CdS < M-TiO_2/CdSe < C-TiO_2/CdSe@CdS < C-TiO_2/CdSe < M-TiO_2 < C-TiO_2. The values of the R_{CT} are reported in Table 3.4.

Table 3.4 The values of the R_{CT}.

Sample	R_{ct} (kΩ)
C-TiO_2	144.87
M-TiO_2	86.92
C-TiO_2/CdSe	10.29
M-TiO_2/CdSe	3.09
C-TiO_2/CdSe@CdS	3.71
M-TiO_2/CdSe@CdS	2.33

A further confirmation of the suppression of charge recombination in M-TiO_2 can be obtained by analyzing the transient photocurrent by chronoamperometry (Figure 3.14a). In particular, to quantitatively determine

the charge recombination behavior, it is possible to introduce a normalized parameter (D), defined as Eq 3.8[214, 215]:

$$D = \frac{I(t) - I_{in}}{I_{in} - I_{st}} \quad (3.8)$$

where I(t), I_{st} and I_{in} are the time-dependent, steady-state and initial photocurrent, respectively. By plotting ln (D) vs time, it is possible to obtain the transient time constant (τ), defined as the time when lnD= -1[215]. As visible in Figure 3.14b, M-TiO_2 sample presents a slower kinetics, and in particular $\tau_{M\text{-}TiO2} > \tau_{C\text{-}TiO2}$ (0.33 s vs 0.14 s), indicating a reduced charge recombination of the carrier. Overall, these results confirm the faster charge transfer and lower charge-recombination at the M-TiO_2 interface, which could be induced by the band alignment formed by the presence of the mixed anatase/rutile phase.

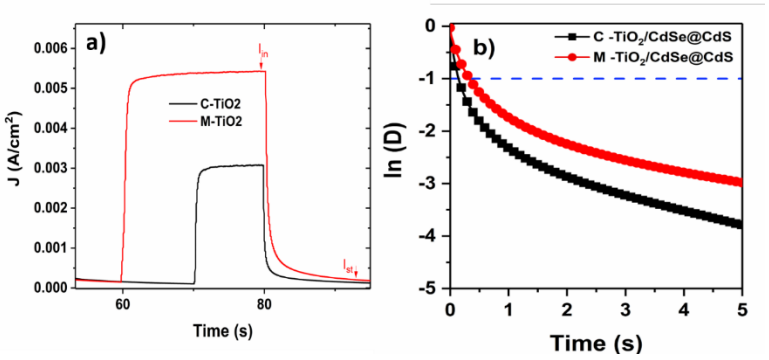

Figure 3.14 (a) Transient photocurrent by chronoamperometry (b) Normalized plot of the current-time dependence for transients.

H_2 evolution was further measured during the PEC measurement for M-TiO_2/CdSe@CdS. The produced H_2 gas was detected using a GC equipped with a thermal conductivity detector. Argon gas was used as the carrier gas for GC analysis. The evolution of H_2 exhibits a nearly linear increase over time (Figure 3.15). The associated Faradaic efficiency ($\eta_{Faradaic}$), which was 75.29% (see below), was determined by comparing the amount of gas produced experimentally with the theoretically calculated values (for details, see the experimental section in the Chapter 2). The difference between the measured and calculated value of H_2 might be due to gas leakage in our home-made prototype experimental system. According to gas chromatography after 3600 s, the H_2 gas evolved was 0.7853 10^{-4} mol, whereas the current obtained by chronoamperometry is 5.593 mA.

$$n_{H_2}(\text{theoretical}) = \frac{0.005593\ (A)\ \times\ 3600\ (s)}{2\ \times\ 96485.33\ C \cdot mol^{-1}} = \ 1.043\ \times\ 10^{-4}\ mol$$

Therefore,

$$\eta_{Faradaic} = \frac{0.7853 \times 10^{-4}\, mol}{1.043 \times 10^{-4}\, mol} = 75.29\%$$

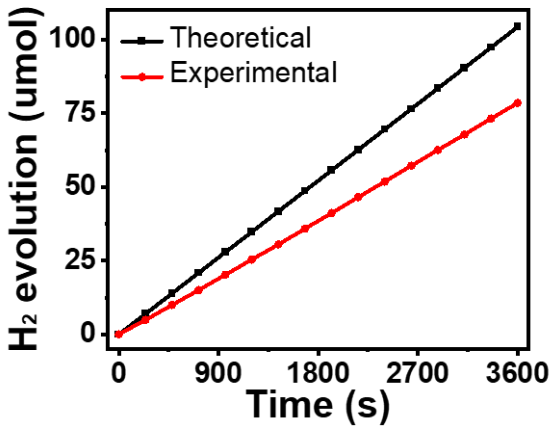

Figure 3.15 H_2 evolution of M-TiO_2/CdSe@CdS as a function of time at 0.9 V vs RHE under 100 mW/cm^2 illumination with AM 1.5 G filter. The evolution of H_2 exhibits a nearly linear increase over time (solid red curve). H_2 evolution is also calculated from the measured current (solid black curve).

3.3 Conclusions and perspectives

In this study, we reported a synthesis method in which MIL-125-NH_2 was used as a sacrificial template to fabricate TiO_2 nanoparticles composed of mixed rutile and anatase phases. To enhance solar absorption in the visible and near-infrared range, this MOF-derived TiO_2 was sensitized with QDs. Structural investigations confirmed that the mixed-phase TiO_2 retained the MOF octahedral morphology. Compared with pure anatase commercial TiO_2, the M-TiO_2 sensitized with core-shell QDs showed an enhanced current density of 47.6%. In addition, this architecture showed a remarkable PEC stability, with a relative increment of 42.1% in the optimized devices compare to the pure anatase TiO_2, maintaining more than 78.7% of the initial value. Transient PL spectra evidenced that this M-TiO_2 film exhibits a faster electron transfer rate than C-TiO_2, which could be ascribed to favorable electronic band alignment and increased charge transfer. UPS spectra and EIS data confirmed the hypothesis of an improved charge separation due to a favorable band alignment of the A/R MOF-derived TiO_2.

In this study, we highlight the potential of using MOF as templates to control the morphology and crystalline phase of TiO_2 films for PEC hydrogen production. These findings provide fundamental insights into the significance of band alignment control in metal oxide semiconductors. PEC cells based on colloidal QDs may focus on controlling the separation of photogenerated charges by introducing a phase junction in a polymorph semiconductor, such as TiO_2, in order to improve their performance and stability.

4 HOLLOW NICKEL OXIDE/CARBON PHOTOCATHODE

This chapter is based on the paper "*Design of MOF-Derived NiO/carbon Nanohybrids Photocathodes Sensitized with Quantum Dots for Solar Hydrogen Production*" published on *Small*, (2022) 2201815.

Link between articles:

As aforementioned in 2.1, a conventional PEC system is composed of at least one photoactive semiconductor electrode, either n-type or p-type, as the working electrode. When the photoactive semiconductor is p-type, the photoelectrode will work as a photocathode. Normally, photoanodes suffer significant photo-corrosion due to their self-photo-oxidation at the photoelectrode/electrolyte interface by the photo-excited holes, and scavengers, such as S^{2-} and SO_3^{2-}, are required to prevent this photo-corrosion. Unlikely, photocathodes based on p-type semiconductors are reported to be cathodically protected from this photooxidation, making them likely to be more stable than the photoanodes[216, 217].

However, in the development of PEC over the past 40 years, there exists a tendency that researchers always pay their attention to the exploitation of photoanodes, such as TiO_2, while often ignoring the development of efficient photocathodes. An analogous phenomenon also exists in the investigation of solar cell, mainly owing to the scarcity of suitable p-type semiconductors[218-220]. The focus on photoanode has made this field fast-developing, while on the opposite, photocathode always develops sluggishly. So, a mismatch between photoanodes and photocathodes in both photocurrent density and catalytic efficiency emerges. The mismatching greatly hinders the construction of high-efficient tandem PEC water-splitting system, in the absence of extra bias between two photoelectrodes[57, 221-224].

Photocathode, usually composed of p-type semiconductors, operates in an inverse mode of a photoanode. To be specific, under light irradiation, the semiconductor absorbs photons with energy equal to or exceeding its bandgap to produce electron and hole pairs. The photoexcited holes will move to the bulk of the p-type semiconductor, while photoexcited electrons transport to the surface of semiconductor, followed by being injected into the electrolyte. This is mainly due to the existence of built-in electric field and band bending. After that, the holes transfer to the counter electrode (e.g., Pt) through the outer circuit and oxidize water to generate O_2 while the electrons are used to reduce proton into molecular H_2, simultaneously. In general, the p-type semiconductors are used as photocathodes so that the minority carriers (electrons) can be directed to the solid/liquid interface for subsequent reduction reactions, especially H_2 generation. Therefore, the CB edge of the photocathode material should be more negative than the water reduction potential level in the NHE scale (see section 1.3.2).

There are four main categories of current photocathode materials so far: metal oxides, silicon, copper-based chalcogenides, and III-V group materials. Among them, p-type silicon, as an attractive photocathode material, shows good electronics mobility (up to 1360 $cm^2 \cdot V^{-1} \cdot s^{-1}$) and wide solar absorption spectrum. However, the critical drawback of it is poor stability in aqueous solution, which limits its water splitting application. One promising solution to this is compositing p-Si with other materials or cocatalysts. The most commonly used III-V group materials are GaP (2.2 eV) and InP (1.34 eV), which are usually existing in the form of nanowire structure to reduce their cost and improve charge collection. The next is copper-based chalcogenides which are another important branch as photocathode materials with favorable visible-light response due to the narrow bandgaps, such as $CuIn_xGa_{1-x}Se_2$ (1.68 eV), $CuGaSe_2$ (1.7 eV), $CuInS_2$ (1.5 eV), and so on[225]. Some of them face the problems of poor stability and structural modification. The last group is p-type MO semiconductor, such as NiO (3.5 eV), Cu_2O (2.0 eV), $CaFe_2O_4$ (1.9 eV), and $CuFeO_2$ (1.5 eV). Most of them often have advantages of easy preparation and low cost[226-228]. However, some of them suffer from low charge-carrier mobility and short charge-carrier lifetime, thus inhibiting their widespread application in PEC systems. Thus, engineering photocathodes with exceptional light absorption ability, high stability, and great conductivity is of great significance.

Based on the above-mentioned situations, the focus of this chapter shifts from the photoanode to the photocathode. NiO, which possesses good thermal/chemical stability and a suitable band edge position at pH 7, was chosen as the photocathode material due to a lack of available materials. [229-231]. However, the NiO-based PEC systems always yield low current density, which can be ascribed to several factors[229, 232-234]:

1) Small hole diffusion coefficient of NiO;
2) Poor electrical conductivity that hinders a rapid charge flow and favours charge recombination;
3) low value of the extinction coefficient that limits the light-harvesting efficiency (LHE);
4) low specific surface area that limits the loading of the sensitizer.

Recently, several strategies have been proposed to overcome these issues, like engineering hollow structure or hybridization of with carbon allotropes[234-236]. However, the synthetic methods are either very complicated and require many reaction steps or cannot satisfy all aspects at the same time.

Templating with MOF is an innovative approach to synthesize NiO that satisfies all the requirements. The NiO derived from Ni-MOF can maintain some of the features of pristine MOF, such as large surface area, composition diversity and dispersion, as well as tailored porosity. Moreover, under suitable thermal treatment, the organic linkers of the Ni-MOF can be decomposed, forming porous carbon allotropes which will hybridize the NiO[147]. Therefore, we reported a facile synthetic strategy to engineer NiO photocathode with a hollow ball-in-ball structure formed by NiO/carbon hybrid using nickel-based MOFs (Ni-MOFs) as

a sacrificial template. Due to the wide bandgap (E_g = 3.6-4.0 eV) of NiO, we employed inorganic semiconductor QDs as the sensitizer to enhance solar absorption in the visible and near-infrared range via SILAR method. After sensitization with QDs, a 2.2-fold PEC performance enhancement over pure NiO/QDs film is obtained. Remarkably, this value is obtained at neutral pH (6.8) and without any sacrificial reagent, cocatalyst, or molecular linker. Such improvement can be ascribed to a higher surface area, improved light scattering, and to the presence of carbon that facilitates charge transfer.

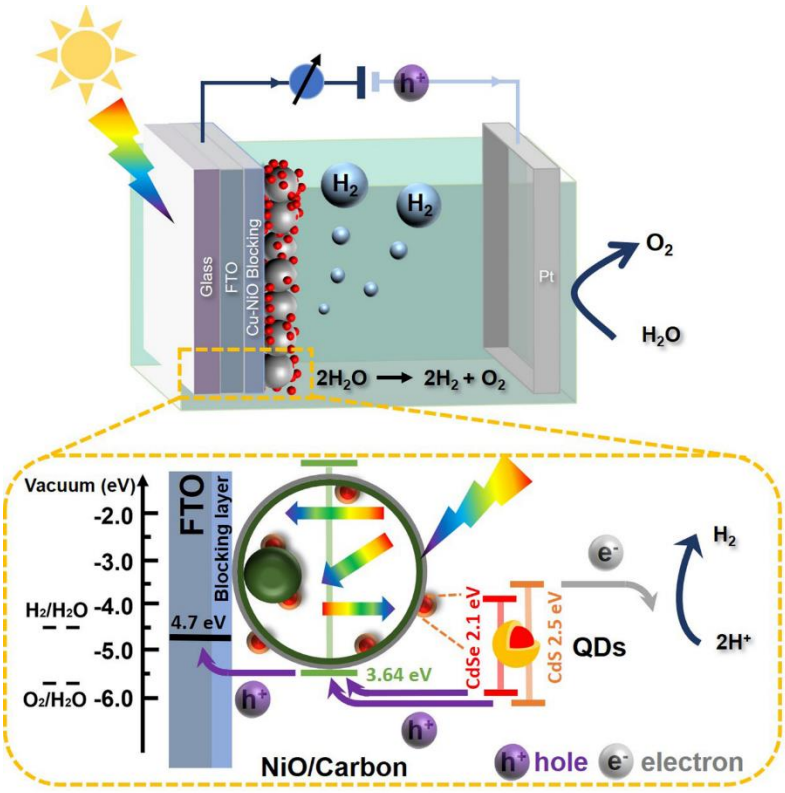

Figure 4.1 Schematic illustration of the assembled NiO/C photocathode in a PEC setup and the migration of photogenerated excitons at the interfaces.

4.1 Experimental sections

In the section 2.3, we reported the detail of the synthesis. There are few unique properties of hollow structures that are beneficial for promoting the PEC performance of semiconductor materials in water splitting application (Figure 4.2)[236]. Specifically, the large specific surface areas will allow more sensitizers loading which can provide abundant active sites for redox reactions[237, 238]. Besides, the thin-shelled topologies reduce the charge transport distance. Also, light scattering and reflection effects induced by hollow structures can enhance the absorption and utilization of solar irradiation[239]. The fast mass transfer in open hollow structures could further accelerate the reactions. Therefore, in this experiment, we would like to design a hollow structure photocathode to enhance the NiO photocathode PEC performance.

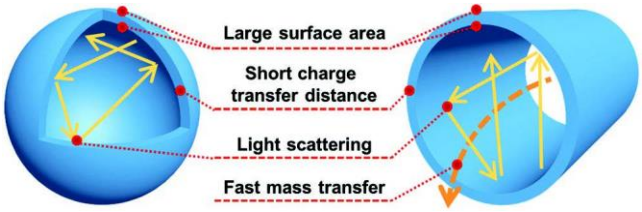

Figure 4.2 Schematic illustration of some advantages of closed and open hollow structures for photocatalytic reactions. Reprinted with permission[236]. Copyright 2019, Wiley.

Before using the trimesic acid as the organic ligand, we tried NH_2-BDC at the beginning. From Figure 4.3, we can see that the synthesized Ni-MOF exhibits a well-defined nanorod morphology with a smooth surface and average length around 5-7 μm. We also employed a two-step heat treatment to convert this MOF to NiO/carbon composite (refer to 2.3 for annealing details).

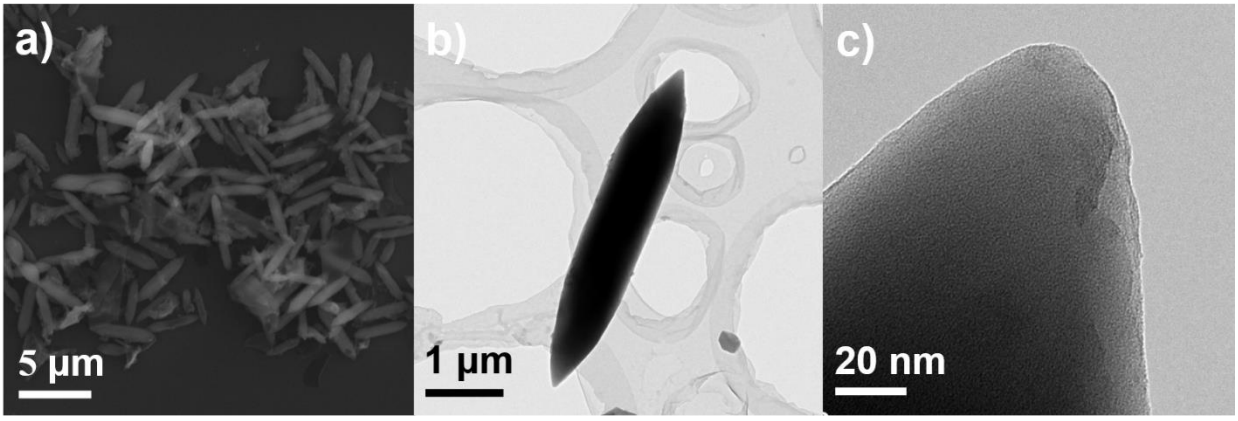

Figure 4.3 TEM images of the Ni-MOF precursors with ligand NH_2-BDC (a and b), HRTEM (c).

After annealing, the morphologies of NiO/C products were characterized by SEM and TEM. As shown in Figure 4.4, after two-step calcination, the surface became rough and some nanorods bended. However, most of resulting NiO/C composite inherited the morphology of the Ni-MOF, but did not reveal a hierarchical hollow structure (Figure 4.4a) as visible by the difference in contrast in the TEM image (Figure 4.4b). The elemental mapping images (Figure 4.4d-g) of NiO/C obtained in STEM mode indicated relatively uniform distributions of nickel, oxygen, and carbon.

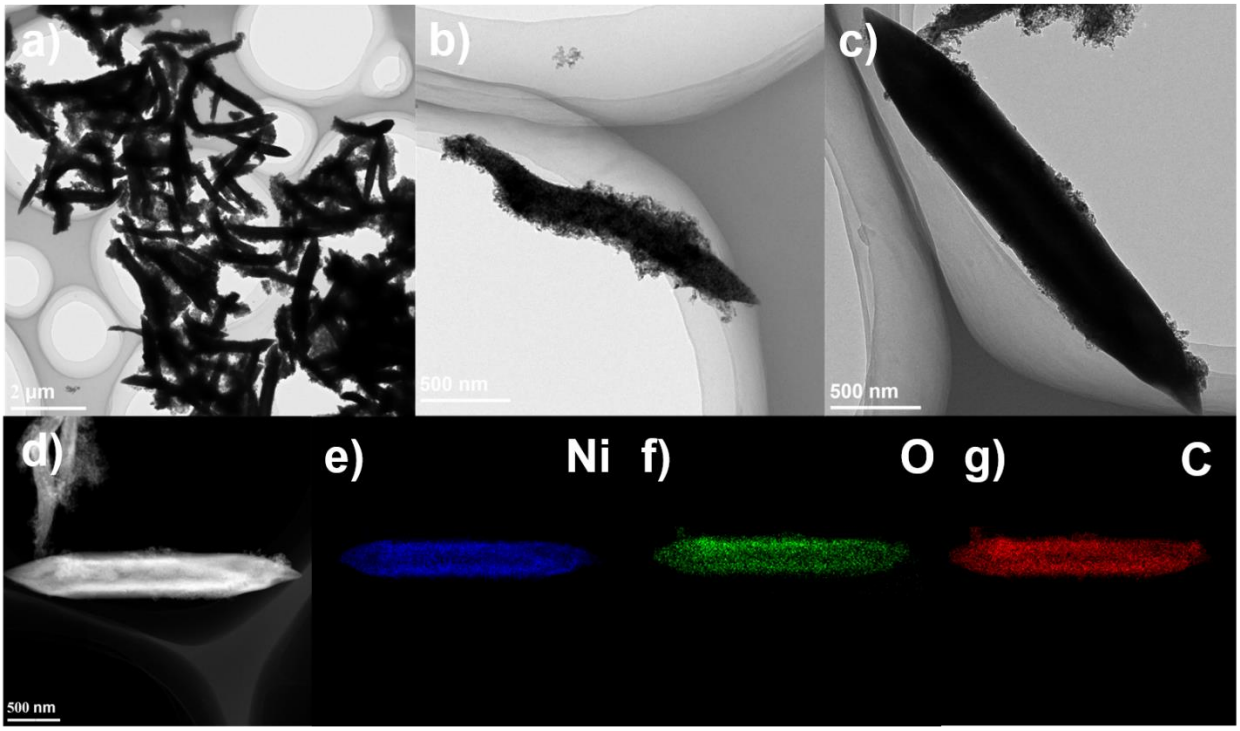

Figure 4.4 TEM images of the NiO/C (a, b, and c); (d-g): STEM image, nickel, oxygen, and carbon.

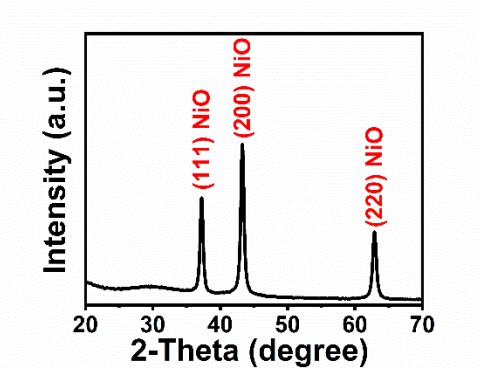

Figure 4.5 XRD patterns of NiO/C.

The XRD data (Figure 4.5) acquired from the sample NiO/C shows that the diffraction peaks around 37.17°, 43.29° and 62.87° can be indexed to the (111), (200), and (220) of NiO in good agreement with the standard face-centered cubic (fcc) NiO phase (JCPDS No. 47-1049) and consistent with data from Figure 4.9. No other redundant peaks are detected, suggesting a complete thermal conversion of precursor.

Then, we turned to the ligand of H_3BTC as the second ligand to build a hollow structure, which needs polyvinylpyrrolidone (PVP) as the stabilizing agent. It is found that PVP plays an important role in the morphology of the Ni-MOF precursor. As an amphiphilic surfactant, PVP can facilitate the dispersion of various nanocrystals in water or organic solvents[240-242]. Furthermore, its pyrrolidone groups can coordinate with metal ions[243]. During the hydrothermal process, the Ni ions coordinate with the pyrrolidone groups of PVP so that they can distribute homogeneously along the PVP chains. In addition, PVP also serves as a stabilizing agent and a source of carbon.

We also encountered some issues in the fabrication of the films. Initially we used the standard doctor-blade method. However, 2 layers of NiO/C film with QDs sensitizers exhibited a very low current density, around -13 $\mu A/cm^2$ at 0 V vs. RHE, and very bad light response. We believe this is due to the thickness of the film (~ 15 μm) which is too thick to transfer efficiently the photo-electron to the counter electrode. We tried diluting the paste concentration to make the film thinner with the doctor blade technique, but it did not work and it was not possible to form a uniform layer. Finally, we selected the EPD method instead of doctor-blade method, which will allow us to deposit the MO on the FTO glass. The thickness of the film could be adjusted via EPD time and the concentration of iodine in the solution. Briefly speaking, the iodine reacts with acetone and generates protons, which can absorb onto the surface of suspended particles to enhance the EPD process and decrease the voltage required[244]. In this way, we reduced the thickness to ~7 μm. In addition, colloidal QDs have difficulty penetrating films even during the EPD method, so SILAR may be a better option for depositing multilayers of QDs.

4.2 Results and discussions

4.2.1 Synthesis and structural characterizations

Figure 4.6 illustrates the synthesis procedure used to obtain hierarchical NiO/carbon nanocomposites. Ni-MOFs was first synthesized by a conventional solvothermal approach[147]. To convert Ni-MOF microspheres into hierarchical NiO/carbon (NiO/C) nanocomposites, a two-step heat treatment was performed. In the first step, carbon-coated nickel nanoparticles are formed by annealing the Ni-MOF precursor under an inert gas environment (Ar). During this stage, Ni ions in the MOFs are converted into metallic Ni nanoparticles, while organic ligands are carbonized on the surface of the MOFs. Subsequently, the Ni/carbon (Ni/C) nanocomposites are annealed in air, and the metallic Ni nanoparticles are partially oxidized to form NiO. The final NiO/C nanocomposites retain the original microspherical structure of the Ni-MOFs.

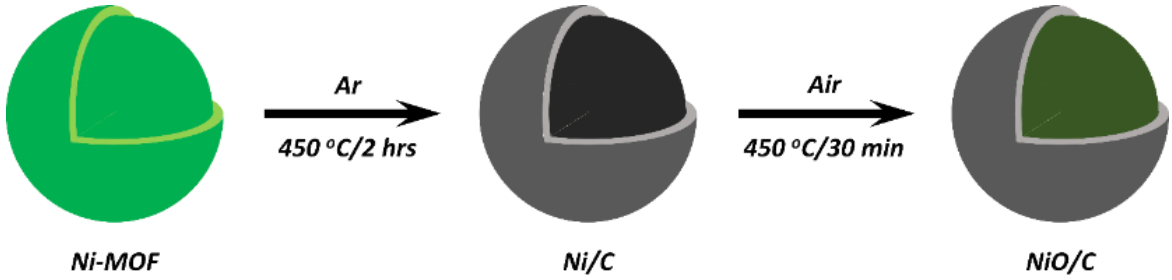

Figure 4.6 Schematic illustration of the formation of NiO/C composites.

The morphologies of Ni-MOF, Ni/C and NiO/C products were characterized by scanning electron microscopy (SEM) and transmission electron microscopy (TEM). As shown in Figure 4.7a and Figure 4.7a, Ni-MOF displays a spherical morphology with a smooth surface with average diameters around 1-2 μm. After the first step of calcination in an inert atmosphere, the surface became rough after pyrolysis, but no changes in morphology were detected (Figure 4.7c and Figure 4.8b). In the second step, annealing is conducted in air to oxidize metallic nickel. The resulting NiO/C composite inherits the morphology of the Ni-MOF and reveals a hierarchical hollow structure (Figure 4.8c) as visible by the difference in contrast in the TEM image (Figure 4.8c).

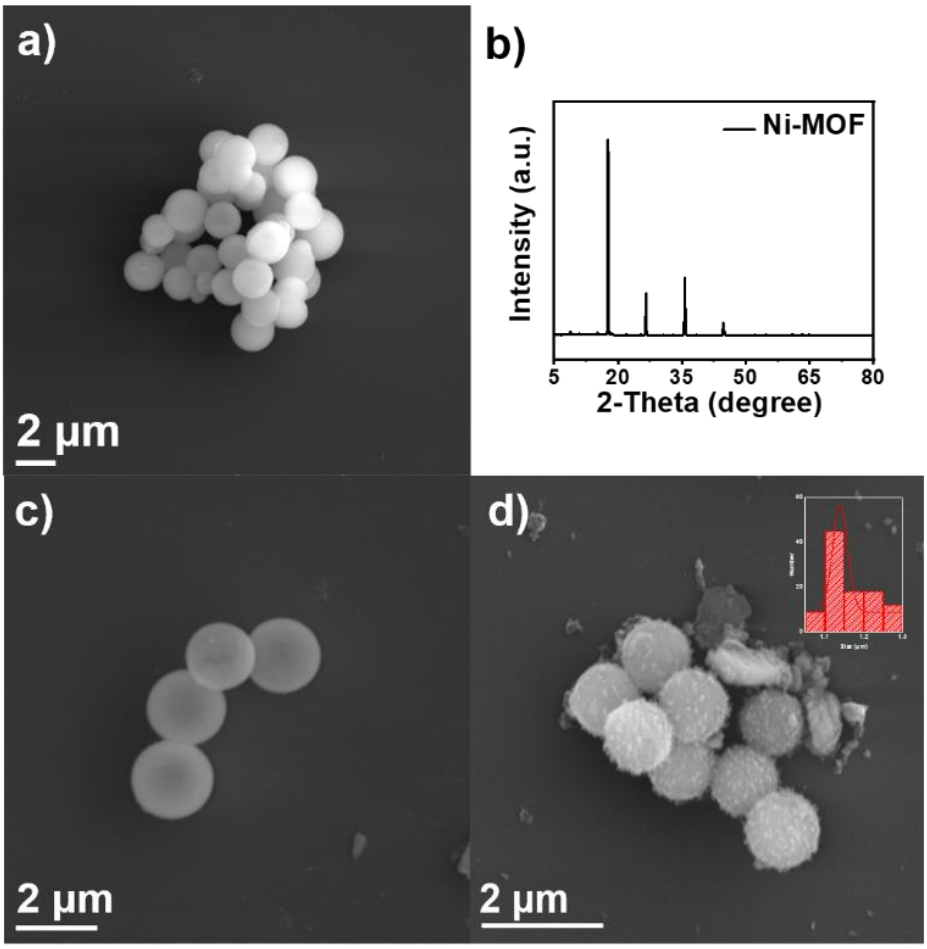

Figure 4.7 SEM images of the Ni-MOF precursors (a), XRD patterns of Ni-MOF precursors (b), SEM of Ni/C (c), and NiO/C, the inset image exhibits the average size of NiO/C (d).

However, when compared to the original Ni-MOF (the Figure 4.7a with Figure 4.7d), the NiO/C has been shrunk and truncated, mainly due to the loss of C and H of organic ligands after thermolysis[116]. Selected-area electron diffraction (SAED) (Figure 4.8d) shows a group of diffraction rings that are indexed to the (111), (200), and (220) of NiO. From the high-resolution TEM (HRTEM) image (Figure 4.8e), the d-spacings are 2.4 Å and 2.1 Å and can be indexed to the NiO (111) and (200) planes. Energy-dispersive X-ray spectroscopy (EDS) analysis (Figure 4.10a and b) confirms the presence of Ni, O, and C elements in the Ni/C and NiO/C composite. The elemental mapping images (Figure 4.8f) of NiO/C obtained in STEM mode indicate relatively uniform distributions of nickel (43%), and oxygen (41.1%), while carbon (15.9%) element seems more concentrated in the outer shell of the hollow structure. The content of C is much higher than the result from TGA is due to the contaminant from environment.

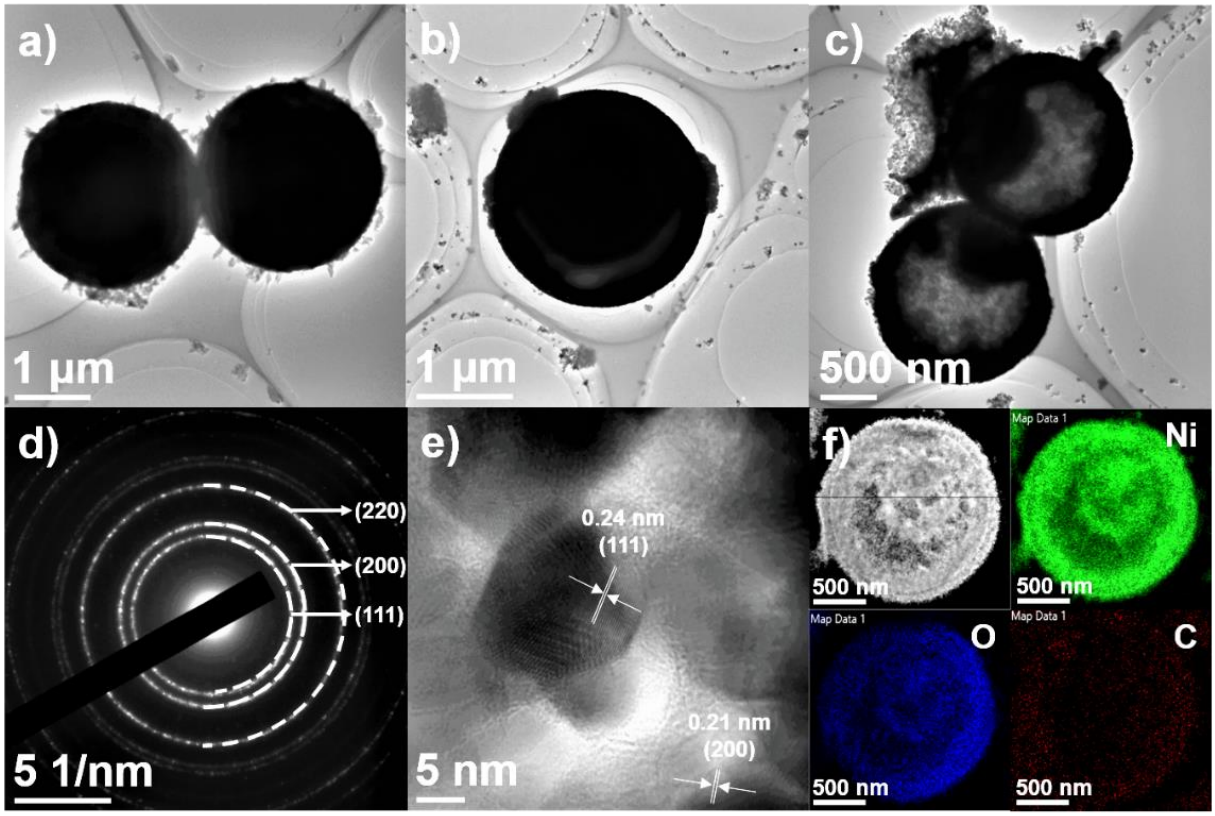

Figure 4.8 TEM images of the Ni-MOF precursors (a), Ni/C (b), and NiO/C (c). (d) SAED pattern of NiO/C. (e) HRTEM image of NiO/C. Elemental mapping images of NiO/C (f): STEM image, nickel, oxygen, and carbon.

Based on the above results, the formation of the hollow ball-in-ball structure of NiO/C can be due to the heterogeneous decomposition and contraction process of Ni-MOFs induced by nonequilibrium heat conduction. At the beginning of the annealing process, there is a large temperature gradient along the radial direction from the exterior shell to the interior core. The surface of Ni-MOF starts to decompose, forming an outer shell. With prolonged thermal treatment, the internal core starts to decompose as well. At this stage, there will be two opposite forces present. One is the outward force caused by the bond between the NiO shell and the Ni-MOF core and the release of gases in the NiO-MOFs decomposition process Another is the inward force caused by the decomposition and contraction of the Ni-MOF core. The layers of the shell and core form and separate under these two forces, forming a unique nanostructure of ball-in-ball microspheres[131, 245].

X-ray diffraction (XRD) patterns were acquired from the Ni-MOF precursors, Ni/C obtained by calcining Ni-MOFs at 450 °C in Ar, and on NiO/C synthesized by annealing Ni/carbon at 450 °C in air (Figure 4.9 and 4.7a). The XRD data acquired from Ni-MOF shows that it is highly crystalline, and all diffraction peaks can be well assigned to the $Ni_3(BTC)_2 \cdot 12H_2O$. Moreover, it is also in good agreement with previous

reports[147, 246, 247]. All the characteristic diffraction peaks of Ni/C around 44.41° and 51.91° correspond to the (111) and (200) planes of cubic nickel (fcc) (JCPDS No. 04-0850) (Figure. 4.9a). For the sample NiO/C, the diffraction peaks around 37.17°, 43.29° and 62.87° can be indexed to the (111), (200), and (220) of NiO, consistent with HRTEM and SAED data, and in good agreement with the standard face-centered cubic (fcc) NiO phase (JCPDS No. 47-1049) (Figure 4.9b)[248]. No other redundant peaks are detected, suggesting a complete thermal conversion from metallic Ni to NiO in air.

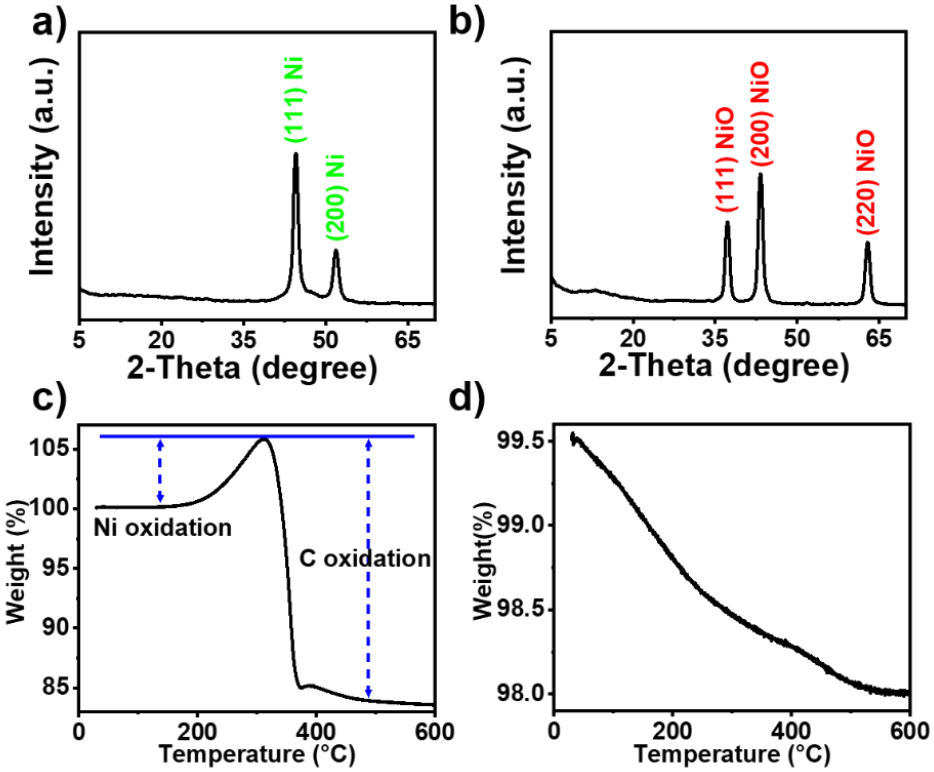

Figure 4.9 XRD patterns of (a) Ni/C and (b) NiO/C. TGA results of (c) Ni/C composite and (d) NiO/C.

The calcination process of Ni/C and NiO/C was also investigated by thermogravimetric analysis (TGA) (Figure 4.9c and d). The weight of the Ni/C first increases and then decreases with rising temperature. This is an indication that Ni is first oxidized, while the carbon is still stable up to 310 °C. The loss of weight in the second stage, after 400 °C, occurs because of the carbon oxidation, further confirming its presence (around 15 wt%). TGA can also estimate the final carbon content of NiO/C; in our samples it has been found to be around 2 wt%. (Figure 4.9d). Figure 4.10c displays Raman analysis performed on representative samples. The characteristic peaks of carbon around 1136 and 1387 cm^{-1} are clearly visible in the Ni/C and NiO/C samples. The lower intensity of the peaks in NiO/C suggests a lower amount of carbon in the sample. This data is also confirmed by the TGA analysis reported in Figure 4.9c and d. Instead, in the NiO sample,

these peaks are almost completely absent, suggesting that there is almost no carbon left. The small amount detected is not significant enough to influence the performance of the photocathode.

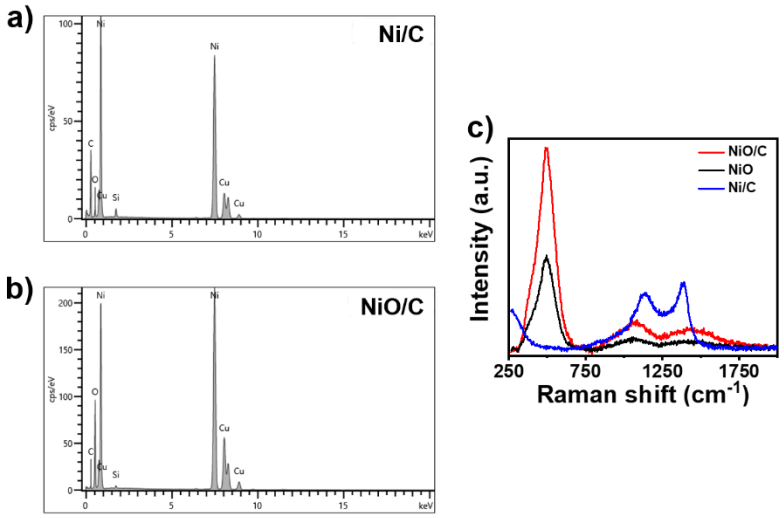

Figure 4.10 EDS analysis of (a) Ni/C, (b) NiO/C samples, and (c) Raman spectra of pure-NiO, Ni/C, and NiO/C.

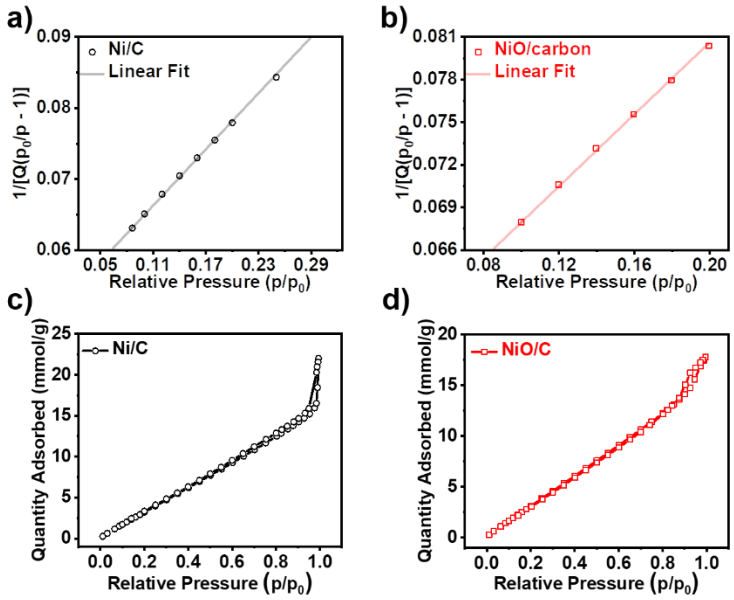

Figure 4.11 BET surface area plot of (a) Ni/C and (b) NiO/C; Nitrogen adsorption-desorption isotherm of the (c) Ni/C and (d) NiO/C nanocomposite.

The Brunauer-Emmett-Teller (BET) surface areas of Ni/C and NiO/C are 531.2 ± 4.3 m^2/g and 535.7 ± 5.7 m^2/g, respectively (Figure 4.11). These values indicate a large surface area that can be in contact with the electrolyte and allow a large loading of QDs sensitizers. As shown in Figure 4.11c and d, when uptake over

at a range of high P/P_0 (0.8-1), the nitrogen adsorption-desorption isotherm exhibits a typical IV-type curve with hysteresis loop, revealing a mesoporous structure[249].

To investigate the surface electronic properties, the surface chemical states of the Ni/C and NiO/C were probed by X-ray photoelectron spectroscopy (XPS) (Figure 4.12). As expected, for both Ni/C and NiO/C the survey XPS spectra reveal the presence of Ni, O and C peaks (Figure 4.12a and b) without other elements in the composite, consistent with the EDX and XRD results. The high-resolution O 1s spectrum of the Ni/C (Figure 4.12c) can be fitted with a single peak at a binding energy of 532.6 eV, which can be assigned to the oxygen in hydroxide[250]. This is largely due to the prolonged exposure of the sample to an ambient environment. Instead, in the O 1s spectrum of NiO/C there are two peaks, at 529.7 eV and 532.9 (Figure 4.12d). The lower binding energy peak at 529.7 eV is attributed to the O (1s) core level of O^{2-} anions associated with Ni-O chemical bonding[251, 252], while the higher binding energy peak observed at 532.9 eV can be attributed to the presence of carbon and/or of hydroxyl (-OH) groups[253]. The high-resolution Ni 2p spectra for Ni/C and NiO/C are shown in Figure 4.8e and f. For the Ni/C composite (Figure 4.12e), besides the shake-up satellite peaks, the peak at approximate 852.6 eV ($2p_{3/2}$) and 869.8 eV ($2p_{1/2}$) can be assigned to metallic Ni. Additionally, the binding energy difference (ΔE) between Ni ($2p_{3/2}$) and Ni ($2p_{1/2}$) peaks is 17.2 eV, confirming the metallic nature of Ni. As shown in Figure. 4.12f, the Ni 2p region of NiO/C comprises five features: Ni $2p_{3/2}$ (854.2 eV) main peak and its satellites (861.6 eV), Ni 2p1/2 (872.9 eV) main peak and its satellite (874.2 eV), all of which can be attributed to the presence of NiO[252-254]. Apart from these peaks, an additional feature peak appeared at 856.2 eV as a small shoulder, which was presumably due to the presence of a small quantity of Ni_2O_3 on the surface[254]. The value of the binding energy difference between Ni ($2p_{3/2}$) and Ni ($2p_{1/2}$) peaks is about 18.7 eV, significantly larger than that of 17.2 eV for metallic Ni[255, 256]. This confirms that the Ni is in it oxidize forms (i.e. Ni^{2+}) and no pure metallic form was detected.

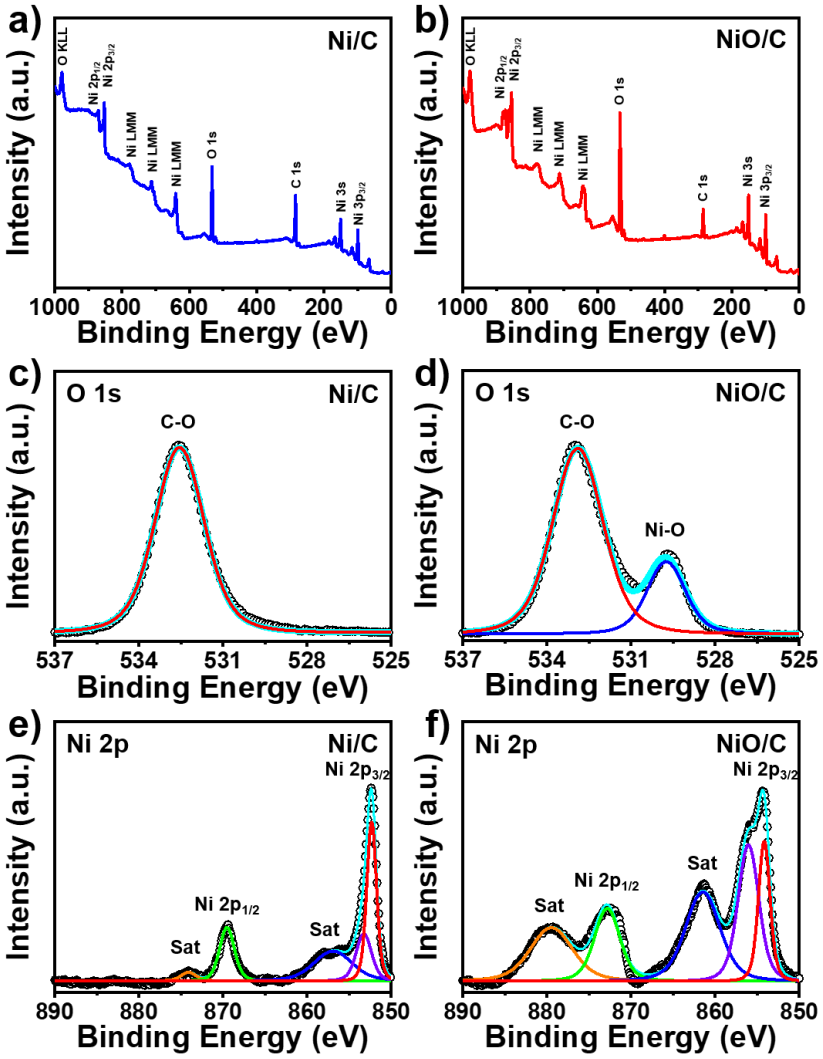

Figure 4.12 XPS survey spectra of (a) Ni/C and (b) NiO/C. High resolution O 1s spectra for (c) Ni/C and (d) NiO/C. High resolution Ni 2p spectra for (e) Ni/C and (f) NiO/C.

4.2.2 Optical properties

Besides its use as mesoporous layer for p-type DSSCs, NiO has also been used as hole transporting/electron blocking layer in perovskite solar cells, due to its inertness and intrinsically p-type conductivity with a deep valence band (5.1-5.4 eV)[257]. These characteristics are beneficial for both efficient hole extraction and device stability. In our work a back-illuminated configuration is used, thus more holes are photogenerated at the back contact and be exposed to recombination centers. For this reason, in order to reduce the charge recombination at the back contact, a blocking layer of Cu-doped NiO was used as interlayer between the FTO and the NiO or NiO/C films[149-151].

The UV-DRS of pure NiO with and without the Cu-doped NiO blocking layer are shown in Figure 4.13a. Both of them present absorption in the UV-visible region, typical of NiO, with almost identical profiles, meaning that the Cu-doped NiO blocking layer has a very slight influence on the NiO films light absorption. Besides, the NiO/C also has a better light absorption than the pure NiO from MOF, which is due to better light scattering inside the carbon. In Figure 4.13a is also reported the absorption spectrum of NiO/C after sensitization with QDs (CdSe or CdSe@CdS). The spectrum presents a characteristic feature of the first excitonic absorption peak located at 546 nm and 573 nm corresponding to the CdSe and CdSe@CdS QDs, respectively. The successful deposition of QDs on the NiO/C films after SILAR process is also confirmed by TEM (Figure 4.13b). No obvious QD aggregation is visible on the surface of NiO/C. To evaluate whether the NiO/C could serve as an effective photocathode, Open circuit potential (OCP) test was performed under dark and illuminated conditions as shown in Figure 4.13c. Upon illumination, the OCP shifted toward a more positive potential, indicating that holes generated from QDs can transfer to NiO/C in the assembled photocathode.

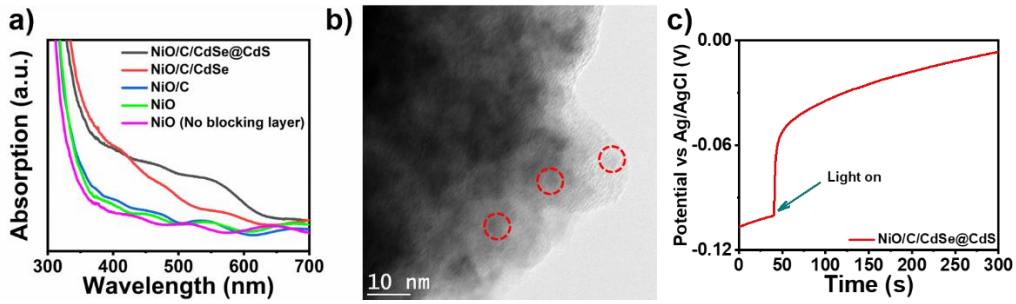

Figure 4.13 (a) DRS-UV spectra of pure NiO without blocking layer, NiO with blocking layer, NiO/C with blocking layer, and NiO/C with blocking layer sensitized by CdSe and CdSe@CdS; (b) TEM images of QDs (CdSe@CdS) deposited by SILAR method on NiO/C; (c) Open circuit potential response of the CdSe@CdS QDs/NiO/C photocathode under dark and illuminated conditions (under AM 1.5 G illumination (100 mW/cm^2).

The cross-section and plain-view SEM imaging and corresponding EDS analysis of the CdSe@CdS sensitized NiO/C photocathodes are shown in Figure 4.14. The thickness of the NiO/C film is estimated to be ~7.6 μm. The CdSe@CdS QDs were found to be uniformly dispersed in the NiO/C film. The EDS mapping spectra verified the presence of Ni, O, C, Cd, Se, and S, respectively, consistent with the chemical composition in the CdSe@CdS QD-sensitized NiO/C photocathode.

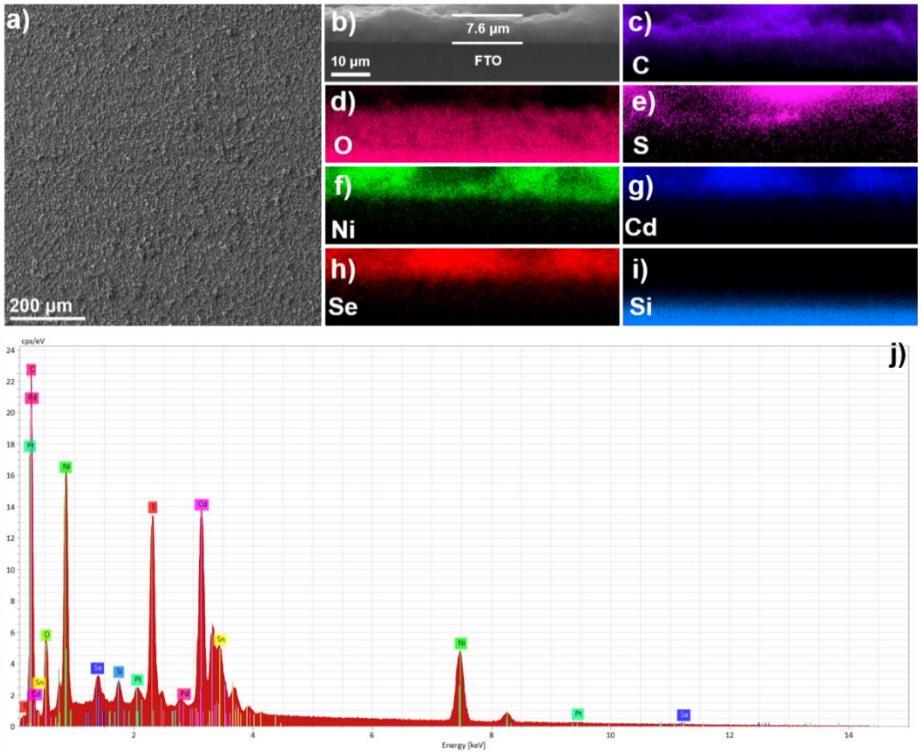

Figure 4.14 Plain-view and cross-sectional SEM image of CdSe@CdS QDs sensitized photocathode (a and b); EDS mapping analysis of all the elements in relevant NiO/C/CdSe@CdS electrode including (c) C, (d) O, (e) S, (f) Ni, (g) Cd, (h) Se and (i) Si; j) EDS spectra of all chemical composition.

4.2.3 PEC measurements

The QDs-sensitized NiO/C photoelectrodes are tested in a typical three-electrode configuration with a Pt counter electrode and an Ag/AgCl reference electrode (saturated with 3M KCl). N_2-purged 0.1 M Na_2SO_4 aqueous solution (pH ~ 6.8) was used as electrolyte. The PEC activity of the different photocathodes is reported in Figure 4.15. All the photocurrents were measured under dark, continuous and chopped illumination. Light-chopped linear sweep voltammetry (LSV) measurements on the different photocathodes are reported in Figure 4.16.

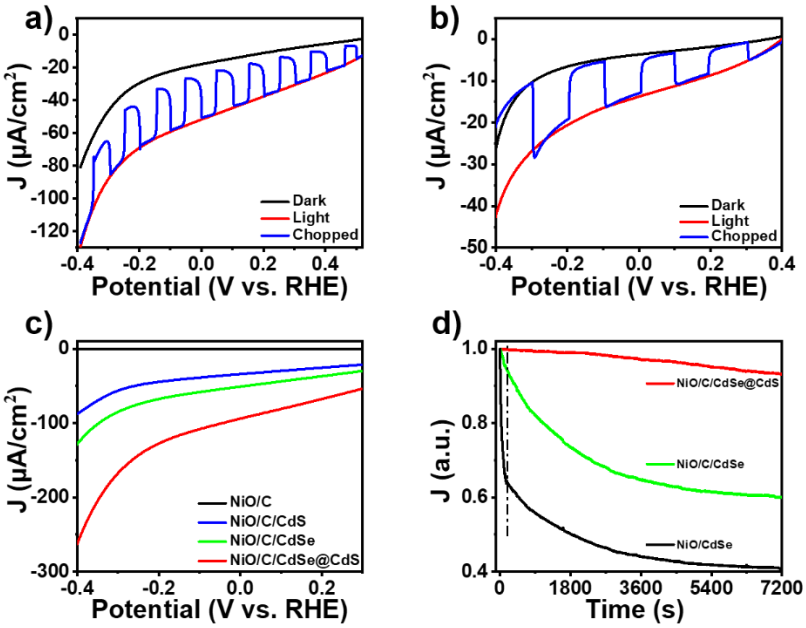

Figure 4.15 PEC performance under dark, continuous and chopped illumination. (a) NiO/C/CdSe; (b) NiO/CdSe; (c) LSV of pure NiO/C and NiO/C sensitized by CdS, CdSe, and CdSe@CdS QDs; (d) Stability measurements (chronoamperometry) of NiO/C sensitized by CdSe and CdSe@CdS photoanodes at 0 V versus RHE under AM 1.5 G illumination (100 mW/cm^2).

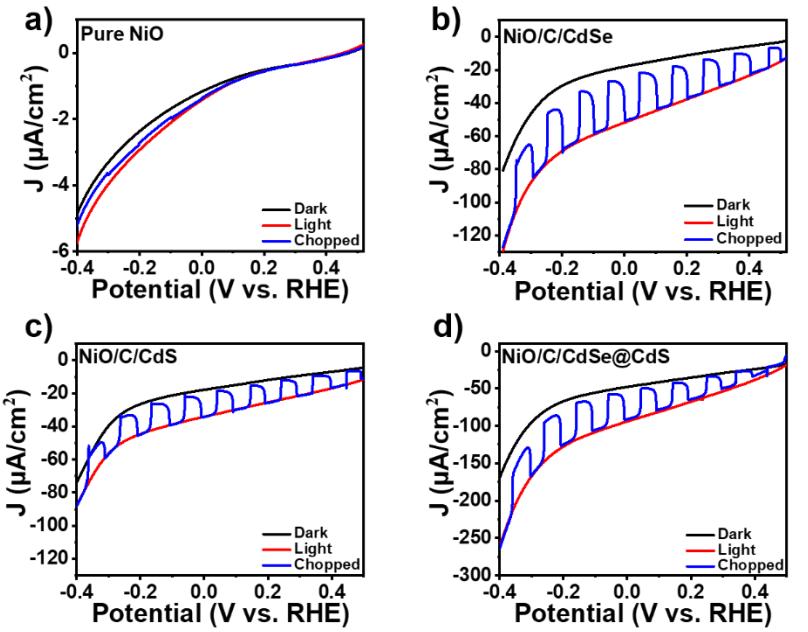

Figure 4.16 LSV under dark, continuous and chopped illumination. (a) Pure NiO; (b) NiO/C/CdSe; (c) NiO/C/CdS and (d) NiO/C/CdSe@CdS.

Notably, the photocurrent density (J_{ph}) of NiO/C/CdSe photocathode with blocking layer is as high as -51.87 μA/cm^2 at 0 V vs. RHE (Figure 4.15a). The instant response of the photocurrent to the chopped illumination indicates an efficient separation of electron–hole pairs in the system induced by visible light. The NiO/C/CdSe photocathode without blocking layer displayed similar maximum J_{ph} (-53.82 μA/cm^2 at 0 V vs. RHE) but with a slower dynamic (Figure 4.17). The presence of the blocking layer can reduce the accumulation of charges at the interfaces and thus allow a faster transient response.

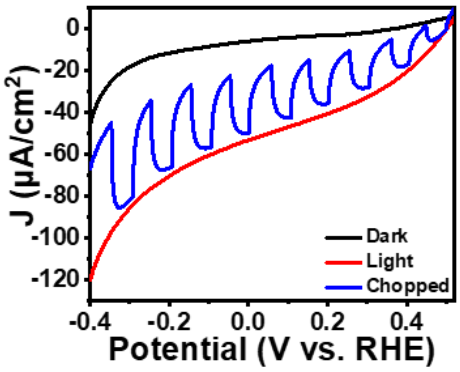

Figure 4.17 Photocurrent density potential dependence of NiO/C/CdSe without blocking layers.

To observe the influence of the presence of carbon on the properties of the photocathode, the same experiments were also carried out using as benchmark a pure NiO film-based photocathode prepared using a similar MOF templated technique. The contribution of pure NiO without any QDs to the electrode's photocurrent is negligible (Figure 4.16a). When the pure NiO film was sensitized with CdSe QDs, the J_{ph} was only -13.97 μA/cm^2 (Figure 4.15b). Thus, the presence of carbon in the NiO shell can improve the charge collection and PEC performance due to an improved conductivity of the film. A similar phenomenon was previously observed for other mesoporous metal oxides electrodes[140, 141, 258]. To further extend the spectral response of the photocathode, core@shell CdSe/CdS QDs were deposited on NiO/C by SILAR method. For a fair comparison, NiO/C/CdS QDs were also prepared. As visible in Figure 4.16c the photocurrent at 0 V vs. RHE from NiO/C/CdSe@CdS (-93.59 μA/cm^2) is clearly superior to those obtained with only CdSe (-51.87 μA/cm^2) or CdS QDs (-27.63 μA/cm^2), reaching a maximum of -285 μA/cm^2 at -0.4 V vs RHE. By employing the core-shell QDs (CdSe@CdS), a +225% maximum enhancement in photocurrent can be obtained compared to core QDs (CdSe).

The main reason for the improved performance of core-shell QDs compared to core QDs is not only the improved absorption range, but also due to the passivation of surface defects offered by the CdS shell that covers the core. Surface defects can in fact act as charge traps, reducing the photoconversion and increasing the charge recombination of core-only QDs[200, 201]. However, the function of the shell is to passivate the

core material from the QDs surface chemistry and the surrounding chemical environment[202]. Thus, core-shell QDs exhibit enhanced photocurrent and stability due to their excellent properties such as reduced surface traps, suppressed charge recombination and enhanced photo/chemical stability[203, 204]. A schematic illustration of the photocathode and the principle of PEC hydrogen generation are shown in Figure 4.1.

Another major unresolved challenge for PEC devices is their long-term stability. In this work, the stability of QDs sensitized NiO photocathodes PEC devices (photocurrent vs. time evolution) was measured at 0 V vs RHE under AM 1.5 G solar illumination (100 mW/cm^2) (Figure 4.15d). To better visualize the decay trends, the photocurrent densities of the photoanodes were normalized to their maximum values. The J_{ph} of the device based on bare NiO sensitized with QDs rapidly decays within 180 s, reducing to about 65% of the initial values, and further decay to around 40% of the initial value after 7200 s. For the NiO/C/CdSe QDs photocathodes, after 2 h the J_{ph} declined to 60.1% of its initial value. On the other hand, the photocurrent values of NiO/C/CdSe@CdS within the first 180 seconds did not decrease, maintaining 99.61%, of their initial value. Even after 2 h of continuous operation, the NiO/C/CdSe@CdS sample remarkably retained more than 93.2% of its initial value. This difference in long-term stability of PEC devices can be attributed to a better passivation due to the presence of the shell of the QDs and to the presence of carbon which facilitate the charge transfer and thus decrease the photodegradation of the QDs[259].

To clarify the working mechanism of the NiO/C/QDs photocathodes and the effect of the presence of a conductive carbon matrix on the band alignment of NiO and NiO/C, we investigated the band energy alignments of the materials by UPS analysis. According to the classical Tauc's formula[210], the energy bandgaps of pure NiO films and NiO/C films were calculated to be ~3.73 eV, and 3.64 eV, respectively (Fig. 4.18c). UPS with He I radiation (21.21 eV) was used to estimate the Fermi level (E_F) and valance band maximum (VBM) energy level. With these data, it is possible to determine the conduction band minimum (CBM) level values of the pure NiO films and NiO/C films (the detailed analysis is reported in Fig. 4.18a and b). The precise band alignment and schematic diagram of QDs-sensitized photoanode for PEC cell are illustrated in Fig. 4.18d and f. Compared to pure NiO, a shift of the VBM and a reduced band gap can be seen for the NiO/C film. These changes can have a positive influence on the charge transfer, favouring the injection of holes from the QDs to the NiO. The presence of carbon will also contribute to promote charge separation and suppresses charge recombination between NiO nanoparticles. As a consequence, the photocathode will present an improved efficiency and stability because the oxidation of the QDs is reduced by removing the generated holes and electrons more rapidly.

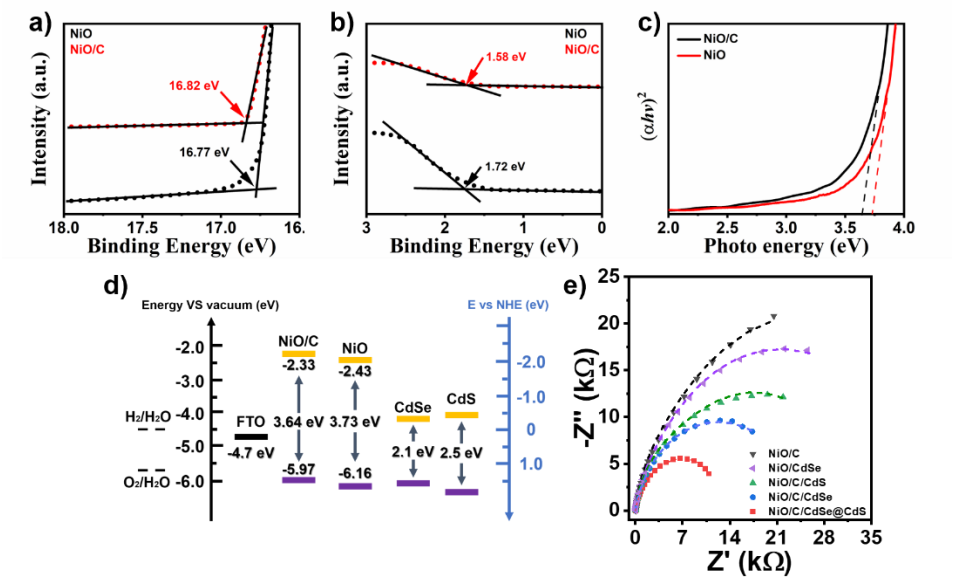

Figure 4.18 High binding energy cut-off (a) and low binding energy cut-off (b) of UPS spectra of NiO films and NiO/C films; The extrapolation of Tauc plots ($(\alpha h\nu)^2$ versus photon energy ($h\nu$)) for the NiO films and NiO/C films (c). (d) Summary of the energy levels obtained from UPS measurements. The CdSe and CdS energy levels are taken from[182]; (e) Nyquist plots of all samples recorded at 0 V versus RHE under 1 Sun (100 mW/cm^2).

To further investigate the mechanism responsible for the different performances of NiO photocathodes, the charge transfer characteristics of the photoelectrodes were investigated using electrochemical impedance spectroscopy (EIS). Figures 6c shows the Nyquist plots recorded at 0 V versus RHE under 1 Sun (100 mW/cm^2) of representative samples of NiO, with/without carbon and QDs. The data were fitted with a Randles equivalent circuit consisting of a series resistance (R_S), space charge capacitance and resistance (C_{SC} and R_{SC}), double layer capacitance (C_{DL}) and charge transfer resistance (R_{CT}) and a Warburg element (W). Similar models have been already developed for related systems[117, 211]. By extrapolating the R_{CT} for each device (Table 4.1), it is possible to confirm that the presence of carbon is beneficial for charge transfer: the R_{CT} of NiO/CdSe w/o carbon is two times higher compared to the NiO/C/CdSe sample. Also, compared to the single CdSe and CdS QDs, the use of core/shell QDs further reduced the R_{CT} thanks to a more favorable band alignment that allow faster charge transfer[153].

Table 4.1 The values of the R_{CT}.

Sample	R_{ct} (kΩ)
NiO/C	38.46
NiO/CdSe	24.73
NiO/C/CdSe	17.71
NiO/C/CdSe@CdS	13.38

To confirm that the photocurrent generated by the photocathode was related to H_2 production and not to other photoreduction processes, we measured the H_2 evolution for NiO/C/CdSe@CdS photocathode sample during the PEC measurement at -0.4 V vs RHE under 1 sun. A gas chromatograph (GC) equipped with a thermal conductivity detector was employed go detect the produced H_2 gas. Argon gas was used as the carrier gas for GC analysis. The evolution of H_2 exhibits a nearly linear increase over time (Figure. 4.19). The theoretical curve is calculated based on the actual photocurrent versus time. The associated Faradaic efficiency ($\eta_{Faradaic}$) of 95.5%, was determined by comparing the amount of gas produced experimentally with the theoretically calculated values (Detailed calculations are provided in the Supplementary materials). The difference between the measured and calculated value of H_2 might be due to gas leakage in our home-made prototype experimental system. According to gas chromatography after 3600 s, the H_2 gas evolved was 6.217×10^{-5} mol, whereas the current obtained by chronoamperometry is 3.49 mA.

$$n_{H_2}(\text{theoretical}) = \frac{0.00349\ (A)\ \times\ 3600\ (s)}{2\ \times\ 96485.33\ C \cdot mol^{-1}} =\ 6.511\ \times\ 10^{-5}\ mol$$

Consequently,

$$\eta_{Faradaic} = \frac{6.217\ \times\ 10^{-5}\ mol}{6.511 \times\ 10^{-5}\ mol} = 95.48\%$$

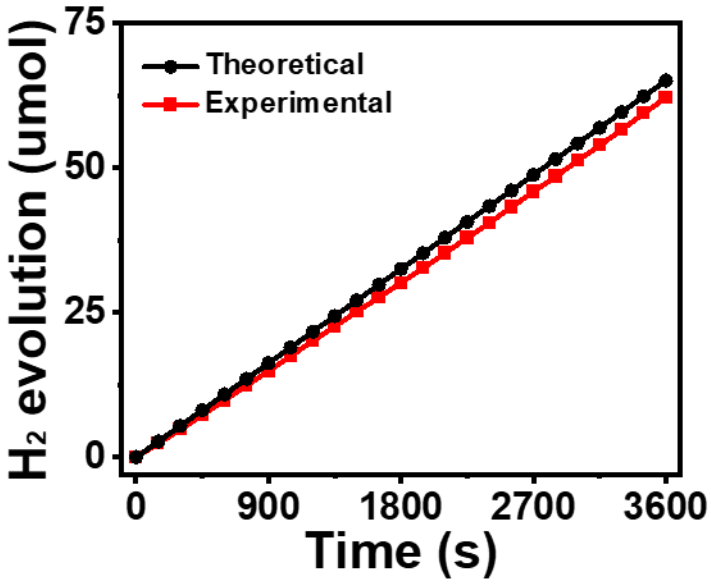

Figure 4.19 H_2 evolution of NiO/C/CdSe@CdS as a function of time at -0.4 V vs RHE under 100 mW/cm^2 illumination with AM 1.5 G filter. The evolution of H_2 exhibits a nearly linear increase over time (solid red curve). H_2 evolution is also calculated from the measured current (solid black curve).

The results obtained from these comparative experiments indicate that the high photocurrent density of the NiO/C electrode stems from the broad visible light absorption of QDs, the open porous nanostructure of NiO, and the increased conductivity due to the presence of carbon. For a convenient comparison, Table 4.2 summarizes the photoelectrocatalytic data of our porous NiO/C/CdSe and NiO/C/CdSe@CdS electrodes together with all reported photocathodes based on non-noble molecular catalysts and/or p-type semiconductors, which shows that the porous NiO/C/CdSe@CdS electrode obtained in this work present excellent performance.

Table 4.2 Comparison of different photocathodes in a three-electrode PEC cell.

Photocathode	Electrolyte/pH	Bias	Current density	Ref.
NiO/C/CdSe	**0.1 M Na_2SO_4 pH 6.8 solution**	**−0 V versus RHE**	**−51.87 μA/cm²**	**Present work**
NiO/C/CdSe@CdS	**0.1 M Na_2SO_4 pH 6.8 solution**	**−0 V versus RHE**	**−93.59 μA/cm²**	**Present work**
NiO/CdSe	0.1 M phosphate pH 6.8 buffer solution	−0 V versus RHE	−20 μA/cm²	[260]
NiO/CdSe/MoS_2	A buffer solution (pH 6) containing 0.3 M $C_6H_{12}N_4$, 0.1 M HCl, and 0.2 m KCl	−0.131 V versus RHE	−60 μA/cm²	[261, 262]
NiO/CdTe/NiS	0.1 M phosphate pH 6 buffer solution	−0.222 V versus Ag/AgCl	−40 μA/cm²	[263]
NiO/CdS	0.05 M Na_2SO_4	0 V versus NHE	−17.5 μA/cm²	[264]
NiO/CdS/cobaloxime	0.05 M Na_2SO_4	0 V versus NHE	−25 μA/cm²	[264]
NiO/CdSe (CdSe: 0.3 mg cm^{-2})	0.1 M Na_2SO_4 pH 6.8 solution	−0.1 V versus NHE	−60 μA/cm²	[265]
NiO/RuP_4-Co	0.1 M MES/0.1 M NaCl at pH 5.5	+0.14 V vs RHE	-84 ± 7 μA/cm²	[266]
NiO/ZnSe/CdS	0.1 M potassium phosphate	−0 V versus RHE	-57 μA/cm²	[267]
NiO/CdS/ZnSe	0.1 M potassium phosphate	−0 V versus RHE	-49 μA/cm²	[267]
NiO/CdSeTe	0.1 M phosphate buffer solution	−0.1 V vs NHE	-45 μA/cm²	[268]
NiO/Ru/Co	0.1 m phosphate pH 7 buffer solution	0.2 V versus NHE	-60 μA/cm²	[269]
NiO/PMI-6T-TPA/Pt_{ed}	0.1 m H_2SO_4	0.059 V versus RHE	-30 μA/cm²	[270]
NiO/PMI/30ALD/CoL_2	0.1 m H_2SO_4 and 0.1 m Na_2SO_4 in 1:1 H_2O:MeCN	−0.40 V versus Ag/$AgNO_3$	-25 μA/cm²	[271]
NiO/RuP3/Zr^{4+}/NiP	0.1 m Na_2SO_4 pH 3 solution	0.3 V versus RHE	-10 μA/cm²	[272]
NiO/RuP/CoHEC	0.1 m phosphate pH 7 buffer solution	−0.4 V versus Ag/AgCl	-13 μA/cm²	[222]

4.3 Conclusions and perspectives

In conclusion, the present study reports the fabrication of hollow ball-in-ball structure NiO/C nanocomposite by using Ni-based MOF as sacrificial template. To improve the solar absorption of this photocathode in the visible and near-infrared range, QDs were employed as sensitizers. Structural investigations confirmed that the NiO coated by carbon retained the MOFs original architecture intact, with a BET surface area of NiO/C of 535.68 ± 5.7 m^2/g. Upon illumination of visible light on the NiO/C/CdSe@CdS cathode, a photocurrent density of around -93.59 $\mu A/cm^2$ was generated at an applied potential of 0 V, and of -285 $\mu A/cm^2$ at -0.4V, in a neutral aqueous solution without any sacrificial reagent, cocatalyst, molecular linker and buffer solution. The enhanced activity and improved stability of the photocathode compared to the so far-reported NiO-based photocathodes is attributed to a higher surface area for loading sensitizers, better light scattering and a continuous conductive carbon matrix to facilitate the fast charge transfer. Overall, we have demonstrated in this work that NiO nanostructures derived from MOFs exhibit promising performance as photoelectrode materials for PEC hydrogen production. To generate higher photocurrents in NiO-based photocathodes, it will be necessary in the future to implement new design strategies for both the material and the electrode construction. Even though there are still many obstacles to overcome before they can be widely used for PEC water splitting, it is anticipated that the recent progress will inspire additional research in this field and lead to the development of more advanced MOF architectures for energy conversion applications.

5 QDS-FREE P-N HETEROJUNCTION PHOTOANODE

This chapter is based on the paper "*MOF-derived In_2O_3/CuO p-n heterojunction photoanode incorporating with graphene nanoribbon for solar hydrogen generation*" published on *Small* (2023) 2300606.

Link between articles:

As the first step, light absorption, particularly the absorption of visible light, can have a significant impact on PEC performance, as light harvesting determines the theoretical maximum efficiency for water splitting. In the previous chapters we have investigated the MOF-derived wide band gap MO. In order to improve their light absorption to visible light that accounts for 42-43% of total solar energy[273], we employed QDs as the sensitizer. Despite the enhanced visible light absorption, metal chalcogenides QDs often suffer from severe photo-corrosion. Therefore, we have to use the hole scavenger electrolyte to protect them (e.g., Na_2S and Na_2SO_3). In addition, there is another critical drawback: the toxicity of Cd-based chalcogenides causes serious environmental safety and human health issues, which hinder their mass production[274, 275].

Therefore, in this chapter, we move the focus on smaller band gap MO. Due to good capability of light absorption, small band gap MO have also been extensively explored for PEC water oxidation[276-279]. However, a common issue in the small bandgap MO is that the misalignment of their band edge positions with water electrolysis potentials. The conduction band positions of most of them (compared to proton reduction potentials) are low, so an external bias is required to achieve direct water splitting.

Indium oxide (In_2O_3), a typical n-type semiconductor material, stands out as a feasible candidate for PEC applications due to the appropriately positioned conduction and valence bands for water splitting, good conductivity, and high stability[280, 281]. However, pure In_2O_3 is hindered by its high recombination rate of photogenerated electron-hole pairs, which undoubtedly reduces its catalytic activity and the H_2 yield in water splitting reaction. Therefore, it is essential to suppress charge recombination in In_2O_3 photocatalyst. Numerous modification techniques can be effective to enhance the properties of MO photoelectrodes including surface functionalization, doping, and creating heterojunctions[282-284]. As we mentioned previously in chapter 3, building a p-n heterojunction structure in composite semiconductors is believed to be a better way to reduce the recombination rate of photogenerated carriers and broaden the light absorption range[135]. Several p-type materials have been considered as good candidates to build p-n junction for PEC applications, including p-Si, NiO, CuO, and III−V group p-type semiconductors (e.g., p-GaN, InP, and GaAs)[77, 265, 285, 286]. Most of them with narrow bandgap have an advantage of wide light absorption spectral range, they are subjected to photocorrosion when acting as the photoelectrodes during solar water splitting. Generally speaking, smaller band gap leads to higher vulnerability to photocorrosion.

Among them, copper oxide (CuO) has been attractive due to its abundant reserve, low cost, narrow bandgap (1.4-2.3 eV), nontoxicity, high light absorption coefficient, and high activity in photocatalytic splitting of water into H_2[287, 288]. An improvement in conductivity and a decrease in resistance are likely to result from a p-n heterojunction between p-type CuO and an n-type MO[135]. However, the traditional In_2O_3/CuO composite preparation method is generally by wet chemical method (e.g., hydrothermal method)[289, 290], which falls short in delivering materials with the desired properties like tailoring the morphology in an easily scalable way with a high degree of reproducibility[87]. Hence, the development of a simple synthetic procedure that meets all the requirements would be highly desirable.

Therefore, we designed a MOF-on-MOF heterostructure as the precursor to synthesize the MO composite with heterojunction. Through MOF-template method, we could not only achieve uniform contact between two single MO, but also retain the above advantages in the obtained MO heterojunction[133]. Thus, Cu-BDC (Cu-based MOFs) is selected to grow on the surface of hexagonal rod-shaped MIL-68(In) to form MIL-68(In)/Cu-BDC heterostructure, which as a precursor after annealing can form p-n heterojunction In_2O_3/CuO composite and retain the hollow hexagonal rod-shaped structure.

In addition, because of the hole accumulation that leads to self-reduction, CuO is expected to be electrochemically unstable during water reduction. To solve this problem, we could incorporate carbon allotropes low-dimensional (1D) nanostructure (like carbon nanotubes[140, 291, 292], graphene[293], and graphene oxide[294]) into semiconductor electrodes to enhance the hole transfer capability.

To address this issue, we could incorporate low-dimensional (1D) carbon allotropes nanostructures (such as carbon nanotubes[140, 291, 292], graphene[293], and graphene oxide[294]) into semiconductor electrodes to improve hole transfer capability Graphene nanoribbons (GNRs), a quasi-1-D nanoribbon carbon allotrope structures, have been already employed with success in a wide range of optoelectronic devices[295-297]. In this way, by adding a very small amount of GNRs, we can increase the charge transport efficiency by enabling a unidirectional flow of electrons. The optimized In_2O_3/CuO-GNRs photoanode exhibited a remarkable photocurrent density as high as 1.51 $mA \cdot cm^{-2}$ at 1.6 V vs RHE under one sun illumination (AM 1.5 G, 100 mW/cm^{-2}), which is 70% higher than the device based on pure In_2O_3/CuO photoanodes (0.89 $mA \cdot cm^{-2}$).

After 5 hours of irradiation, In_2O_3/CuO-GNRs exhibit good stability for PEC water splitting. Multiple characterization techniques were used to determine the role of the In_2O_3/CuO composite in charge transfer and band energy alignment. There will also be a discussion of the mechanisms underlying the formation of p-n junctions and the separation of photogenerated electrons and holes.

5.1 Experimental sections

The size and shape of In-MOF precursor can be controlled through a particle growth blocking event involving blocking agent interaction with particular facets of In-MOF and simultaneous particle growth interruption in a specific direction[148]. As described in Figure 5.1, In-MOFs were selectively generated with hexagonal rod, hexagonal lump, and hexagonal disk shapes.

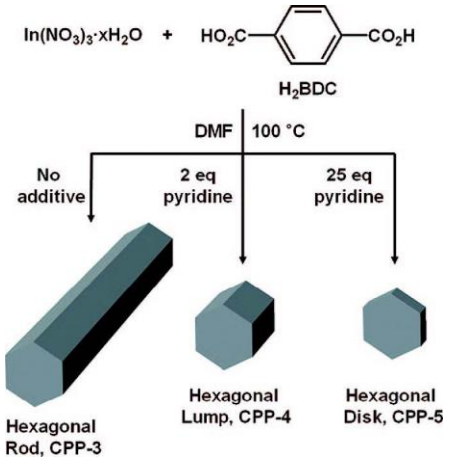

Figure 5.1 Selective Formation of Porous In-MOF, Hexagonal Rod (CPP-3), Hexagonal Lump (CPP-4), and Hexagonal Disk (CPP-5). Reprinted with permission[148]. Copyright 2008, The American Chemical Society.

Using the surfactant effect to control the growth direction of metallic or semiconducting crystalline nanomaterials is well studied and generally used to control shape[298, 299]. The formation of hexagonal disks instead of hexagonal rods can be rationalized by a blocking event in which pyridine reversibly coordinates to an indium center exposed on the hexagonal facet and simultaneously blocks particle growth in that direction[298-300]. Therefore, we synthesized all these three different morphologies of In-MOF (Figure 5.2). However, after annealing process, only the hexagonal rod-shaped morphology could maintain their morphology. Others, like nanorod and disk morphologies collapsed. Thus, we selected the hexagonal rod-shaped morphology for next synthesis part.

For synthesizing MIL-68(In)/Cu-BDC hexagonal rods precursor, we found that if we synthesized the In-MOF and the Cu-BDC, simultaneously, the Cu-BDC cannot distribute uniformly on the surface of In-MOF and tends to form agglomerates (Figure 5.3). However, when we separated the reaction in two steps, synthesizing first the In-MOF and then adding to it the Cu-precursor, they will share the organic ligand on the surface of the In-MOF, which can make them evenly dispersed on the surface of In-MOF (Figure 5.9).

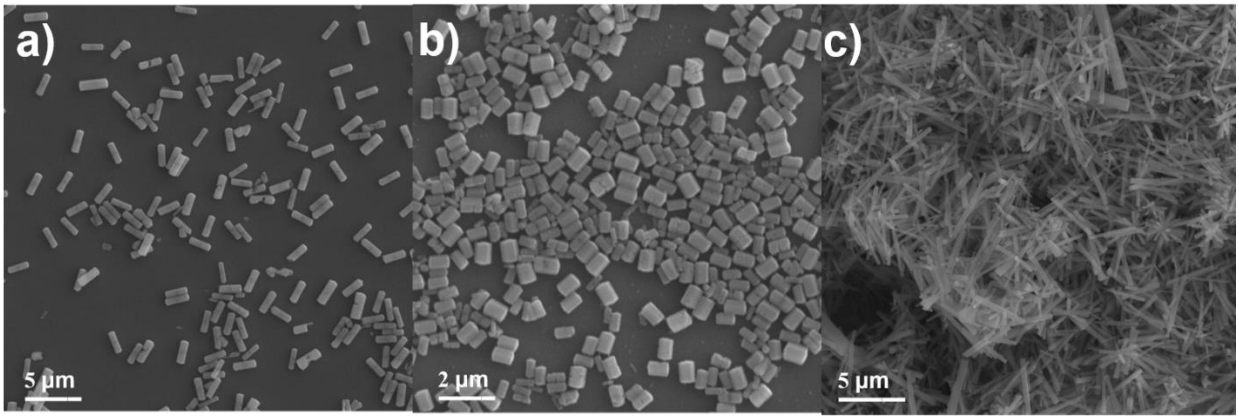

Figure 5.2 SEM of In-MOF with different concentration of pyridine.

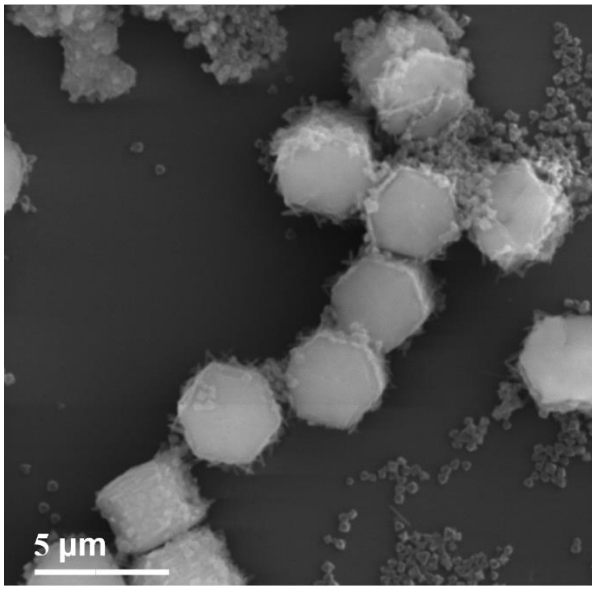

Figure 5.3 SEM of In-MOF/Cu-BDC.

5.2 Results and discussions

5.2.1 Synthesis and structural characterizations

The synthesis procedure to obtain In_2O_3/CuO composite with the morphology of hollow hexagonal rod-shaped is schematically depicted in Figure 5.4. First, a well-defined In-based MOF (MIL-68(In)) with hexagonal rod-shaped morphology was synthesized via a simple solvothermal reaction. The obtained MIL-68(In) are then dispersed in DMF solution (18 mL) with a copper precursor (copper nitrate hexahydrate) and annealed at 100 °C for 15 minutes. In this way, Cu-based MOFs (Cu-BDC) can be grown epitaxially on the MIL-68(In) to form MIL-68-In/Cu-BDC template. In_2O_3/CuO composites can be then obtained by annealing treatment of the MIL-68(In)/Cu-BDC template in an air atmosphere at 500 °C for 1 h.

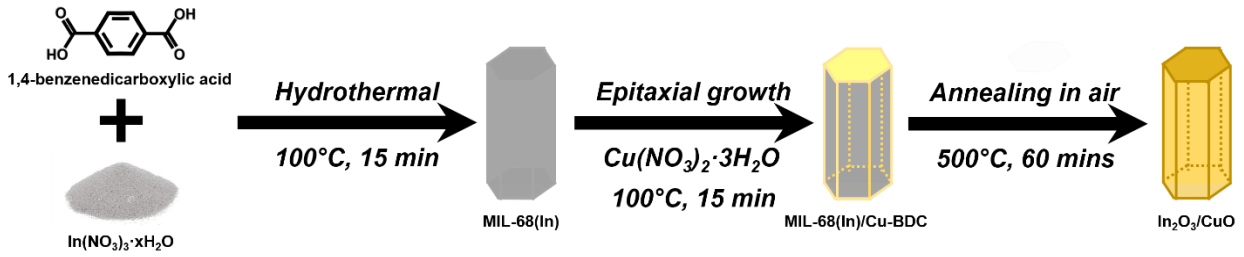

Figure 5.4 Schematic illustration of MOF-templated technique to obtain In_2O_3/CuO composite.

The calcination process of MIL-68(In), Cu-BDC, and MIL-68(In)/Cu-BDC was investigated by thermogravimetric analysis (TGA) (Figure 5.5). As shown in the TGA curve in Figure. 5.5a, the weight of the MIL-68(In) losses around 31.2 wt% from room temperature to 200 °C which could be attributed to the removal of the absorbed methanol and DMF solvent, whereas the noteworthy weight losses (around 45.9 wt%) from temperature 400 °C to 485 °C is assigned to the decomposition of the MOF skeleton. For the Cu-BDC part, the weight losses around 24.1 wt% from room temperature to 244 °C could be attributed to the removal of the absorbed methanol and DMF solvent, whereas the noteworthy weight losses (around 50.8 wt%) from temperature 370 °C to 313 °C is assigned to the decomposition of the MOF skeleton (Figure. 5.5b). On the basis of the TGA results, the pyrolysis temperature for MIL-68(In) and Cu-BDC precursor was set to 500 °C and 350 °C, respectively, with a heating rate of 5 °C·min^{-1} for 1 h in air atmosphere. The weight of the MIL-68(In)/Cu-BDC losses around 26 wt% from room temperature to 200 °C could be attributed to the removal of the absorbed methanol and DMF solvent, whereas the noteworthy weight losses (around 44.4 wt%) from temperature 400 °C to 487 °C is assigned to the decomposition of the MOF skeleton (Figure 5.5c). On the basis of the TGA result, the pyrolysis temperature for the MIL-

68(In)/Cu-BDC precursor was set to 500°C with a heating rate of 5 °C·min^{-1} for 1 h in air atmosphere to absolutely convert the as-prepared MIL-68(In)/Cu-BDC into the In_2O_3/CuO.

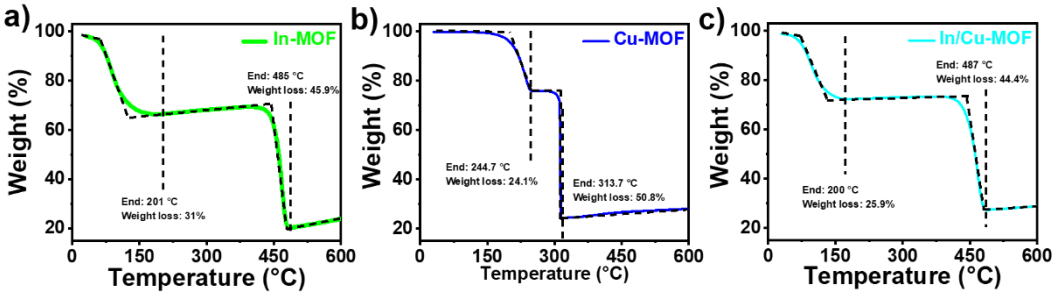

Figure 5.5 TGA curves of the as-obtained (a) MIL-68(In), (b) Cu-BDC, and (c) MIL-68(In)/Cu-BDC.

Power X-ray diffraction (XRD) was used to characterize MIL-68(In)/Cu-BDC (Figure 5.6a). The precursor exhibits sharp diffraction peaks and all peaks were consistent with a previous report[133, 301], confirming the formation of the MOF-on-MOF structure. Then, the XRD was also employed to characterize the crystallinity information of the CuO, In_2O_3 and In_2O_3/CuO (Figure 5.6b). The XRD patterns indicate that after annealing process, the obtained product In_2O_3/CuO is covered with CuO (JCPDS No. 41-0254) and In_2O_3 (JCPDS No. 44-1087) phases. Likewise, the Cu-BDC derived CuO and MIL-68(In) derived In_2O_3 also corresponse well with those of monoclinic CuO and In_2O_3. No other residues or contaminants in all three spectra indicate the high purity of the products. In addition, the concentration of GNRs in the In_2O_3/CuO-GRNs hybrid is below the XRD detection limit.

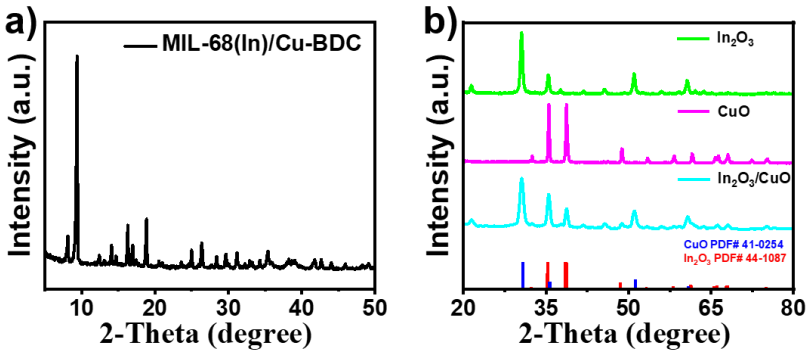

Figure 5.6 XRD patterns of (a) MIL-68(In)/Cu-BDC precursor and that of (b) In_2O_3 (green), CuO (magenta), and In_2O_3/CuO (cyan) (blue bar: monoclinic CuO, No. 41-0254; red bar: monoclinic In_2O_3, No.44-1087).

The morphologies and structure feature of In_2O_3/CuO were characterized by scanning electron microscopy (SEM), transmission electron microscopy (TEM), and high-angle annular dark-field scanning transmission electron microscope (HAADF-STEM). The single MIL-68(In) in the first synthesis step is characterized by

SEM in Figure 5.7, which reveals that hexagonal rod like morphology with average diameter and length of the rod were ~2.5 μm and ~7.8 μm respectively.

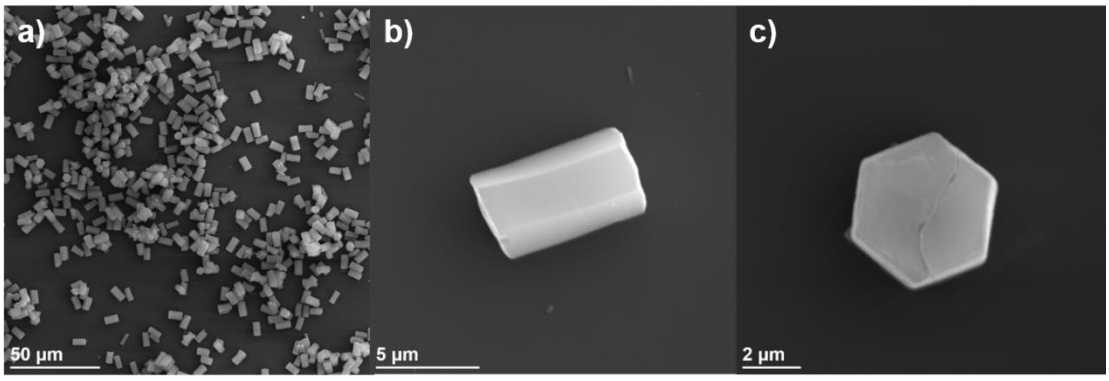

Figure 5.7 SEM images of MIL-68(In).

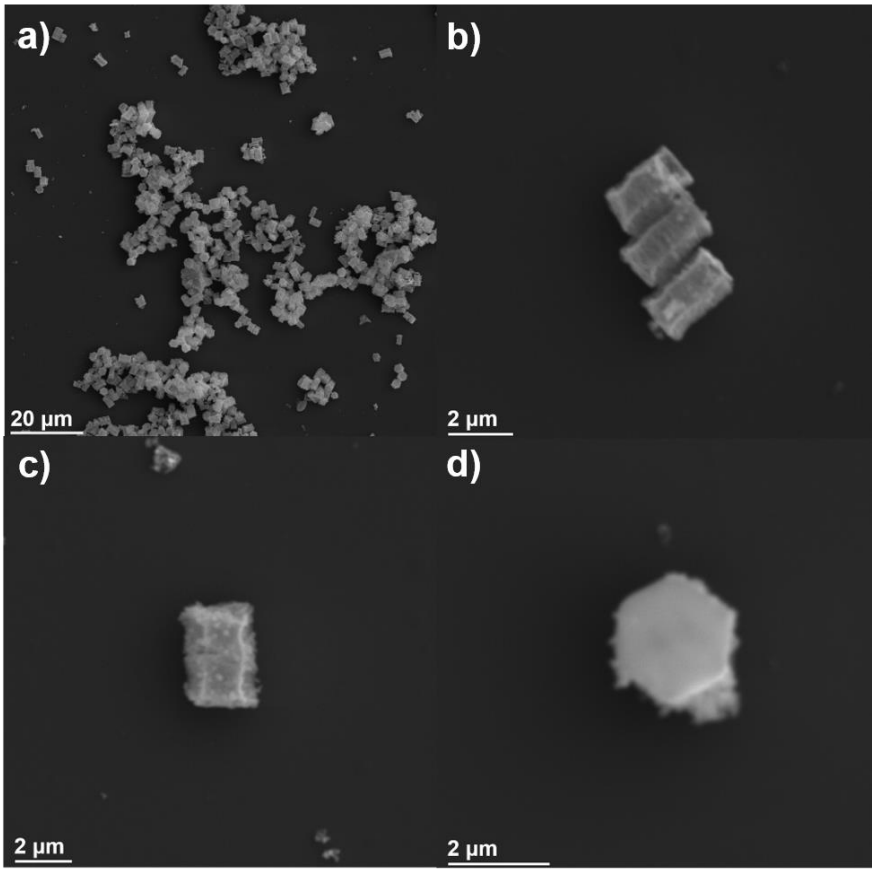

Figure 5.8 SEM images of In_2O_3/CuO after annealing MIL-68(In)/Cu-BDC.

As observed in Figure 5.9a, b, and c, the MIL-68(In)/Cu-BDC displays also a hexagonal rod-shaped morphology with a smooth surface. After the calcination in air atmosphere, the In_2O_3/CuO composite

retains the original hexagonal rod-shaped of MIL-68(In)/Cu-BDC (Figure 5.8) and reveals a hierarchical hollow structure (Figure 5.9d and e) as visible by the difference in contrast in the TEM image. On the other hand, the surface of the calcined particles becomes rough. This result can further validate the successful formation of In_2O_3/CuO heterojunction. From the high-resolution TEM (HRTEM) image of In_2O_3/CuO composite (Figure 5.9f), the d-spacings are 2.92 Å and 2.52 Å that can be indexed to the (222) plane of In_2O_3 and (110) plane of CuO, respectively. Energy-dispersive X-ray spectroscopy (EDX) analysis (Figure 5.10) confirms the presence of In, Cu, O, and C element in the In_2O_3/CuO composite. The elemental mapping images (Figure 5.9g-k) obtained in STEM mode clearly indicate relatively uniform distributions of In, Cu, O and C elements. Additionally, Figure 5.11 is the TEM and SAED for the pure In_2O_3 derived by MIL-68(In) and pure CuO derived by Cu-BDC. As can be seen in TEM, the In_2O_3 retains the rod like morphology after annealing, while the CuO is amorphous form. Selected-area electron diffraction (SAED) (Figure 5.11c and d) shows a group of diffraction rings which can be indexed to (211), (222) (400), (440) and (622) planes for In_2O_3, and (002), (111), and (202) planes for CuO. This result further validates the successful formation of In_2O_3 heterojunction.

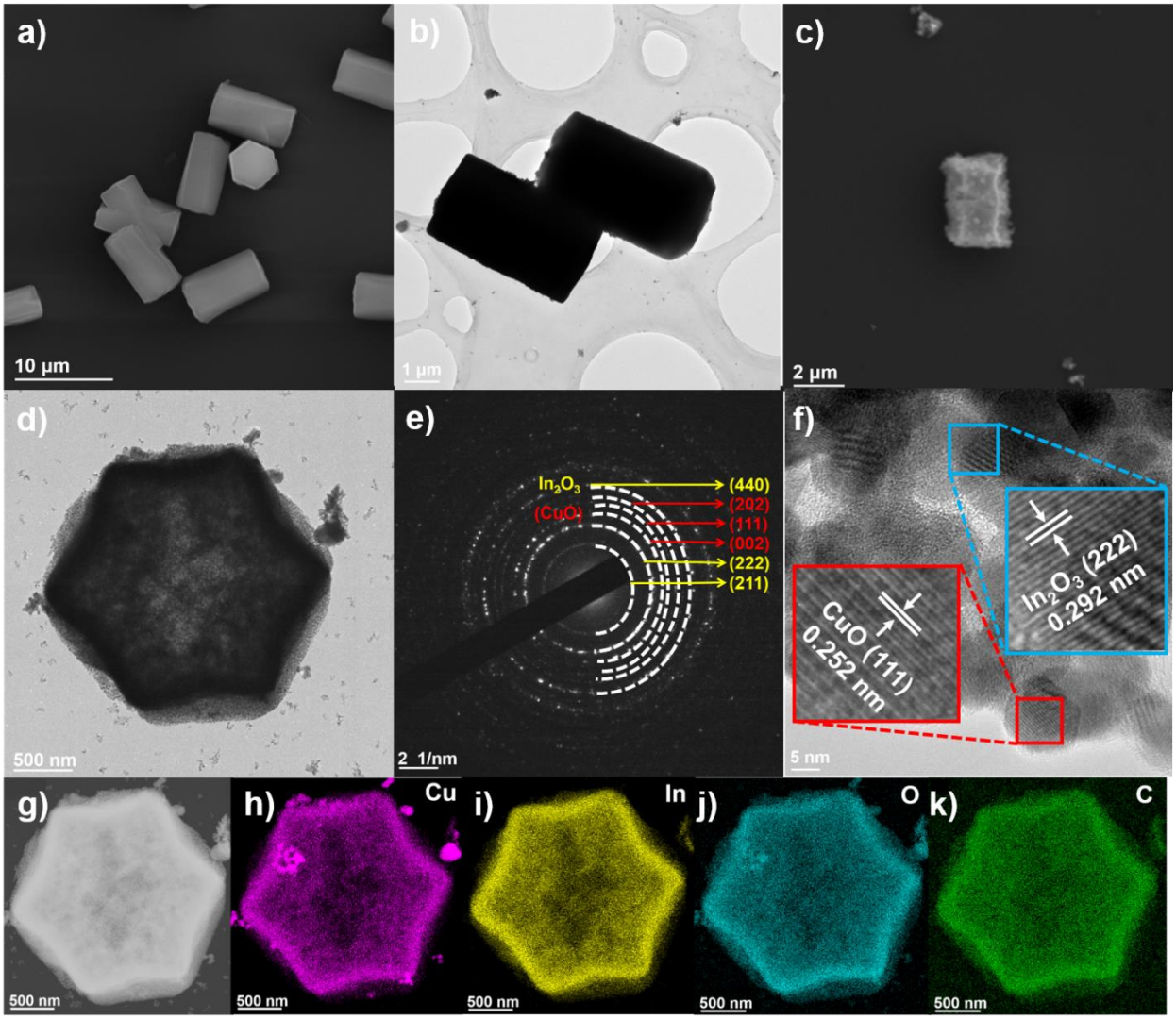

Figure 5.9 SEM (a) and TEM (b) images of the MIL-68(In)/Cu-BDC precursors. (c) SEM images of In_2O_3/CuO. (d) TEM images of In_2O_3/CuO (e) SAED pattern of In_2O_3/CuO. (f) HRTEM image of In_2O_3/CuO. (g-k) HAADF-STEM image and corresponding EDX elemental mapping of In, Cu, O, and C elements for In_2O_3/CuO composite.

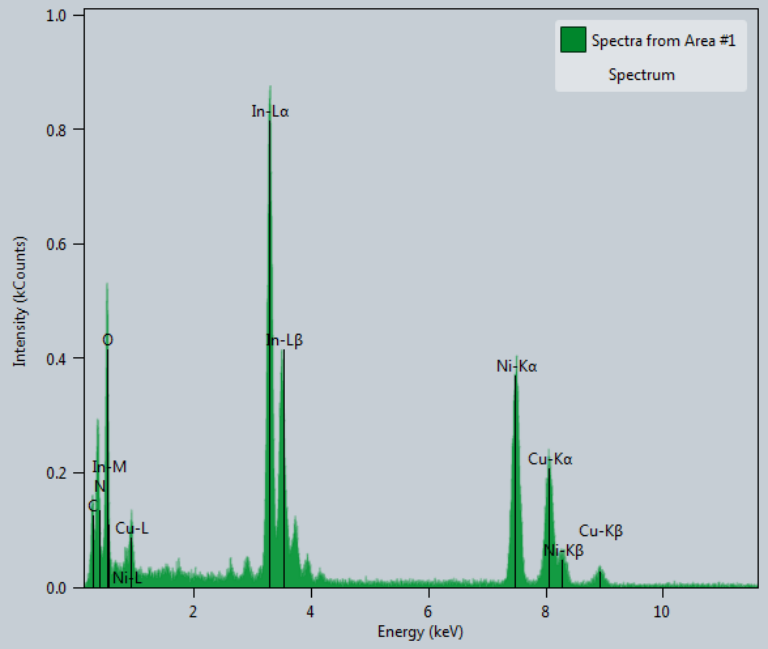

Figure 5.10 EDX spectrum of In_2O_3/CuO (Ni substrate).

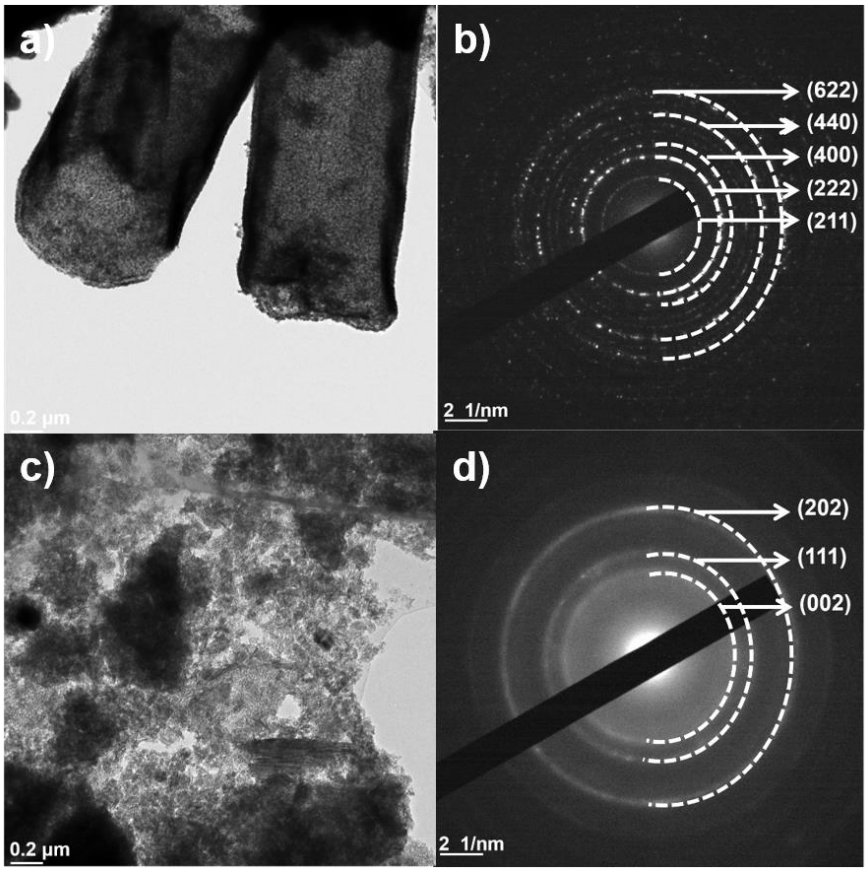

Figure 5.11 TEM and SAED images of (a, b) In_2O_3 from MIL-68(In) and (c, d) CuO from Cu-BDC.

Moreover, the surface electronic properties and chemical states of the In_2O_3/CuO were analyzed by X-ray photoelectron spectroscopy (XPS) (Figure 5.12). As expected, the survey XPS spectra reveal the presence of In, Cu, and O peaks (Figure 5.12a), consistent with the EDX and XRD results. The C 1s peak, associated to the widespread presence of carbon in the environment is also clearly observed. The high-resolution XPS spectrum of O 1s (Figure. 5.12c) could be deconvoluted into two major peaks at 532.5 eV and 529.9 eV assigned to the surface adsorbed oxygen groups (O-H bonds) and lattice oxygen (O_L), respectively[135, 289]. Likewise, In 3d XPS spectrum (Figure 5.12e) shows two distinct peaks, which are attributed to typical spin-orbit split In $3d_{5/2}$ (444.1 eV) and In $3d_{3/2}$ (451.6 eV), respectively. The result indicated that In (III) is the dominating state in the product. When compared with the In 3d XPS spectrum of pure In_2O_3, In $3d_{5/2}$ (444.0 eV), the binding energies are slightly shifted, which is due to the occurrence of band bending in the In_2O_3/CuO composite (Figure 5.15c)[289]. The high resolution XPS spectrum of Cu 2p (Figure 5.12b) exhibits two main peaks at 953.4 eV and 933.2 eV, corresponding to Cu $2p_{1/2}$ and Cu $2p_{3/2}$, respectively. The distance between these two peaks is around 20 eV, meaning a normal state of Cu^{2+}[133]. Additionally, the shake-up satellites (denoted as Sat.) at 940.6 eV, 942.4 eV, and 961.1 eV also confirm that the Cu atoms are in their +2 oxidation states, which represents the presence of CuO. Therefore, by combining the aforementioned results, it can be concluded that In_2O_3/CuO composite have been fabricated successfully.

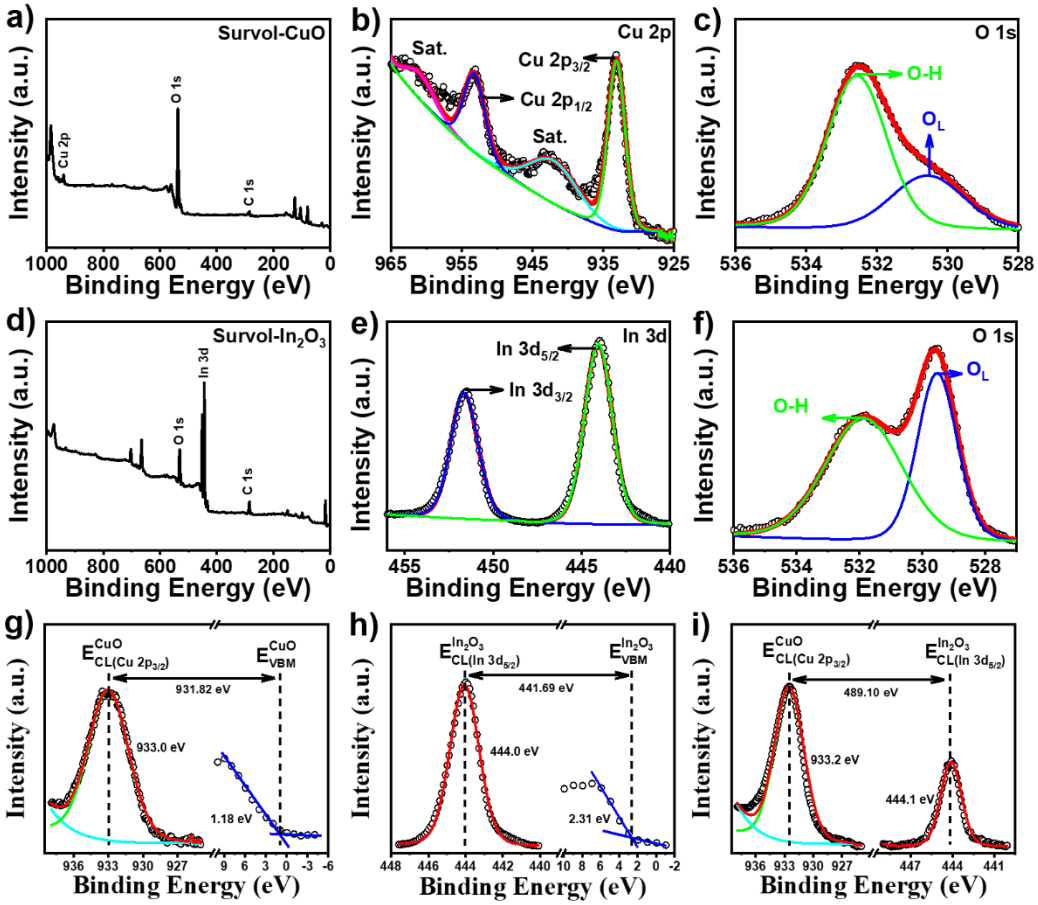

Figure 5.12 XPS survey spectra of (a) CuO. High resolution Cu 2p spectra (b). High resolution O1s spectra of CuO (c). Survol spectra of (d) In_2O_3. High resolution In 3d spectra (e). High resolution O1s spectra (f). XPS core level and valence spectra from (g) CuO from Cu-BDC, (h) In_2O_3 from MIL-68(In) and (i) In_2O_3/CuO composite.

5.2.2 Optical properties and band alignment at the heterojunction

Measuring the band edge positions of CuO and In_2O_3 and the band alignments is of importance to investigate the electron transfer process at the heterojunction. The combined analysis data from UV-DRS, UPS, and XPS was used to determine electronic band alignments.

The UV-DRS spectra of CuO, In_2O_3, and In_2O_3/CuO are shown in Figure 5.13. All of them present absorption in the UV-visible region. The absorption edges for pure CuO, In_2O_3, and In_2O_3/CuO are approximately 650, 460, and 550 nm, respectively. The In_2O_3/CuO-0.03% GNR is also tested with almost identical profiles, meaning that the presence of the GNR does not interfere with the optical property of In_2O_3/CuO composite (Figure 5.13a). According to the classical Tauc's formula[210], the optical bandgaps of E_{BG}(CuO) and E_{BG}(In_2O_3) are 1.79 eV, and 2.70 eV, respectively (Figure 5.13b). These Figures agree with the previously reported values for CuO[302, 303] and In_2O_3[36].

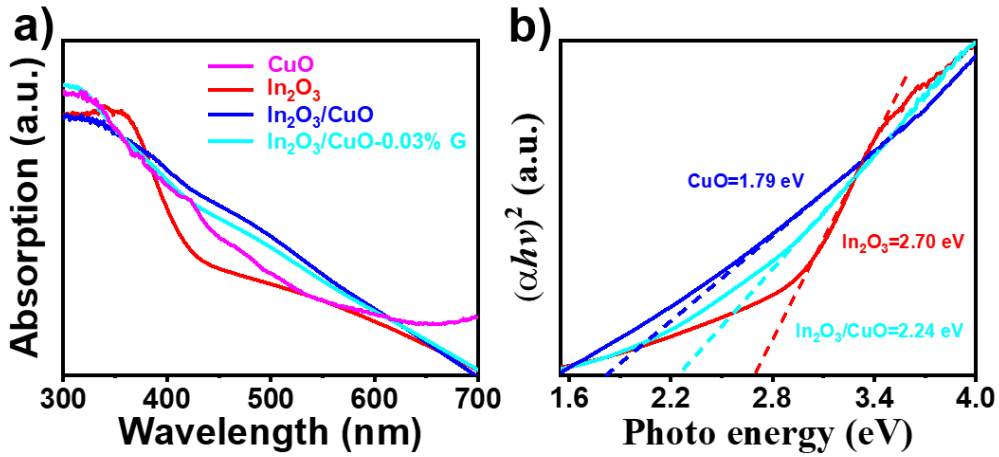

Figure 5.13 (a) UV-DRS spectra of CuO, In_2O_3, In_2O_3/CuO composite and In_2O_3/CuO-0.03 wt% GNRs. (b) The extrapolation of Tauc plots ($(\alpha h\nu)^2$ versus photon energy ($h\nu$)) for CuO, In_2O_3, and In_2O_3/CuO composite.

UPS with He I radiation (21.21 eV) was used to estimate the Fermi level (E_F) and valence band maximum (VBM) energy level. Figure 5.14 shows the UPS spectra of CuO, In_2O_3, and In_2O_3/CuO, respectively. According to the linear intersection method, the E_{VBM} of CuO is calculated to be -5.62 eV (vs vacuum). Similarly, the work function and the corresponding E_F level of CuO are estimated to be 5.42 and -5.42 eV (vs vacuum), respectively. Since the value of E_{BG}(CuO) is 1.79 eV, the conduction band minimum (E_{CBM}) is located at -3.83 eV (vs vacuum). According to the relationship between vacuum energy (E_{abs}) and the normal electrode potential (E^{Θ}), $E_{abs} = -E^{\Theta} - 4.44$ (at 298 K)(pH = 0)[304], the corresponding relative valence and conduction band positions are 1.18 and -0.61 eV (vs. NHE), respectively. Equally, the value of E_{VBM}, E_{CBM}, and E_F of In_2O_3 are 2.31, -0.39 and 0.2 eV (vs. NHE), respectively (Figure 5.16a).

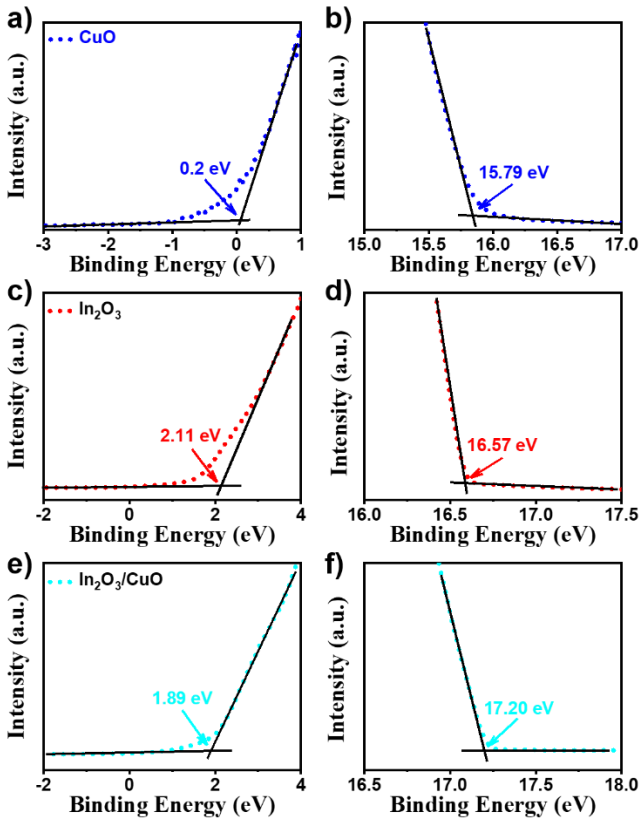

Figure 5.14 High binding energy cut-off (a) and low binding energy cut-off (b) of UPS spectra of CuO, In_2O_3, and In_2O_3/CuO composite.

When the two metal oxides are in contact, it will give rise to the formation of a p-n heterojunction at the interface and the new systems will attain equilibrium and form a new Fermi level. Finally, an interface depletion layer will be formed at the contact area of In_2O_3/CuO. In this case the band offsets of the nanocomposite can be determined following the method of Kraut[305]. To accurately determine the valence band offset (ΔE_{VBO}), the energy difference between the core level (E_{CL}) and the valence band maximum (E_{VBM}) in the pure materials (all data come from the corresponding XPS spectra), as well as the energy difference between the core levels at the interface of the heterostructure (ΔE_{CL}^{Int}) are needed (Figure 5.12g-i provides the XPS spectra). Eqs. (5.1) and (5.2) are used to calculate ΔE_{VBO} and ΔE_{CL}^{Int}, respectively:

$$\Delta E_{VBO} = (E_{CL}^{CuO} - E_{VBM}^{CuO}) - (E_{CL}^{In_2O_3} - E_{VBM}^{In_2O_3}) - \Delta E_{CL}^{Int} \quad (5.1)$$

$$\Delta E_{CL}^{Int} = (E_{CL}^{CuO} - E_{CL}^{In_2O_3})^{In_2O_3/CuO} \quad (5.2)$$

The conduction band offset (ΔE_{CBO}) can be readily obtained from the bandgap energies (E_{BG}) of the pure materials and ΔE_{VBO} (Eqs. (5.3)):

$$\Delta E_{CBO} = E_{BG}^{CuO} - E_{BG}^{In_2O_3} + \Delta E_{VBO} \ (5.3)$$

Combining the information gathered during XPS and UV-DRS spectra indicates that for the In_2O_3/CuO nanocomposite ΔE_{VBO} = 1.03 eV and ΔE_{CBO} = 0.12 eV (Figure 5.15b). The energy difference between the conduction and valence bands for the materials in the In_2O_3/CuO nanocomposite is about 0.10 eV higher in comparison with the values before contact. It is assumed that the difference value (D-value) between E_{CBM} and E_F of In_2O_3 and D-value between E_{VBM} and E_F of CuO keeps constant before and after contact. Besides, the possible band bending is not taken into account[306], the E_{VBM} of In_2O_3 in In_2O_3/CuO nanocomposite is calculated to be 2.51 eV (vs. NHE), and the E_{CBM} of CuO in In_2O_3/CuO nanocomposite is calculated to be -1.2 eV (vs. NHE).

Construction of energy diagram

In order to build the band diagram of pure materials (before contact) and the composite from UPS data, the position of the valence band maximum is obtained from Eq. (S1):

$$E_{VB} = E_F - X \ (S1)$$

Where E_F is the energy of the Fermi level and X is obtained from the extrapolation of the onsets in the UPS spectrum [X(CuO) = 0.2 eV, X(In_2O_3) = 2.11 eV, and X(In_2O_3/CuO) = 1.89 eV].

The Fermi level needed in Eq. (S1) is equivalent to the negative value for the work function (E_F = -Φ), and can be calculated using Eq. (S2):

$$\Phi = 21.21\ eV - E_{SO} \ (S2)$$

In Eq. (2) He I radiation (21.21 eV) is used to estimate the E_F and E_{SO} is the secondary electron onset, which is obtained from the linear extrapolation of the UPS spectrum indicated above.

[E_{SO}(CuO), E_{SO}(In_2O_3), and E_{SO}(In_2O_3/CuO) are 15.79 eV, 16.56 eV, and 17.2 eV].

Thus, the Φ of them could be obtained [Φ (CuO), Φ (In_2O_3), and Φ (In_2O_3/CuO) are 5.42 eV, 4.64 eV, and 4.01 eV]. (e.g., Φ(CuO) = 21.21 eV - E_{SO}(CuO) = 21.21 eV - 15.79 eV = 5.42 eV)

Moreover, based on the Eq (E_F = -Φ), their E_F are [E_F(CuO), E_F(In_2O_3), and E_F(In_2O_3/CuO) are -5.42 eV, -4.64 eV, and -4.01 eV].

According to the Eq S1, we could further get the E_{VBM} of them, which are [E_{VBM}(CuO) = -5.62 eV, E_{VBM}(In_2O_3) =-6.75 eV, and E_{VBM} (In_2O_3/CuO) = -5.90 eV]. (e.g., E_{VBM}(CuO) = E_F(CuO) - X = -5.42 eV-0.2 eV = -5.62 eV).

Then, the conduction band minimum potential can be readily calculated applying Eq. (S3):

$$E_{CB} = E_F + E_{BG} - X \ (S3)$$

where the bandgap energy E_{BG} is obtained by DRS measurements. [E_{BG}(CuO), E_{BG}(In_2O_3), and E_{BG}(In_2O_3/CuO) are 1.79 eV, 2.70 eV and 2.24 eV]. Their E_{CBM} are [E_{CBM}(CuO) = -3.83 eV, E_{CBM}(In_2O_3) =-4.05 eV, and E_{CBM} (In_2O_3/CuO) = -3.66 eV] (e.g., E_{CBM}(CuO) = E_F(CuO) + E_{BG}(CuO) - *X* = -5.42 eV + 1.79 eV -0.2 eV=-3.83 eV).

In the last, all the data could be transfer to NHE by Eq (E_{abs} = -E^{Θ}- 4.44).

1. [E_F(CuO) = 0.98 eV, E_F(In_2O_3) = 0.2 eV, and E_F(In_2O_3/CuO) = -0.43 eV] (e.g., E_F(CuO) = -E^{Θ}- 4.44, E^{Θ}(E_F(CuO)) = 5.42 eV - 4.44 eV = 0.98 eV);

2. [E_{VBM}(CuO) = 1.18 eV, E_{VBM}(In_2O_3) = 2.31 eV, and E_{VBM} (In_2O_3/CuO) = 1.46 eV] (e.g., E_{VBM}(CuO) = -E^{Θ}- 4.44, E^{Θ}(E_{VBM}(CuO)) = 5.62 eV - 4.44 eV = 1.18 eV);

3. [E_{CBM}(CuO) = -0.61 eV, E_{CBM}(In_2O_3) = -0.39 eV, and E_{CBM} (In_2O_3/CuO) = -0.78 eV] (e.g., E_{CBM}(CuO) = -E^{Θ}- 4.44, E^{Θ}(E_{VBM}(CuO)) = 3.83 eV - 4.44 eV = -0.61 eV).

The results are summarized in the Table 1.

As mentioned in the manuscript, The valence band offset (ΔE_{VBO}) and conduction band offset (ΔE_{CBO}) could be obtained via Eq (1), Eq (2), and Eq (3).

$$\Delta E_{VBO} = \left(E_{CL}^{CuO} - E_{VBM}^{CuO}\right) - \left(E_{CL}^{In_2O_3} - E_{VBM}^{In_2O_3}\right) - \Delta E_{CL}^{Int} \ (1)$$

$$\Delta E_{CL}^{Int} = (E_{CL}^{CuO} - E_{CL}^{In_2O_3})^{In_2O_3/CuO} \ (2)$$

$$\Delta E_{CBO} = E_{BG}^{CuO} - E_{BG}^{In_2O_3} + \Delta E_{VBO} \ (3)$$

Therefore, the energy difference between the core level (E_{CL}) and the valence band maximum (E_{VBM}) in the pure materials are shown in the Figure S8g-i.

$$\Delta E_{VBO} = \left(E_{CL}^{CuO} - E_{VBM}^{CuO}\right) - \left(E_{CL}^{In_2O_3} - E_{VBM}^{In_2O_3}\right) - \Delta E_{CL}^{Int}$$
$$= (933.0\ eV - 1.18\ \text{eV}) - (444.0\ eV - 2.31\ \text{eV}) - 489.10\ \text{eV} = 1.03\ \text{eV}$$

$$\Delta E_{CL}^{Int} = (E_{CL}^{CuO} - E_{CL}^{In_2O_3})^{In_2O_3/CuO} = (933.2\ eV - 444.1\ \text{eV})^{In_2O_3/CuO} = 489.10\ eV$$

$$\Delta E_{CBO} = E_{BG}^{CuO} - E_{BG}^{In_2O_3} + \Delta E_{VBO} = 1.79\ eV - 2.70\ eV + 1.03\ eV = 0.12\ eV$$

The obtained values are summarized in Table 5.1.

Table 5.1. Band energies of CuO, In_2O_3 and In_2O_3/CuO nanocomposite calculated by UV-DRS, XPS and UPS.

Sample	E_{BG} (eV)	E_F (eV)		E_{VBM} (eV)		E_{CBM} (eV)		ΔE_{VBO} (eV)	ΔE_{CBO} (eV)
		Vacuum	NHE	Vacuum	NHE	Vacuum	NHE		
CuO	1.79	-5.42	0.98	-5.62	1.18	-3.83	-0.61		
In_2O_3	2.70	-4.64	0.2	-6.75	2.31	-4.05	-0.39		
In_2O_3/CuO	2.24*	-4.01	-0.43	-6.95	2.51†	-3.24	-1.2‡	1.03	0.12

*Apparent E_g;

†The valence band maximum potential of In_2O_3 in In_2O_3/CuO nanocomposite;

‡The conduction band minimum potential of CuO in In_2O_3/CuO nanocomposite.

As shown in Figure 5.15b, the In_2O_3/CuO nanocomposite form a Type II (staggered) band alignment heterostructure, whose highly energetic conduction band favors the separation of charges. Under light irradiation, photogenerated electrons from CuO can favorably transfer into the conduction band of In_2O_3, while photogenerated holes from In_2O_3 migrate into the valence band of CuO. The built-in electric field of In_2O_3/CuO p-n heterojunction facilitates carrier migration, enhancing the separation efficiency of photogenerated electron-hole pairs and suppressing charge recombination.

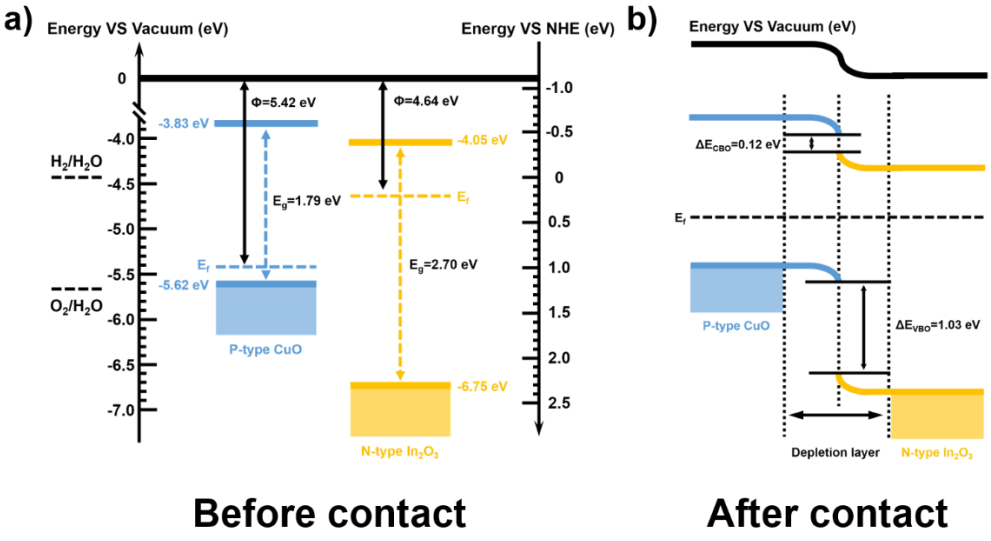

Figure 5.15 Energy band diagrams for (a) CuO and In_2O_3 before contact and (b) the energy band alignment of CuO/In_2O_3 heterojunction.

Besides, the Mott-Schottky (M-S) tests were also employed to confirm the semiconductor types of the pristine of CuO, In_2O_3, and In_2O_3/CuO composite. The positive slope of the M-S plot ascertains that the In_2O_3 is an n-type semiconductor (Figure. 5.16a)[307], and correspondingly, the negative slope demonstrates

the typical p-type semiconductor property of CuO (Figure. 5.16b)[303]. The Mott-Schottky plot of In_2O_3/CuO composite exhibits a typical inverted "V" shape, which is in accordance with the character of a p-n heterojunction[308, 309].

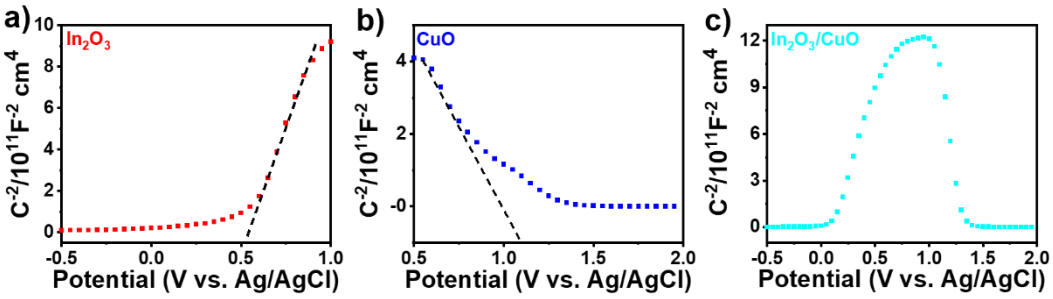

Figure 5.16 Mott-Schottky plot of CuO, In_2O_3, and In_2O_3/CuO composite.

5.2.3 PEC measurements

The In_2O_3/CuO composite was incorporated with different content of GNRs as photoanode to build a PEC device. A bare In_2O_3/CuO composite was also applied as a reference to highlight the effect of GNRs. Figure 5.17 depicts the comparison of the Raman spectra of pristine GNRs, In_2O_3/CuO and the In_2O_3/CuO-GNRs photoanode with an optimized concentration of GNRs. Raman spectra of pristine GNRs displays the characteristic of the D and G bands at 1347 cm^{-1} and 1578 cm^{-1} respectively, which are specific of the carbonaceous material[310]. The In_2O_3/CuO-0.03 wt% GNRs film clearly shows the presence of D and G bands at 1340 cm^{-1} and 1569 cm^{-1} respectively even at a very low concentration of GNRs (0.03 wt%) used. This confirms the presence of GNRs without any structural changes in the In_2O_3/CuO-GNRs hybrid photoanode after 30 min annealing at 500 °C under ambient conditions. However, the relative intensity of the D and G bands is lower, which may be due to the conformal coverage of GNRs by the In_2O_3/CuO composite. Moreover, the In_2O_3/CuO-GNRs hybrid photoanode was also analyzed via cross-section and plain-view SEM imaging corresponding EDX (Figure 5.18). The thickness of the In_2O_3/CuO-GNRs film is estimated to be ~12.2 μm. EDS mapping spectra verifies the presence of In, Cu, O, and C, respectively, consistent with the chemical composition in the In_2O_3/CuO-GNR photoanode.

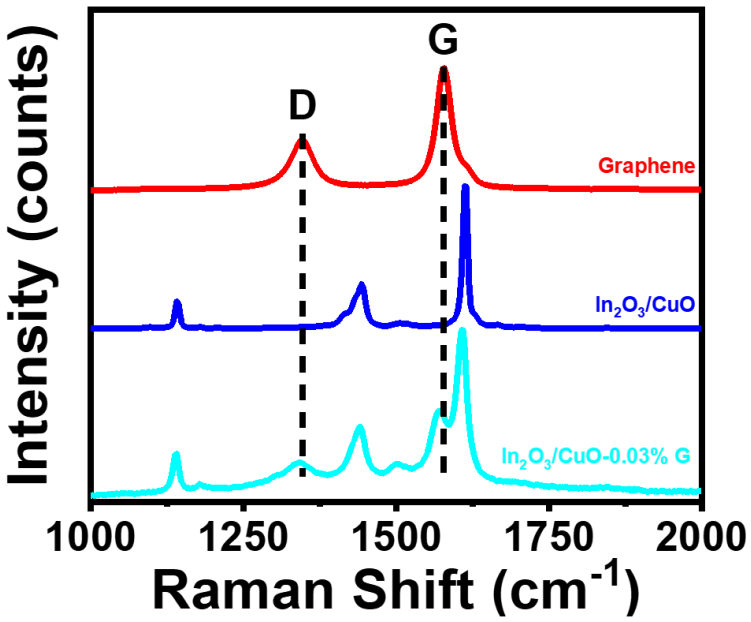

Figure 5.17 Raman spectra of bare GNRs (red line), In_2O_3/CuO composite (blue line), and In_2O_3/CuO-GNRs hybrid mesoporous film (cyan line).

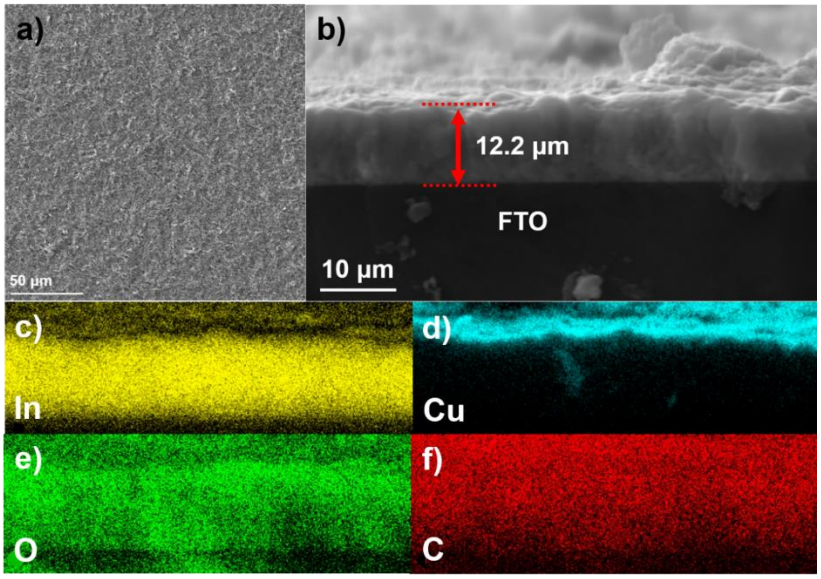

Figure 5.18 Plain-view and cross-sectional SEM image of In_2O_3/CuO-0.03 wt% GNRs (a and b); EDS mapping analysis of all the elements in relevant In_2O_3/CuO-0.03 wt% GNRs electrode including (c) In, (d) Cu, (e) O, and (f) C.

These In_2O_3/CuO-GNRs hybrid photoanodes were then used in a typical three-electrode configuration with a Pt counter electrode and an Ag/AgCl reference electrode (saturated with 3M KCl). The N_2-purged 1 M

NaOH aqueous solution (pH ~ 13) was used as electrolyte. All the PEC measurements were performed under dark, continuous and chopped illumination (one sun illumination AM 1.5 G, 100mW·cm^{-2}). Light-chopped linear sweep voltammetry (LSV) measurements on the different concentration of GNRs and In_2O_3/CuO photoanode as a benchmark are reported in Figure 5.19. All the samples show the low dark current densities indicate that the photocatalysts are almost inactive without light irradiation. Besides, the instant response of the photocurrent to the chopped illumination indicates an efficient separation of electron-hole pairs in the system induced by visible light. The photocurrent density (J_{ph}) for all samples gradually increases with the increase in the concentration of GNRs in In_2O_3/CuO composite at beginning. Figure 5.19g summarizes the variation of saturated photocurrent density values versus concentration of GNRs in the In_2O_3/CuO photoanode at 1.6 V RHE. In brief, the highest saturated photocurrent density of the PEC system based on bare In_2O_3/CuO photoanode is 0.89 mA·cm^{-2} (Figure 5.19a). After adding the 0.01 wt% of GNRs in In_2O_3/CuO film, the saturated photocurrent density increases to 0.98 mA·cm^{-2} (Figure 5.19b), then reaches to maximum value of 1.51 mA·cm^{-2} at 0.03 wt% of GNR content (Figure 5.19d), which is 70% higher than that of a PEC system based on the bare In_2O_3/CuO photoanode. Enhanced electron transport and reduced charge transfer resistance are mainly responsible for the increase in photocurrent density of In_2O_3/CuO-0.03 wt% GNRs photoanode (see Figure 5.21b).

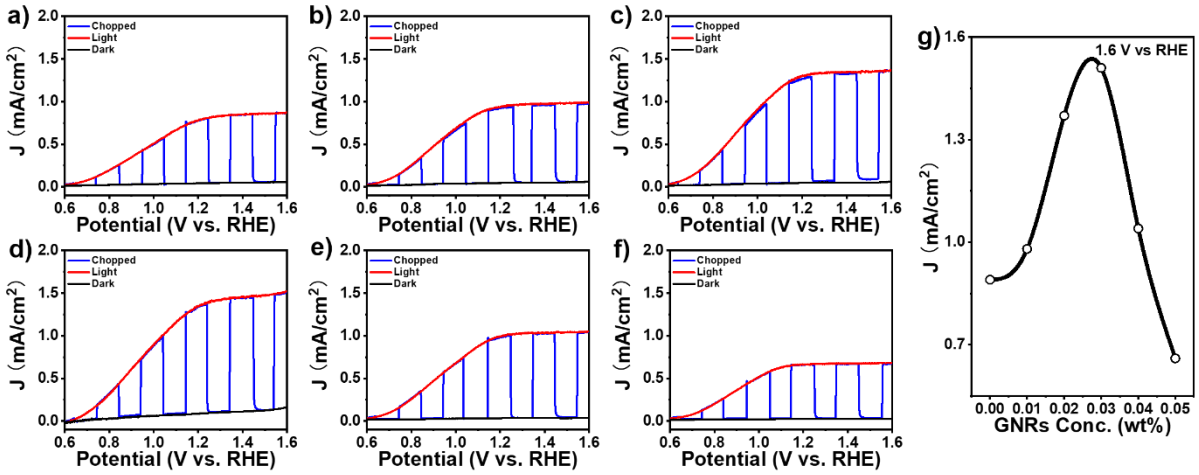

Figure 5.19 Photocurrent density-potential curves of PEC devices based on In_2O_3/CuO-GNRs hybrid photoanodes with different concentrations of GNRs under dark, continuous and chopped illumination (AM 1.5G, 100 mW·cm^{-2}): (a) 0.00 wt%;(b) 0.01 wt%; (c) 0.02 wt%; (d) 0.03 wt%; (e) 0.04 wt% and (f) 0.05 wt%. (g) Variation of current density at 1.6 V vs. RHE under 100 mW·cm^{-2} illumination with the concentration of GNRs.

The high electrical conductivity of the GNRs provides a direct pathway to the photoinjected electrons towards the FTO without passing through the numerous grain boundaries of In_2O_3/CuO composite, thereby enhancing electron collection. If the concentration of GNRs keeps increase, the photocurrent density

reduces from 1.51 mA·cm^{-2} to 1.04 mA·cm^{-2} (0.04 wt%) (Figure 5.19e) and 0.66 mA·cm^{-2} (0.05 wt%) (Figure 5.19f). The reason for this phenomenon is mainly due to the negative effect (e.g., crack formation) of the high concentration of GNRs, which acts as recombination centers during carrier transport, as well as the reduces optical transparency of the hybrid photoanode. Moreover, the small amount of GNRs (0.03 wt%) used does not affect the optical transparency of the film, as confirmed by UV-DRS tests (see Figure 5.13a).

To observe the influence of CuO on the properties of the photoanode, the same experiment was also carried out by preparing a pure In_2O_3 film via MOF template method (see experiment part 2.4) under same conditions. The J_{ph} of the pure In_2O_3 photocathode is only 0.3 mA·cm^{-2} (Figure 5.20a). In addition, after adding the same content (0.03 wt%) of GNRs in the In_2O_3 photocathode, the photocurrent density increases to 0.36 mA·cm^{-2} (Figure 5.20b), which is only 20% higher than that of a PEC system based on the bare In_2O_3 photoanode. However, if we compare the bare In_2O_3/CuO photoanode (0.89 mA·cm^{-2}) with the bare In_2O_3 photoanode, it shows an enhanced PEC performance of +196%. Finally, the comparative LSV plot of pure In_2O_3, In_2O_3/CuO, and In_2O_3/CuO-0.03 wt% GNRs is shown in Figure 5.21a and the chopped illumination data are also shown in Figure 5.21b. The limiting photocurrent density of In_2O_3/CuO-0.03 wt% GNRs is ~4.03 and 0.7-fold higher than those of pure In_2O_3 and In_2O_3/CuO, respectively. Therefore, the In_2O_3/CuO-0.03 wt% GNRs is considered as the best photoelectrode in PEC water splitting. It is verified that the incorporation of CuO in In_2O_3 can form p-n junction, which can improve efficiency of photogenerated electron-hole pairs, facilitate carrier migration, and suppress charge recombination. The PEC performance of the In_2O_3/CuO-0.03 wt% GNRs compares favorably to those of some representative In_2O_3 photocatalysts reported for PEC water splitting (Table 5.1).

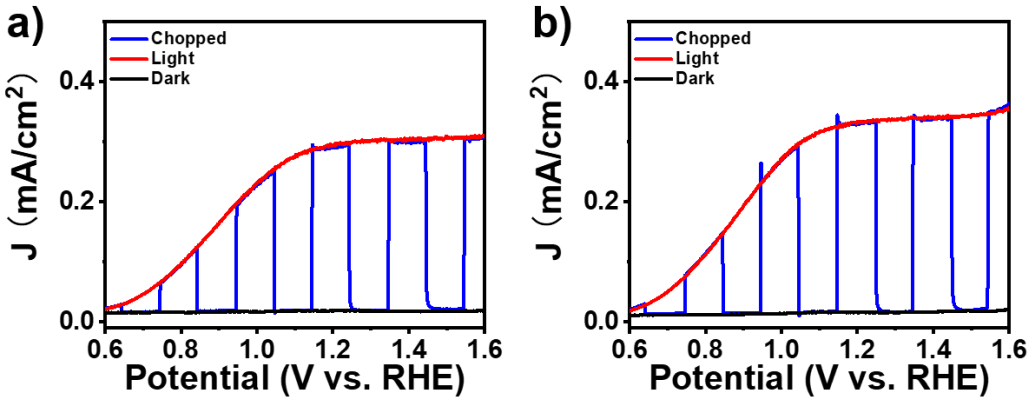

Figure 5.20 Photocurrent density of (a) In_2O_3 and (b) In_2O_3-0.03wt GNRs.

The long-term stability of the PEC device is a critical factor towards commercialization. In this work, the stability of In_2O_3/CuO-0.03 wt% GNRs photoanode PEC devices (photocurrent vs. time evolution) was measured at 1.4 V vs RHE under AM 1.5 G solar illumination (100 $mW \cdot cm^{-2}$) (Figure 5.21d). The photostability of the In_2O_3/CuO-0.03 wt% GNRs photoanode shows an obvious photocurrent density decreases in 0.5 M Na_2SO_4. However, this hybrid photoanode is very stable in NaOH (pH ~ 13), which can generate an unaltered photocurrent density of up to 18000 s. Moreover, the morphological robustness of the In_2O_3/CuO-0.03 wt% GNRs hollow hexagonal rod-shaped is checked after the long-term operation (Figure 5.22a, b), and it is observed that In_2O_3/CuO-0.03 wt% GNRs can retain its morphology.

Table 5.1 Comparison of the PEC performance of some representative In_2O_3 photocatalysts with literature.

Photocathode	Electrolyte	Light Source	Photocurrent density (mA cm^{-2})	Ref.
In_2O_3	**1 M NaOH**	**1 Sun**	**0.3 (1.6 V vs RHE)**	**Present work**
In_2O_3/CuO	**1 M NaOH**	**1 Sun**	**0.89 (1.6 V vs RHE)**	**Present work**
In_2O_3/CuO-0.03 wt% GNRs	**1 M NaOH**	**1 Sun**	**1.51 (1.6 V vs RHE)**	**Present work**
In_2O_3/TiO_2	0.1 M Na_2SO_4	350W Xe lamp	0.65 (No mention)	[311]
In_2S_3/CdS/NiOOH	0.25 M Na_2S and 0.35 M Na_2SO_3	1 Sun	1.01 (1.23 V vs RHE)	[312]
In_2O_3/In_2S_3	1 M NaOH	300W Xe lamp	0.53 (1.23 V vs RHE)	[282]
N-doped In_2O_3	0.1 M Na_2SO_4	300W Xe lamp	0.2 (1.6 V vs RHE)	[134]
In_2O_3/Fe_2O_3	0.1 M NaOH	300W Xe lamp	0.04 (1.6 V vs RHE)	[313]
In_2O_3/ZnO	0.5 M Na_2SO_4	300W Xe lamp	0.36 (0.5 V vs Ag/AgCl)	[314]
In_2O_3/Carbon	Triethanolamine (8 vol%)	300W Xe lamp	0.04 (0.2 V vs Hg/Hg_2Cl_2)	[315]

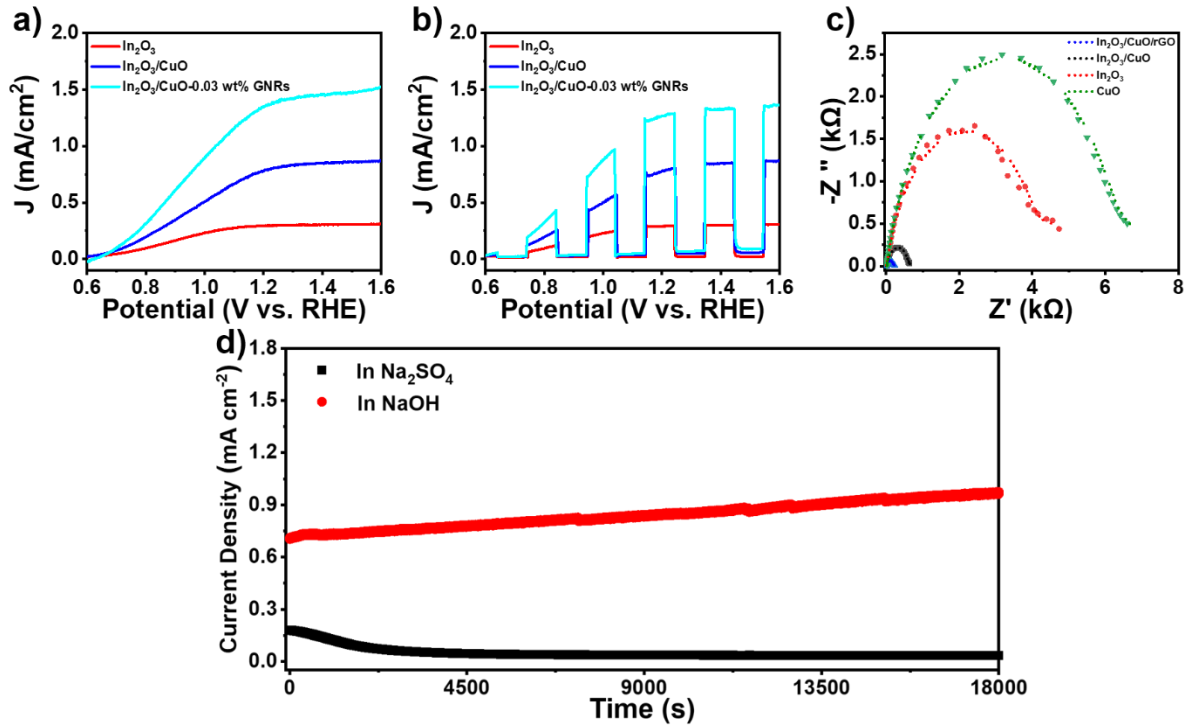

Figure 5.21 (a) Comparative LSV curve of bare In_2O_3, In_2O_3/CuO, and In_2O_3/CuO-0.03 wt% GNRs. (d) chopped illumination of bare In_2O_3, In_2O_3/CuO, and In_2O_3/CuO-0.03 wt% GNRs (Electrolyte 1M NaOH). (b) Nyquist plots of In_2O_3, In_2O_3/CuO composite, and In_2O_3/CuO-0.03 wt% GNRs. (d) Stability measurements (chronoamperometry) of In_2O_3/CuO-0.03 wt% GNRs in NaOH and Na_2SO_4 electrolyte, respectively (All experiments ran at 1.4 V versus RHE under AM 1.5 G illumination (100 mW cm^{-2})).

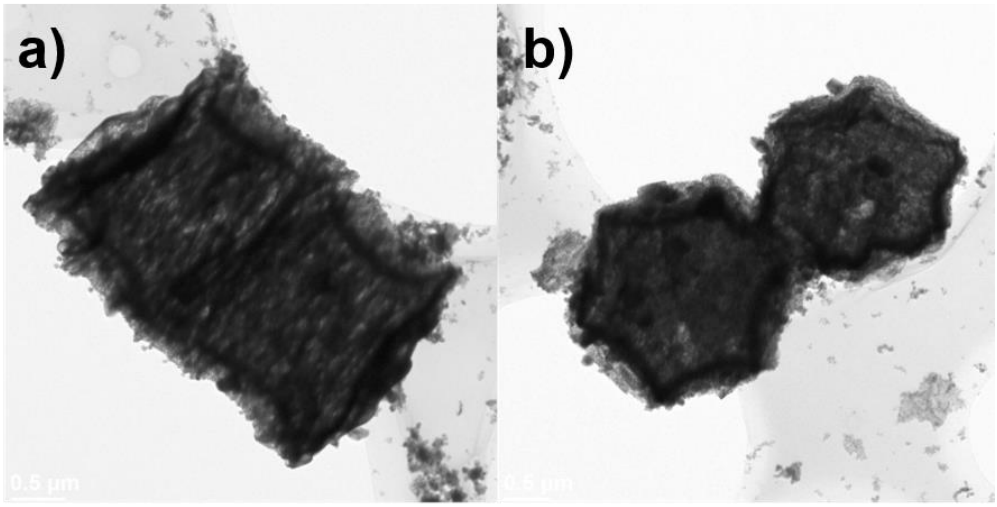

Figure 5.22 TEM images of the In_2O_3/CuO-0.03wt GNRs after the stability test from different directions.

To further investigate the mechanism behind the improved performance for different In_2O_3/CuO photoanodes on the carrier transport properties, electrochemical impedance spectroscopy (EIS)

measurements were carried out. In Figure 5.21c are reported the Nyquist plots recorded at 1.4 V versus RHE under 1 Sun (100 mW cm^{-2}) of representative samples of In_2O_3, In_2O_3/CuO and In_2O_3/CuO-0.03 wt% GNRs. To obtain information on the charge transport properties, the data were fitted with an equivalent circuit consisting of a series resistance (R_S) followed by two parallels of a space charge capacitance and resistance (C_{SC} and R_{SC}), double layer capacitance (C_{DL}), and charge transfer resistance (R_{CT}).). Similar models have been developed for related systems[117, 212]. By extrapolating the R_{CT} for each device (Table S1), an optimum amount of GNRs in the In_2O_3/CuO composite shows the lowest R_{CT}, indicating a higher charge transfer and an improved separation of electron/hole pairs. In addition, compared to pure In_2O_3 and In_2O_3/CuO, the RCT of In_2O_3/CuO reduced. This could be thanks to a more favorable band alignment that allow faster charge transfer by the built-in electric field of In_2O_3/CuO p-n heterojunction.

Table 5.2 The values of the R_{CT}.

Sample	R_{ct} (kΩ)
CuO	6420
In_2O_3	4270
In_2O_3/CuO	622
In_2O_3/CuO-0.03 wt% GNRs	109

H_2 production was further measured during the PEC measurement for In_2O_3/CuO-0.03 wt% GNRs. The produced H_2 gas was detected using a gas chromatograph (GC) equipped with a thermal conductivity detector at 1.4 V vs RHE under 1 sun. Argon gas was used as the carrier gas for GC analysis. The evolution of H_2 exhibits a nearly linear increase over time (solid red curve) (Figure 5.23). The evolution is also calculated from the measured current (solid black curve). The associated Faradaic efficiencies ($\eta_{Faradaic}$)(95.11%) are determined by comparing the amount of gas produced experimentally with the theoretically calculated values. The difference between the measured and calculated value of H_2 might be due to gas leakage in our home-made prototype experimental system.

According to gas chromatography after 5400s, the H_2 gas evolved was 7.947×10^{-6} mol, whereas the current obtained by chronoamperometry is 0.27 mA.

$$n_{H_2}(\text{theoretical}) = \frac{0.00027\ (A)\ \times\ 5400\ (s)}{2\ \times\ 96485.33\ C \cdot mol^{-1}} =\ 7.556\ \times\ 10^{-6}\ mol$$

Consequently,

$$\eta_{Faradaic} = \frac{7.556\ \times\ 10^{-6}\ mol}{7.947 \times\ 10^{-6}\ mol} = 95.11\%$$

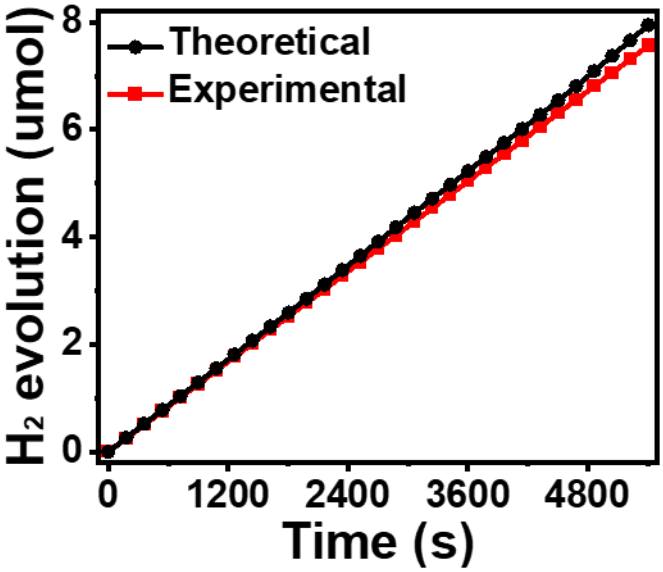

Figure 5.23. H_2 evolution of In_2O_3/CuO-0.03wt GNRs as a function of time at 1.4 V vs RHE under 100 mW/cm^2 illumination with AM 1.5 G filter. The evolution of H_2 exhibits a nearly linear increase over time (solid red curve). H_2 evolution is also calculated from the measured current (solid black curve).

5.3 Conclusions

In summary, In_2O_3/CuO hollow hexagonal rod-shaped has been successfully developed via MOF-templating technique. In order to improve the efficiency for PEC H_2 generation of the In_2O_3/CuO photoanode, small amounts of GNRs were employed for incorporation. Structural investigations confirmed that the In_2O_3/CuO retained the MOF morphology. By forming the p-n heterojunction, the In_2O_3/CuO-photoanode showed an enhanced current density of 196%, when compared with pure In_2O_3-phtoanode. This is mainly attributed to the improved separation efficiency of photogenerated electron-hole pairs in the In_2O_3/CuO-photoanode. On the other hand, an optimized concentration of GNRs in a In_2O_3/CuO-photoanode yielded the highest photocurrent density of 1.51 $mA \cdot cm^{-2}$, which is 70% higher than the In_2O_3/CuO photoanodes and also higher than the photocurrent density reported for the PEC performance of some representative In_2O_3 photocatalysts. This highlights that with an optimum GNRs concentration in the In_2O_3/CuO-photoanode improves the electrons transport (reducing the Rct), enabled by the directional path of GNRs for the photo-injected electrons towards FTO, without affecting the optical/structural properties, as indicated by EIS and UV-DRS. These findings provide fundamental insights that MOF-derived metal oxides nanostructures, indicating that this type of material can deliver promising performance in terms of stability and photocurrents as photoelectrode materials for PEC hydrogen production. While there are still many challenges ahead before they can be widely commercialized in PEC water splitting, it is anticipated that the recent progress will inspire further research in this area and lead to higher lever MOF architectures for applications in energy conversion.

6 CONCLUSIONS AND PERSPECTIVES

6.1 Conclusions

The increasing energy crisis and global warming impel researchers to put emphasis on the unremitting exploitation of solar energy. Due to their highly designable structures, tunable composition, large surface area, and controllable porosity, MOF have emerged as highly desirable templates or precursors for the synthesis of porous transition MO nanomaterials in recent years. Particularly, by adjusting the experimental conditions (such as thermolysis temperature, atmosphere, and time), it is simple to control the shape, size, crystal structure, and purity of MO or MO composites. Notably, the photocatalytic performance of the MO is primarily determined by these properties, making these MOF-derived MOs an ideal photocatalytic candidate for PEC water splitting. By selecting appropriate MOF precursors, for instance, it is possible to design porous MO materials with the desired dimension (1-D, 2-D, or 3-D).Controlling the dimension of the MO materials is crucial for optimizing the contact area between the MO photoelectrode and the electrolyte for achieving high PEC performance. Due to very few conventional methods offering the options for controlling the dimensionalities of the obtained MO products for the PEC applications, this clearly highlights the advantage of MOF-derived materials and their future significance. Besides the pure MO, MOF has also been demonstrated as highly versatile precursors to derive metal oxides nanocomposites and metal oxide/carbon nanocomposites. Therefore, the specific conclusions are as follows:

In Chapter 3, Ti-MOF (NH_2-MIL-125) makes an excellent candidate to be used as sacrificial template to synthesize TiO_2 with tuned morphology and crystal phase. By adjusting the thermolysis temperature, we could obtain different ratio of anatase and rutile, while simultaneously retaining the MOF crystal morphology. To extend the absorption range of the TiO_2 in the visible and near-infrared range, we employed metal chalcogenide QDs as sensitizers. The PEC performance of this QDs-based MOF-derived mixed-phase TiO_2 film photoanode was systematically investigated. After sensitization with core@shell CdSe@CdS QDs, the mixed-phase TiO_2 film exhibited an enhanced PEC device stability and PEC performance, compared with pure anatase commercial TiO_2 film. We further investigated the mechanism that underpins this enhancement, demonstrating that mixed-phase TiO_2 film exhibits a faster electron transfer rate than pure anatase commercial TiO_2 film, which could be ascribed to the favourable electronic band alignment and increased charge transfer. We believe that this finding represents a promising new concept of using MOF as templates for controlling the morphology and the crystalline phase of MO semiconductor to enhance the performance and stability of PEC hydrogen production. Moreover, this approach can be broadened to other solar technologies such as reduction of CO_2.

In chapter 4, we engineered a photocathode by using nickel-based MOFs (Ni-MOFs) as sacrificial templates, which allowed us to obtain hierarchical hollow NiO/carbon nanostructures. Therefore, to enhance the absorption spectrum of NiO in the visible range and near-infrared range, we sensitized the photocathode with metal chalcogenide QDs. After sensitization with core@shell CdSe@CdS QDs by SILAR method, the optimized PEC performance exhibited a photocurrent density of -93.6 $\mu A/cm^2$ at 0 V vs. RHE. This value was obtained at neutral pH (6.8) and without any sacrificial reagent, cocatalyst, or molecular linker. Compared to bare NiO, the enhancement is almost three-fold. We further investigated the mechanism that underlies this photocurrent enhancement. We found that the superior performance can be jointly attributed to the high surface area for loading sensitizers and light scattering of the nanohybrid as well as the presence of a carbon matrix that conducts electrons rapidly. Overall, in this work the MOF-template technique proved to be an easy and promising method to obtain an optimum MO with hierarchical hollow structure and carbon hybridization, which improves the performance of photocathodes for PEC hydrogen generation.

In chapter 5, a MOF-on-MOF heterostructure as the precursor to synthesize the MO composite with p-n heterojunction was developed. The MOF-template method was presented to achieve uniform contact between two single MO, but also retained the above advantages in the obtained MO heterojunction. In order to overcome the electrochemical instability of CuO, small carbon allotropes were incorporated inside the MO composite. In this way, the charge transport efficiency increased by enabling a unidirectional flow of electrons. The optimized photoanode exhibited a remarkable photocurrent density and show extremely stability. We found that the superior performance is due the forming the p-n heterojunction improved separation efficiency of photogenerated electron-hole pairs. The induce of carbon materials will also improves the electrons transport (reduces the R_{ct}), enabled by the directional path of carbon allotropes. This work provides fundamental insights that MOF-derived MO p-n heterostructures deliver promising performance as photoelectrode materials for PEC hydrogen production.

6.2 Perspectives

It is now possible to design and develop nanoporous transition MO materials with controlled size, shape, porosity, phase, and/or conductivity by selecting the proper organic and inorganic components of the MOF precursors and controlling the heat treatment conditions. Even though significant progress has already been made in the field of MOF-derived MO photocatalysts for PEC water splitting, significant efforts are still required to develop photoelectrodes with superior and stable PEC properties. Here, we will provide our perspectives on a few of the most significant issues in this field and also propose the following solutions. These problems are:

(1) Even though, MOFs-derived MO have shown some good potential as photoelectrode for water splitting applications, they are still suffering from poor electrical conductivity, leading to an overall increase in resistance. One way to address this problem is to synthesize the MOF-derived MO/carbon nanocomposites or combine the MOF-derived MO with highly conductive carbon substrates (e.g., rGO, carbon nanotubes, and graphene networks). However, in the MOF-derived MO/carbon nanocomposites, the concentration of the carbon is hard to control. Another method is hetero-atom doping with such as N, S and P which have been shown to be an effective method for enhancing the electronic properties of MOF-derived MO. Still, it is particularly challenging to efficiently and controllably incorporate dopants with large ionic radius into the lattice of MO. Therefore, it is highly desirable to develop new doping methods.

(2) Some MOF-derived MO has low electrode surface area, resulting in a small contact area between the electrode material and the electrolyte. One way to increase in surface area of MOF-derived MO can be achieved by preheating the MOF precursors under N_2 atmosphere before heat treating them in air. This is beneficial for preventing the rapid release of volatile gases (e.g., CO_x and NO_x), which would have caused the collapse of the frameworks.

(3) Due to the high crystallinity of MOF-derived MO, the diffusion distance of the electrolyte inside the pores of the MO are highly limited. On the one hand, decreasing the crystallinity of the MOF-derived MO materials can improve the distance at which the electrolyte can diffuse inside the pores of the MO. Previously, it was demonstrated that electrolyte could only diffuse for a short distance (20 nm) inside the pores of crystalline MO materials, whereas the same electrolyte could diffuse for a longer distance (50 nm) in amorphous MO materials. On the other hand, this problem could be solved by optimising the heating conditions to match the pore size of the MOF-derived MO with the electrolyte ion size. Nonetheless, achieving effective control of the heating conditions is difficult.

(4) In most cases, in PEC system, sacrificial electrolyte has been widely used in the system to consume electrons or holes, which is neither eco-friendly to water resources nor sustainable for practical application. As a result, replacing the sacrificial agent with a refractory contaminant or a precursor of a valuable chemical product should spur future research in this area.

(5) Although the rapid progress in the fabrication of MOF-derived MO or MO composites, a precise control over their structures is still absent because of the knowledge limited in the process of the transformation. Thus, a total understanding of this issue is urgently needed.

(6) Despite more than 20,000 MOFs have been designed[316], the choices of MOF as the template are still limited. Only limited types (MILs, UiOs, and ZIFs) MOF can be chosen as the proper precursors to fabricate the MO for photocatalysts or photoelectrode. Therefore, more alternative MOFs should be explored.

In conclusion, there is enormous potential for the development of phase-controlled, highly conductive MOF-derived MO for PEC water splitting applications, even though some barriers to MOF-derived MO still exist. We expect that in the near future, the functionalization of MOF-derived MO through heteroatomic doping or hybridization with carbonaceous materials will help to realize the potential use of MOF-derived MO for high-performance photoelectrode, which could further push the PEC performance. Furthermore, with respect to the commercialization of MOF-derived MO, it is highly important that they are tested to match the practical standard of commercial electrodes. Hence, in the future, significant research efforts should be carried out for the synthetic method modifications of MOF-derived MO and to increase their processability for commercial applications. Finally, it is suggested that future research on MOF-derived MO nanomaterials address the challenges in this field in order to fully unlock their true potential for PEC water splitting applications.

BIBLIOGRAPHY

[1] P. Poizot, F. Dolhem, Energy & Environmental Science 4 (2011) 2003.

[2] A. Olabi, K. Obaideen, K. Elsaid, T. Wilberforce, E.T. Sayed, H.M. Maghrabie, M.A. Abdelkareem, Renewable and Sustainable Energy Reviews 153 (2022) 111710.

[3] J. Curtin, C. McInerney, B.Ó. Gallachóir, C. Hickey, P. Deane, P. Deeney, Renewable and Sustainable Energy Reviews 116 (2019) 109402.

[4] C. Zheng, D.M. Kammen, Energy Policy 67 (2014) 159.

[5] N.S. Lewis, D.G. Nocera, Proceedings of the National Academy of Sciences 103 (2006) 15729.

[6] Z. Wang, C. Li, K. Domen, Chemical Society Reviews 48 (2019) 2109.

[7] X. Zhang, M. Schwarze, R. Schomäcker, R. van de Krol, F.F. Abdi, Nature Communications 14 (2023) 991.

[8] T. Hisatomi, J. Kubota, K. Domen, Chemical Society Reviews 43 (2014) 7520.

[9] M. Balat, International journal of hydrogen energy 33 (2008) 4013.

[10] P.A. Pilavachi, A.I. Chatzipanagi, A.I. Spyropoulou, International Journal of hydrogen energy 34 (2009) 5294.

[11] A. Sartbaeva, V. Kuznetsov, S. Wells, P. Edwards, Energy & Environmental Science 1 (2008) 79.

[12] W. Yang, J. Park, H.-C. Kwon, O.S. Hutter, L.J. Phillips, J. Tan, H. Lee, J. Lee, S.D. Tilley, J.D. Major, Energy & Environmental Science 13 (2020) 4362.

[13] W.-H. Cheng, M.H. Richter, M.M. May, J. Ohlmann, D. Lackner, F. Dimroth, T. Hannappel, H.A. Atwater, H.-J. Lewerenz, ACS Energy Letters 3 (2018) 1795.

[14] A. Fujishima, K. Honda, nature 238 (1972) 37.

[15] K. Sivula, The journal of physical chemistry letters 4 (2013) 1624.

[16] S.J. Moniz, S.A. Shevlin, D.J. Martin, Z.-X. Guo, J. Tang, Energy & Environmental Science 8 (2015) 731.

[17] T. Lopes, L. Andrade, F. Le Formal, M. Gratzel, K. Sivula, A. Mendes, Physical Chemistry Chemical Physics 16 (2014) 16515.

[18] A. Fujishima, X. Zhang, D.A. Tryk, Surface science reports 63 (2008) 515.

[19] S.Y. Jeong, J. Song, S. Lee, Applied Sciences 8 (2018) 1388.

[20] S. Kim, N.T. Nguyen, C.W. Bark, Applied Sciences 8 (2018) 1526.

[21] X. Chen, C. Li, M. Grätzel, R. Kostecki, S.S. Mao, Chemical Society Reviews 41 (2012) 7909.

[22] M. Weber, M. Dignam, International Journal of Hydrogen Energy 11 (1986) 225.

[23] J.R. Bolton, S.J. Strickler, J.S. Connolly, Nature 316 (1985) 495.

[24] A. Murphy, P. Barnes, L. Randeniya, I. Plumb, I. Grey, M. Horne, J. Glasscock, International journal of hydrogen energy 31 (2006) 1999.

[25] R. Van de Krol, M. Grätzel, Photoelectrochemical hydrogen production, Springer, 2012.

[26] P. Dias, A. Mendes, Hydrogen Production from Photoelectrochemical Water Splitting, in: R.A. Meyers (Ed.) Encyclopedia of Sustainability Science and Technology, Springer New York, New York, NY, 2017, pp. 1.

[27] R. van de Krol, Y. Liang, J. Schoonman, Journal of Materials Chemistry 18 (2008) 2311.

[28] A. Vilanova, T. Lopes, C. Spenke, M. Wullenkord, A. Mendes, Energy Storage Materials 13 (2018) 175.

[29] R. Li, Chinese Journal of Catalysis 38 (2017) 5.

[30] A. Frank, In Energy resources through photochemistry and catalysis, M. Gratzel, Ed, Academic Press: New York, 1983.

[31] A.J. Nozik, Annual review of physical chemistry 29 (1978) 189.

[32] S.R. Morrison, S. Morrison, Electrochemistry at semiconductor and oxidized metal electrodes, Springer, 1980.

[33] Y. Yang, S. Niu, D. Han, T. Liu, G. Wang, Y. Li, Advanced Energy Materials 7 (2017) 1700555.

[34] J.Z. Zhang, MRS bulletin 36 (2011) 48.

[35] I. Concina, Z.H. Ibupoto, A. Vomiero, Advanced Energy Materials 7 (2017) 1700706.

[36] R. Marschall, Advanced Functional Materials 24 (2014) 2421.

[37] A.L. Linsebigler, G. Lu, J.T. Yates Jr, Chemical reviews 95 (1995) 735.

[38] S. Sze, Google Scholar There is no corresponding record for this reference (1993) 790.

[39] R. Hoffmann, Solids and surfaces: a chemist's view of bonding in extended structures, John Wiley & Sons, 2021.

[40] Y. Yu, Y. Huang, Y. Yu, Y. Shi, B. Zhang, Nano Energy 43 (2018) 236.

[41] S. Li, W. Xu, L. Meng, W. Tian, L. Li, Small Science (2022) 2100112.

[42] Y. Wang, J. Zhang, M.-S. Balogun, Y. Tong, Y. Huang, Materials Today Sustainability 18 (2022) 100118.

[43] M. Ma, K. Zhang, P. Li, M.S. Jung, M.J. Jeong, J.H. Park, Angewandte Chemie 128 (2016) 11998.

[44] Q. Li, X. Li, S. Wageh, A.A. Al-Ghamdi, J. Yu, Advanced Energy Materials 5 (2015) 1500010.

[45] J. Liu, Y. Liu, N. Liu, Y. Han, X. Zhang, H. Huang, Y. Lifshitz, S.-T. Lee, J. Zhong, Z. Kang, Science 347 (2015) 970.

[46] X.Y. Liu, H. Chen, R. Wang, Y. Shang, Q. Zhang, W. Li, G. Zhang, J. Su, C.T. Dinh, F.P.G. de Arquer, Advanced Materials 29 (2017) 1605646.

[47] F. Cheng, X. Jiang, Z. Zhang, R. Ma, T. Sasaki, F. Pan, X. Jing, Chemical Communications 55 (2019) 2417.

[48] T. Yang, H. Wang, X.M. Ou, C.S. Lee, X.H. Zhang, Advanced Materials 24 (2012) 6199.

[49] M. Wu, J. Zhang, B.-b. He, H.-w. Wang, R. Wang, Y.-s. Gong, Applied Catalysis B: Environmental 241 (2019) 159.

[50] M. Qiao, J. Liu, Y. Wang, Y. Li, Z. Chen, Journal of the American Chemical Society 140 (2018) 12256.

[51] M.Z. Rahman, C.W. Kwong, K. Davey, S.Z. Qiao, Energy & Environmental Science 9 (2016) 709.

[52] P. Ganguly, M. Harb, Z. Cao, L. Cavallo, A. Breen, S. Dervin, D.D. Dionysiou, S.C. Pillai, ACS Energy Letters 4 (2019) 1687.

[53] J. Ran, G. Gao, F.-T. Li, T.-Y. Ma, A. Du, S.-Z. Qiao, Nature communications 8 (2017) 1.

[54] B.D. James, G.N. Baum, J. Perez, K.N. Baum, DOE report (2009).

[55] A. Wolcott, W.A. Smith, T.R. Kuykendall, Y. Zhao, J.Z. Zhang, Small 5 (2009) 104.

[56] K. Arifin, R.M. Yunus, L.J. Minggu, M.B. Kassim, International Journal of Hydrogen Energy 46 (2021) 4998.

[57] G. Wang, H. Wang, Y. Ling, Y. Tang, X. Yang, R.C. Fitzmorris, C. Wang, J.Z. Zhang, Y. Li, Nano letters 11 (2011) 3026.

[58] Z. Kang, H. Si, S. Zhang, J. Wu, Y. Sun, Q. Liao, Z. Zhang, Y. Zhang, Advanced Functional Materials 29 (2019) 1808032.

[59] Y. Hu, X. Yan, Y. Gu, X. Chen, Z. Bai, Z. Kang, F. Long, Y. Zhang, Applied Surface Science 339 (2015) 122.

[60] M. Ma, Y. Huang, J. Liu, K. Liu, Z. Wang, C. Zhao, S. Qu, Z. Wang, Journal of Semiconductors 41 (2020) 091702.

[61] S. Shen, S.A. Lindley, X. Chen, J.Z. Zhang, Energy & Environmental Science 9 (2016) 2744.

[62] S. Hilaire, M.J. Süess, N. Kränzlin, K. Bieńkowski, R. Solarska, J. Augustyński, M. Niederberger, Journal of Materials Chemistry A 2 (2014) 20530.

[63] P.M. Rao, I.S. Cho, X. Zheng, Proceedings of the Combustion Institute 34 (2013) 2187.

[64] S. Wang, P. Chen, J.H. Yun, Y. Hu, L. Wang, Angewandte Chemie 129 (2017) 8620.

[65] J.H. Kim, J.S. Lee, Advanced Materials 31 (2019) 1806938.

[66] J.H. Kim, J.S. Lee, Energy and Environment Focus 3 (2014) 339.

[67] Y.-K. Hsu, C.-H. Yu, Y.-C. Chen, Y.-G. Lin, Electrochimica Acta 105 (2013) 62.

[68] I.V. Bagal, N.R. Chodankar, M.A. Hassan, A. Waseem, M.A. Johar, D.-H. Kim, S.-W. Ryu, International Journal of Hydrogen Energy 44 (2019) 21351.

[69] J. Jian, J. Sun, Solar RRL 4 (2020) 2000111.

[70] R. Fan, Z. Mi, M. Shen, Optics express 27 (2019) A51.

[71] L.E. Garner, K.X. Steirer, J.L. Young, N.C. Anderson, E.M. Miller, J.S. Tinkham, T.G. Deutsch, A. Sellinger, J.A. Turner, N.R. Neale, ChemSusChem 10 (2017) 767.

[72] L. Hallstrom, C. Tossi, I. Tittonen, The Journal of Physical Chemistry C 125 (2021) 12478.

[73] M. Alqahtani, S. Sathasivam, F. Cui, L. Steier, X. Xia, C. Blackman, E. Kim, H. Shin, M. Benamara, Y.I. Mazur, Journal of Materials Chemistry A 7 (2019) 8550.

[74] S. Chandrasekaran, Y.-L.T. Ngo, L. Sui, E.J. Kim, D.K. Dang, J.S. Chung, S.H. Hur, Dalton Transactions 46 (2017) 13912.

[75] J.A. Nasir, Z. ur Rehman, S.N.A. Shah, A. Khan, I.S. Butler, C.R.A. Catlow, Journal of Materials Chemistry A 8 (2020) 20752.

[76] Y. Fu, F. Cao, F. Wu, Z. Diao, J. Chen, S. Shen, L. Li, Advanced Functional Materials 28 (2018) 1706785.

[77] M.H. Lee, K. Takei, J. Zhang, R. Kapadia, M. Zheng, Y.Z. Chen, J. Nah, T.S. Matthews, Y.L. Chueh, J.W. Ager, Angewandte Chemie International Edition 51 (2012) 10760.

[78] M. Szklarczyk, J.O.M. Bockris, The Journal of Physical Chemistry 88 (1984) 5241.

[79] M. Higashi, K. Domen, R. Abe, Journal of the American Chemical Society 134 (2012) 6968.

[80] R. Abe, M. Higashi, K. Domen, Journal of the American Chemical Society 132 (2010) 11828.

[81] Y. Li, T. Takata, D. Cha, K. Takanabe, T. Minegishi, J. Kubota, K. Domen, Advanced materials 25 (2013) 125.

[82] Y. He, J.E. Thorne, C.H. Wu, P. Ma, C. Du, Q. Dong, J. Guo, D. Wang, Chem 1 (2016) 640.

[83] W. Nunn, A.K. Manjeshwar, J. Yue, A. Rajapitamahuni, T.K. Truttmann, B. Jalan, Proceedings of the National Academy of Sciences 118 (2021) e2105713118.

[84] S. Maiti, A. Pramanik, S. Mahanty, CrystEngComm 18 (2016) 450.

[85] Y.V. Kaneti, J. Moriceau, M. Liu, Y. Yuan, Q. Zakaria, X. Jiang, A. Yu, Sensors and Actuators B: Chemical 209 (2015) 889.

[86] Y.V. Kaneti, Q.M. Zakaria, Z. Zhang, C. Chen, J. Yue, M. Liu, X. Jiang, A. Yu, Journal of Materials Chemistry A 2 (2014) 13283.

[87] R.R. Salunkhe, Y.V. Kaneti, Y. Yamauchi, ACS nano 11 (2017) 5293.

[88] L.J. Murray, M. Dincă, J.R. Long, Chemical Society Reviews 38 (2009) 1294.

[89] J.-R. Li, Y. Ma, M.C. McCarthy, J. Sculley, J. Yu, H.-K. Jeong, P.B. Balbuena, H.-C. Zhou, Coordination Chemistry Reviews 255 (2011) 1791.

[90] J.Y. Kim, R. Balderas-Xicohténcatl, L. Zhang, S.G. Kang, M. Hirscher, H. Oh, H.R. Moon, Journal of the American Chemical Society 139 (2017) 15135.

[91] K. Meyer, M. Ranocchiari, J.A. van Bokhoven, Energy & Environmental Science 8 (2015) 1923.

[92] S. Wang, X. Wang, small 11 (2015) 3097.

[93] W. Wang, X. Xu, W. Zhou, Z. Shao, Advanced Science 4 (2017) 1600371.

[94] W.P. Lustig, S. Mukherjee, N.D. Rudd, A.V. Desai, J. Li, S.K. Ghosh, Chemical Society Reviews 46 (2017) 3242.

[95] D. Zhao, Y. Cui, Y. Yang, G. Qian, CrystEngComm 18 (2016) 3746.

[96] Y. Zhao, Z. Song, X. Li, Q. Sun, N. Cheng, S. Lawes, X. Sun, Energy storage materials 2 (2016) 35.

[97] H. Wang, Q.-L. Zhu, R. Zou, Q. Xu, Chem 2 (2017) 52.

[98] Z. Liang, R. Zhao, T. Qiu, R. Zou, Q. Xu, EnergyChem 1 (2019) 100001.

[99] J.W. Yoon, J.H. Kim, C. Kim, H.W. Jang, J.H. Lee, Advanced Energy Materials 11 (2021) 2003052.

[100] W. Zhang, Y. Hu, J. Ge, H.-L. Jiang, S.-H. Yu, Journal of the American Chemical Society 136 (2014) 16978.

[101] T. Zhang, W. Lin, Chemical Society Reviews 43 (2014) 5982.

[102] C. Wang, X. Liu, N.K. Demir, J.P. Chen, K. Li, Chemical Society Reviews 45 (2016) 5107.

[103] J.-S. Qin, D.-Y. Du, W. Guan, X.-J. Bo, Y.-F. Li, L.-P. Guo, Z.-M. Su, Y.-Y. Wang, Y.-Q. Lan, H.-C. Zhou, Journal of the American Chemical Society 137 (2015) 7169.

[104] S. Zhao, Y. Wang, J. Dong, C.-T. He, H. Yin, P. An, K. Zhao, X. Zhang, C. Gao, L. Zhang, Nature Energy 1 (2016) 1.

[105] Y.V. Kaneti, J. Tang, R.R. Salunkhe, X. Jiang, A. Yu, K.C.W. Wu, Y. Yamauchi, Advanced materials 29 (2017) 1604898.

[106] K.J. Lee, J.H. Lee, S. Jeoung, H.R. Moon, Accounts of chemical research 50 (2017) 2684.

[107] X. Cao, C. Tan, M. Sindoro, H. Zhang, Chemical Society Reviews 46 (2017) 2660.

[108] S. Dang, Q.-L. Zhu, Q. Xu, Nature Reviews Materials 3 (2017) 1.

[109] H.B. Wu, X.W. Lou, Science Advances 3 (2017) eaap9252.

[110] H. Luo, Z. Zeng, G. Zeng, C. Zhang, R. Xiao, D. Huang, C. Lai, M. Cheng, W. Wang, W. Xiong, Chemical Engineering Journal 383 (2020) 123196.

[111] F. Song, W. Li, Y. Sun, Inorganics 5 (2017) 40.

[112] L. Oar-Arteta, T. Wezendonk, X. Sun, F. Kapteijn, J. Gascon, Materials Chemistry Frontiers 1 (2017) 1709.

[113] B. Zhu, R. Zou, Q. Xu, Advanced Energy Materials 8 (2018) 1801193.

[114] Z. Xiu, M.H. Alfaruqi, J. Gim, J. Song, S. Kim, T.V. Thi, P.T. Duong, J.P. Baboo, V. Mathew, J. Kim, Chemical Communications 51 (2015) 12274.

[115] K. Khaletskaya, A. Pougin, R. Medishetty, C. Rosler, C. Wiktor, J. Strunk, R.A. Fischer, Chemistry of Materials 27 (2015) 7248.

[116] B. Yan, L. Zhang, Z. Tang, M. Al-Mamun, H. Zhao, X. Su, Applied Catalysis B: Environmental 218 (2017) 743.

[117] L. Shi, D. Benetti, F. Li, Q. Wei, F. Rosei, Applied Catalysis B: Environmental 263 (2020) 118317.

[118] S. Kampouri, C.P. Ireland, B. Valizadeh, E. Oveisi, P.A. Schouwink, M. Mensi, K.C. Stylianou, ACS Applied Energy Materials 1 (2018) 6541.

[119] L. Pan, T. Muhammad, L. Ma, Z.-F. Huang, S. Wang, L. Wang, J.-J. Zou, X. Zhang, Applied Catalysis B: Environmental 189 (2016) 181.

[120] X. Cao, B. Zheng, X. Rui, W. Shi, Q. Yan, H. Zhang, Angewandte chemie international edition 53 (2014) 1404.

[121] W. Li, X. Wu, N. Han, J. Chen, X. Qian, Y. Deng, W. Tang, Y. Chen, Sensors and Actuators B: Chemical 225 (2016) 158.

[122] Y. Han, M. Zhao, L. Dong, J. Feng, Y. Wang, D. Li, X. Li, Journal of Materials Chemistry A 3 (2015) 22542.

[123] Y. Wang, B. Wang, F. Xiao, Z. Huang, Y. Wang, C. Richardson, Z. Chen, L. Jiao, H. Yuan, Journal of Power Sources 298 (2015) 203.

[124] N.L. Torad, R.R. Salunkhe, Y. Li, H. Hamoudi, M. Imura, Y. Sakka, C.C. Hu, Y. Yamauchi, Chemistry–A European Journal 20 (2014) 7895.

[125] R.R. Salunkhe, J. Tang, Y. Kamachi, T. Nakato, J.H. Kim, Y. Yamauchi, ACS nano 9 (2015) 6288.

[126] L. Zhang, H.B. Wu, X.W. Lou, Journal of the American chemical society 135 (2013) 10664.

[127] J. Yao, J. Chen, K. Shen, Y. Li, Journal of Materials Chemistry A 6 (2018) 3571.

[128] W. Guo, W. Sun, L.-P. Lv, S. Kong, Y. Wang, ACS nano 11 (2017) 4198.

[129] T.K. Kim, K.J. Lee, J.Y. Cheon, J.H. Lee, S.H. Joo, H.R. Moon, Journal of the American Chemical Society 135 (2013) 8940.

[130] Z. Sun, L. Hui, W. Ran, Y. Lu, D. Jia, New Journal of Chemistry 40 (2016) 1100.

[131] S. Kong, R. Dai, H. Li, W. Sun, Y. Wang, ACS Sustainable Chemistry & Engineering 3 (2015) 1830.

[132] A. Banerjee, U. Singh, V. Aravindan, M. Srinivasan, S. Ogale, Nano Energy 2 (2013) 1158.

[133] Y. Yang, L. Sun, W. Zhan, X. Wang, X. Han, Journal of Materials Chemistry A 9 (2021) 4310.

[134] X. Gan, R. Zheng, T. Liu, J. Meng, R. Chen, X. Sun, X. Sun, Chemistry–A European Journal 23 (2017) 7264.

[135] L. Sun, Y. Zhuang, Y. Yuan, W. Zhan, X.J. Wang, X. Han, Y. Zhao, Advanced Energy Materials 9 (2019) 1902839.

[136] H. Yu, H. Fan, B. Yadian, H. Tan, W. Liu, H.H. Hng, Y. Huang, Q. Yan, ACS Applied Materials & Interfaces 7 (2015) 26751.

[137] R. Wu, X. Qian, K. Zhou, J. Wei, J. Lou, P.M. Ajayan, Acs Nano 8 (2014) 6297.

[138] J. Zhao, F. Wang, P. Su, M. Li, J. Chen, Q. Yang, C. Li, Journal of Materials Chemistry 22 (2012) 13328.

[139] W. Xia, A. Mahmood, R. Zou, Q. Xu, Energy & Environmental Science 8 (2015) 1837.

[140] D. Benetti, K.T. Dembele, J. Benavides, H. Zhao, S. Cloutier, I. Concina, A. Vomiero, F. Rosei, Journal of Materials Chemistry C 4 (2016) 3555.

[141] M. Batmunkh, M.J. Biggs, J.G. Shapter, Advanced Science 2 (2015) 1400025.

[142] J.-S. Li, S.-L. Li, Y.-J. Tang, K. Li, L. Zhou, N. Kong, Y.-Q. Lan, J.-C. Bao, Z.-H. Dai, Scientific reports 4 (2014) 1.

[143] L. Zhang, Z. Su, F. Jiang, L. Yang, J. Qian, Y. Zhou, W. Li, M. Hong, Nanoscale 6 (2014) 6590.

[144] Y. Zhang, B. Lin, Y. Sun, P. Han, J. Wang, X. Ding, X. Zhang, H. Yang, Electrochimica Acta 188 (2016) 490.

[145] X. Tong, X.T. Kong, Y. Zhou, F. Navarro-Pardo, G.S. Selopal, S. Sun, A.O. Govorov, H. Zhao, Z.M. Wang, F. Rosei, Advanced Energy Materials 8 (2018) 1701432.

[146] F. Li, M. Zhang, D. Benetti, L. Shi, L.V. Besteiro, H. Zhang, J. Liu, G.S. Selopal, S. Sun, Z. Wang, Applied Catalysis B: Environmental 280 (2021) 119402.

[147] F. Zou, Y.-M. Chen, K. Liu, Z. Yu, W. Liang, S.M. Bhaway, M. Gao, Y. Zhu, ACS nano 10 (2016) 377.

[148] W. Cho, H.J. Lee, M. Oh, Journal of the American Chemical Society 130 (2008) 16943.

[149] H.B. Yang, J. Miao, S.-F. Hung, F. Huo, H.M. Chen, B. Liu, ACS nano 8 (2014) 10403.

[150] J.H. Kim, P.W. Liang, S.T. Williams, N. Cho, C.C. Chueh, M.S. Glaz, D.S. Ginger, A.K.Y. Jen, Advanced materials 27 (2015) 695.

[151] K. Yao, F. Li, Q. He, X. Wang, Y. Jiang, H. Huang, A.K.-Y. Jen, Nano Energy 40 (2017) 155.

[152] E.S. Kim, N. Nishimura, G. Magesh, J.Y. Kim, J.-W. Jang, H. Jun, J. Kubota, K. Domen, J.S. Lee, Journal of the american chemical society 135 (2013) 5375.

[153] D. Benetti, D. Cui, H. Zhao, F. Rosei, A. Vomiero, Small 14 (2018) 1801668.

[154] D. Battaglia, J.J. Li, Y. Wang, X. Peng, Angewandte Chemie International Edition 42 (2003) 5035.

[155] J.J. Li, Y.A. Wang, W. Guo, J.C. Keay, T.D. Mishima, M.B. Johnson, X. Peng, Journal of the American Chemical Society 125 (2003) 12567.

[156] D. Battaglia, B. Blackman, X. Peng, Journal of the American Chemical Society 127 (2005) 10889.

[157] L. Jin, B. AlOtaibi, D. Benetti, S. Li, H. Zhao, Z. Mi, A. Vomiero, F. Rosei, Advanced Science 3 (2016) 1500345.

[158] H. Zhang, W. Fang, W. Wang, N. Qian, X. Ji, ACS applied materials & interfaces 11 (2019) 6927.

[159] W. Wang, W. Feng, J. Du, W. Xue, L. Zhang, L. Zhao, Y. Li, X. Zhong, Advanced Materials 30 (2018) 1705746.

[160] F. Purcell-Milton, A. Curutchet, Y. Gun'ko, Materials 12 (2019) 4089.

[161] H. Lee, M. Wang, P. Chen, D.R. Gamelin, S.M. Zakeeruddin, M. Gratzel, M.K. Nazeeruddin, Nano letters 9 (2009) 4221.

[162] A. Li, Z. Wang, H. Yin, S. Wang, P. Yan, B. Huang, X. Wang, R. Li, X. Zong, H. Han, Chemical science 7 (2016) 6076.

[163] D.O. Scanlon, C.W. Dunnill, J. Buckeridge, S.A. Shevlin, A.J. Logsdail, S.M. Woodley, C.R.A. Catlow, M. Powell, R.G. Palgrave, I.P. Parkin, Nature materials 12 (2013) 798.

[164] X. Wang, Q. Xu, M. Li, S. Shen, X. Wang, Y. Wang, Z. Feng, J. Shi, H. Han, C. Li, Angewandte Chemie International Edition 51 (2012) 13180.

[165] J. Hou, C. Yang, Z. Wang, W. Zhou, S. Jiao, H. Zhu, Applied Catalysis B: Environmental 142 (2013) 504.

[166] Z. Wang, J. Hou, C. Yang, S. Jiao, K. Huang, H. Zhu, Energy & Environmental Science 6 (2013) 2134.

[167] D. Yang, H. Liu, Z. Zheng, Y. Yuan, J.-C. Zhao, E.R. Waclawik, X. Ke, H. Zhu, Journal of the American Chemical Society 131 (2009) 17885.

[168] U. Stafford, K.A. Gray, P.V. Kamat, A. Varma, Chemical physics letters 205 (1993) 55.

[169] D.C. Hurum, A.G. Agrios, K.A. Gray, T. Rajh, M.C. Thurnauer, The Journal of Physical Chemistry B 107 (2003) 4545.

[170] S.N. Habisreutinger, L. Schmidt-Mende, J.K. Stolarczyk, Angewandte Chemie International Edition 52 (2013) 7372.

[171] X. Chen, S.S. Mao, Chemical reviews 107 (2007) 2891.

[172] B.A. Gonfa, H. Zhao, J. Li, J. Qiu, M. Saidani, S. Zhang, R. Izquierdo, N. Wu, M.A. El Khakani, D. Ma, Solar Energy Materials and Solar Cells 124 (2014) 67.

[173] J. Li, M.W. Hoffmann, H. Shen, C. Fabrega, J.D. Prades, T. Andreu, F. Hernandez-Ramirez, S. Mathur, Journal of Materials Chemistry 22 (2012) 20472.

[174] K. Baiju, A. Zachariah, S. Shukla, S. Biju, M. Reddy, K. Warrier, Catalysis letters 130 (2009) 130.

[175] J. Zhang, Q. Xu, Z. Feng, M. Li, C. Li, Angewandte Chemie 120 (2008) 1790.

[176] R.I. Bickley, T. Gonzalez-Carreno, J.S. Lees, L. Palmisano, R.J. Tilley, Journal of solid state chemistry 92 (1991) 178.

[177] T. Ohno, K. Sarukawa, K. Tokieda, M. Matsumura, Journal of Catalysis 203 (2001) 82.

[178] T. Ohno, K. Tokieda, S. Higashida, M. Matsumura, Applied Catalysis A: General 244 (2003) 383.

[179] H. Li, W. Zhang, W. Pan, Journal of the American Ceramic Society 94 (2011) 3184.

[180] Y. Gu, K. Cheng, Y.-n. Wu, Y. Wang, C. Morlay, F. Li, ACS Sustainable Chemistry & Engineering 4 (2016) 6744.

[181] J. Zheng, Y. Lyu, C. Xie, R. Wang, L. Tao, H. Wu, H. Zhou, S. Jiang, S. Wang, Advanced materials 30 (2018) 1801773.

[182] R. Adhikari, L. Jin, F. Navarro-Pardo, D. Benetti, B. AlOtaibi, S. Vanka, H. Zhao, Z. Mi, A. Vomiero, F. Rosei, Nano Energy 27 (2016) 265.

[183] W.-K. Wang, J.-J. Chen, X. Zhang, Y.-X. Huang, W.-W. Li, H.-Q. Yu, Scientific reports 6 (2016) 1.

[184] A.R. Zanatta, AIP Advances 7 (2017) 075201.

[185] J. Li, N. Wu, Catalysis Science & Technology 5 (2015) 1360.

[186] E. Garnett, P. Yang, Nano letters 10 (2010) 1082.

[187] B. Ma, P.-Y. Guan, Q.-Y. Li, M. Zhang, S.-Q. Zang, ACS applied materials & interfaces 8 (2016) 26794.

[188] N. Li, H. Huang, R. Bibi, Q. Shen, R. Ngulube, J. Zhou, M. Liu, Applied Surface Science 476 (2019) 378.

[189] M. Chandra, K. Bhunia, D. Pradhan, Inorganic Chemistry 57 (2018) 4524.

[190] H. Berger, H. Tang, F. Lévy, Journal of crystal growth 130 (1993) 108.

[191] X. Chen, C. Burda, Journal of the American Chemical Society 130 (2008) 5018.

[192] M. Sathish, B. Viswanathan, R. Viswanath, C.S. Gopinath, Chemistry of materials 17 (2005) 6349.

[193] S.S. Mali, C.A. Betty, P.N. Bhosale, P. Patil, ECS Journal of Solid State Science and Technology 1 (2012) M15.

[194] J. Du, M. Yang, F. Zhang, X. Cheng, H. Wu, H. Qin, Q. Jian, X. Lin, K. Li, D.J. Kang, Ceramics International 44 (2018) 3099.

[195] E. Talgorn, M.A. de Vries, L.D. Siebbeles, A.J. Houtepen, ACS nano 5 (2011) 3552.

[196] I. Mekis, D.V. Talapin, A. Kornowski, M. Haase, H. Weller, The Journal of Physical Chemistry B 107 (2003) 7454.

[197] D. Hurum, A. Agrios, S. Crist, K. Gray, T. Rajh, M. Thurnauer, Journal of Electron Spectroscopy and Related Phenomena 150 (2006) 155.

[198] B. Yan, Y. Zhuang, Y. Jiang, W. Xu, Y. Chen, J. Tu, X. Wang, Q. Wu, Applied Surface Science 458 (2018) 382.

[199] X. Yu, Z. Zhao, J. Zhang, W. Guo, J. Qiu, D. Li, Z. Li, X. Mou, L. Li, A. Li, Small 12 (2016) 2759.

[200] A.H. Ip, S.M. Thon, S. Hoogland, O. Voznyy, D. Zhitomirsky, R. Debnath, L. Levina, L.R. Rollny, G.H. Carey, A. Fischer, Nature nanotechnology 7 (2012) 577.

[201] J. Tang, K.W. Kemp, S. Hoogland, K.S. Jeong, H. Liu, L. Levina, M. Furukawa, X. Wang, R. Debnath, D. Cha, Nature materials 10 (2011) 765.

[202] Y. Chen, J. Vela, H. Htoon, J.L. Casson, D.J. Werder, D.A. Bussian, V.I. Klimov, J.A. Hollingsworth, Journal of the American Chemical Society 130 (2008) 5026.

[203] H. McDaniel, N. Fuke, N.S. Makarov, J.M. Pietryga, V.I. Klimov, Nature communications 4 (2013) 1.

[204] H. McDaniel, N. Fuke, J.M. Pietryga, V.I. Klimov, The journal of physical chemistry letters 4 (2013) 355.

[205] D. Wang, H. Zhao, N. Wu, M.A. El Khakani, D. Ma, The Journal of Physical Chemistry Letters 1 (2010) 1030.

[206] H. Zhao, Z. Fan, H. Liang, G. Selopal, B. Gonfa, L. Jin, A. Soudi, D. Cui, F. Enrichi, M. Natile, Nanoscale 6 (2014) 7004.

[207] Y.-F. Lin, Y.-J. Hsu, Applied Catalysis B: Environmental 130 (2013) 93.

[208] Y.-H. Chiu, K.-D. Chang, Y.-J. Hsu, Journal of Materials Chemistry A 6 (2018) 4286.

[209] K.-A. Tsai, Y.-J. Hsu, Applied Catalysis B: Environmental 164 (2015) 271.

[210] X. Tong, Y. Zhou, L. Jin, K. Basu, R. Adhikari, G.S. Selopal, H. Zhao, S. Sun, A. Vomiero, Z.M. Wang, Nano Energy 31 (2017) 441.

[211] R. Trevisan, P. Rodenas, V. Gonzalez-Pedro, C. Sima, R.S. Sanchez, E.M. Barea, I. Mora-Sero, F. Fabregat-Santiago, S. Gimenez, The journal of physical chemistry letters 4 (2013) 141.

[212] S. Hernández, D. Hidalgo, A. Sacco, A. Chiodoni, A. Lamberti, V. Cauda, E. Tresso, G. Saracco, Physical Chemistry Chemical Physics 17 (2015) 7775.

[213] T. Lopes, L. Andrade, H.A. Ribeiro, A. Mendes, international journal of hydrogen energy 35 (2010) 11601.

[214] J. Li, S.K. Cushing, P. Zheng, F. Meng, D. Chu, N. Wu, Nature communications 4 (2013) 1.

[215] D. Tafalla, P. Salvador, R. Benito, Journal of the Electrochemical Society 137 (1990) 1810.

[216] O. Khaselev, J.A. Turner, Science 280 (1998) 425.

[217] M.G. Walter, E.L. Warren, J.R. McKone, S.W. Boettcher, Q. Mi, E.A. Santori, N.S. Lewis, Chemical reviews 110 (2010) 6446.

[218] F. Sauvage, F. Di Fonzo, A. Li Bassi, C.S. Casari, V. Russo, G. Divitini, C. Ducati, C.E. Bottani, P. Comte, M. Graetzel, Nano letters 10 (2010) 2562.

[219] M. Li, W. Luo, D. Cao, X. Zhao, Z. Li, T. Yu, Z. Zou, Angewandte Chemie International Edition 52 (2013) 11016.

[220] A.B. Laursen, P.C. Vesborg, I. Chorkendorff, Chemical Communications 49 (2013) 4965.

[221] L. Tong, A. Iwase, A. Nattestad, U. Bach, M. Weidelener, G. Götz, A. Mishra, P. Bäuerle, R. Amal, G.G. Wallace, Energy & Environmental Science 5 (2012) 9472.

[222] K. Fan, F. Li, L. Wang, Q. Daniel, E. Gabrielsson, L. Sun, Physical Chemistry Chemical Physics 16 (2014) 25234.

[223] K.S. Leschkies, R. Divakar, J. Basu, E. Enache-Pommer, J.E. Boercker, C.B. Carter, U.R. Kortshagen, D.J. Norris, E.S. Aydil, Nano letters 7 (2007) 1793.

[224] A. Kay, I. Cesar, M. Grätzel, Journal of the American Chemical Society 128 (2006) 15714.

[225] T.J. Jacobsson, V. Fjällström, M. Edoff, T. Edvinsson, Solar Energy Materials and Solar Cells 134 (2015) 185.

[226] Q. Yu, X. Meng, T. Wang, P. Li, L. Liu, K. Chang, G. Liu, J. Ye, Chemical communications 51 (2015) 3630.

[227] U.A. Joshi, P.A. Maggard, The journal of physical chemistry letters 3 (2012) 1577.

[228] H.L. Wu, X.B. Li, C.H. Tung, L.Z. Wu, Advanced Science 5 (2018) 1700684.

[229] P. Meng, M. Wang, Y. Yang, S. Zhang, L. Sun, Journal of Materials Chemistry A 3 (2015) 18852.

[230] Z. Ji, M. He, Z. Huang, U. Ozkan, Y. Wu, Journal of the American Chemical Society 135 (2013) 11696.

[231] H. Lv, C. Wang, G. Li, R. Burke, T.D. Krauss, Y. Gao, R. Eisenberg, Proceedings of the National Academy of Sciences 114 (2017) 11297.

[232] K. Zheng, K. Zidek, M. Abdellah, W. Zhang, P. Chábera, N. Lenngren, A. Yartsev, T.n. Pullerits, The Journal of Physical Chemistry C 118 (2014) 18462.

[233] F. Safari-Alamuti, J.R. Jennings, M.A. Hossain, L.Y.L. Yung, Q. Wang, Physical Chemistry Chemical Physics 15 (2013) 4767.

[234] A. Renaud, B. Chavillon, L. Cario, L.c.L. Pleux, N. Szuwarski, Y. Pellegrin, E. Blart, E. Gautron, F. Odobel, S. Jobic, The Journal of Physical Chemistry C 117 (2013) 22478.

[235] Y. Zhang, Z. Guo, Chemical communications 50 (2014) 3443.

[236] P. Zhang, X.W. Lou, Advanced Materials 31 (2019) 1900281.

[237] M. Xiao, Z. Wang, M. Lyu, B. Luo, S. Wang, G. Liu, H.M. Cheng, L. Wang, Advanced Materials 31 (2019) 1801369.

[238] G. Prieto, H. Tüysüz, N. Duyckaerts, J. Knossalla, G.-H. Wang, F. Schüth, Chemical reviews 116 (2016) 14056.

[239] X. Wang, J. Feng, Y. Bai, Q. Zhang, Y. Yin, Chemical reviews 116 (2016) 10983.

[240] Z. Zhao, Q. Chen, C. Hu, S. Huang, Y. Wang, Journal of Alloys and Compounds 485 (2009) 627.

[241] I. Pastoriza-Santos, L.M. Liz-Marzán, Langmuir 18 (2002) 2888.

[242] Y. Liu, Y. Zhao, H. Luo, Z. Wu, Z. Zhang, Journal of Nanoparticle Research 13 (2011) 2041.

[243] D.M. Goodgame, D.J. Williams, R.E. Winpenny, Angewandte Chemie International Edition in English 27 (1988) 261.

[244] L. Besra, M. Liu, Progress in materials science 52 (2007) 1.

[245] W. Guo, W. Sun, Y. Wang, ACS nano 9 (2015) 11462.

[246] L.-N. Jin, Q. Liu, W.-Y. Sun, Chinese Chemical Letters 24 (2013) 663.

[247] C. Liao, J. Zhao, B. Tang, A. Tang, Y. Sun, J. Xu, Journal of New Materials for Electrochemical Systems 15 (2012) 79.

[248] D. Xie, W. Yuan, Z. Dong, Q. Su, J. Zhang, G. Du, Electrochimica Acta 92 (2013) 87.

[249] K.S. Sing, Pure and applied chemistry 57 (1985) 603.

[250] T. Zhou, Z. Cao, P. Zhang, H. Ma, Z. Gao, H. Wang, Y. Lu, J. He, Y. Zhao, Scientific reports 7 (2017) 1.

[251] G. Zhou, D.-W. Wang, L.-C. Yin, N. Li, F. Li, H.-M. Cheng, ACS nano 6 (2012) 3214.

[252] W. Liu, C. Lu, X. Wang, K. Liang, B.K. Tay, Journal of Materials Chemistry A 3 (2015) 624.

[253] D.T. Dam, X. Wang, J.-M. Lee, ACS applied materials & interfaces 6 (2014) 8246.

[254] Y. Zhu, H. Guo, Y. Wu, C. Cao, S. Tao, Z. Wu, Journal of Materials Chemistry A 2 (2014) 7904.

[255] P. Dubey, N. Kaurav, R.S. Devan, G. Okram, Y. Kuo, RSC advances 8 (2018) 5882.

[256] M.A. Peck, M.A. Langell, Chemistry of Materials 24 (2012) 4483.

[257] W. Huang, C. Harnagea, X. Tong, D. Benetti, S. Sun, M. Chaker, F. Rosei, R. Nechache, ACS applied materials & interfaces 11 (2019) 13185.

[258] M. Batmunkh, M.J. Biggs, J.G. Shapter, Small 11 (2015) 2963.

[259] S. Zhang, H. Niu, Y. Lan, C. Cheng, J. Xu, X. Wang, The Journal of Physical Chemistry C 115 (2011) 22025.

[260] M.A. Park, S.Y. Lee, J.H. Kim, S.H. Kang, H. Kim, C.J. Choi, K.S. Ahn, physica status solidi (a) 211 (2014) 1868.

[261] Y. Dong, Y. Chen, P. Jiang, G. Wang, X. Wu, R. Wu, C. Zhang, Chem. - Asian J. 10 (2015) 1660.

[262] Y. Dong, Y. Chen, P. Jiang, G. Wang, X. Wu, R. Wu, C. Zhang, Chemistry–An Asian Journal 10 (2015) 1660.

[263] Y. Dong, R. Wu, P. Jiang, G. Wang, Y. Chen, X. Wu, C. Zhang, ACS Sustainable Chemistry & Engineering 3 (2015) 2429.

[264] Y. Na, B. Hu, Q.-L. Yang, J. Liu, L. Zhou, R.-Q. Fan, Y.-L. Yang, Chinese Chemical Letters 26 (2015) 141.

[265] B. Liu, X.-B. Li, Y.-J. Gao, Z.-J. Li, Q.-Y. Meng, C.-H. Tung, L.-Z. Wu, Energy & Environmental Science 8 (2015) 1443.

[266] E. Giannoudis, S. Bold, C. Müller, A. Schwab, J. Bruhnke, N. Queyriaux, C. Gablin, D. Léonard, C. Saint-Pierre, D. Gasparutto, ACS Applied Materials & Interfaces 13 (2021) 49802.

[267] C. Lu, A. Drichel, J. Chen, F. Enders, A. Rokicińska, P. Kuśtrowski, R. Dronskowski, K. Boldt, A. Slabon, Nanoscale 13 (2021) 869.

[268] X. Su, Y. Chen, L. Ren, Y. He, X. Yin, Y. Liu, W. Yang, ACS Sustainable Chemistry & Engineering 7 (2019) 11166.

[269] J. Massin, S. Lyu, M. Pavone, A.B. Muñoz-García, B. Kauffmann, T. Toupance, M. Chavarot-Kerlidou, V. Artero, C. Olivier, Dalton Transactions 45 (2016) 12539.

[270] D.A. Hoogeveen, M. Fournier, S.A. Bonke, X.-Y. Fang, A.J. Mozer, A. Mishra, P. Bäuerle, A.N. Simonov, L. Spiccia, Electrochimica Acta 219 (2016) 773.

[271] R.J. Kamire, M.B. Majewski, W.L. Hoffeditz, B.T. Phelan, O.K. Farha, J.T. Hupp, M.R. Wasielewski, Chemical science 8 (2017) 541.

[272] M.A. Gross, C.E. Creissen, K.L. Orchard, E. Reisner, Chemical science 7 (2016) 5537.

[273] S. Malato, P. Fernández-Ibáñez, M.I. Maldonado, J. Blanco, W. Gernjak, Catalysis today 147 (2009) 1.

[274] R. Hardman, Environmental health perspectives 114 (2006) 165.

[275] X. Liu, B. Luo, J. Liu, D. Jing, D. Benetti, F. Rosei, Journal of Materials Chemistry A 8 (2020) 1787.

[276] G. Wang, Y. Ling, H. Wang, X. Yang, C. Wang, J.Z. Zhang, Y. Li, Energy & Environmental Science 5 (2012) 6180.

[277] G. Wang, Y. Yang, Y. Ling, H. Wang, X. Lu, Y.-C. Pu, J.Z. Zhang, Y. Tong, Y. Li, Journal of Materials Chemistry A 4 (2016) 2849.

[278] M. Forster, R.J. Potter, Y. Ling, Y. Yang, D.R. Klug, Y. Li, A.J. Cowan, Chemical science 6 (2015) 4009.

[279] Y. Ling, G. Wang, J. Reddy, C. Wang, J.Z. Zhang, Y. Li, Angewandte Chemie 124 (2012) 4150.

[280] H. Li, C. Chen, X. Huang, Y. Leng, M. Hou, X. Xiao, J. Bao, J. You, W. Zhang, Y. Wang, Journal of Power Sources 247 (2014) 915.

[281] E. Cao, G. Song, Z. Guo, Y. Zhang, W. Hao, L. Sun, Z. Nie, Materials Letters 261 (2020) 126985.

[282] H. Xu, H. Chen, S. Chen, K. Wang, X. Wang, International Journal of Hydrogen Energy 46 (2021) 32445.

[283] X. Zhang, Y. Liu, Z. Kang, ACS applied materials & interfaces 6 (2014) 4480.

[284] T. Zhou, J. Wang, S. Chen, J. Bai, J. Li, Y. Zhang, L. Li, L. Xia, M. Rahim, Q. Xu, Applied Catalysis B: Environmental 267 (2020) 118599.

[285] M. Kibria, F. Chowdhury, S. Zhao, B. AlOtaibi, M. Trudeau, H. Guo, Z. Mi, Nature communications 6 (2015) 1.

[286] J.L. Young, K.X. Steirer, M.J. Dzara, J.A. Turner, T.G. Deutsch, Journal of Materials Chemistry A 4 (2016) 2831.

[287] Z. Lin, J. Xiao, L. Li, P. Liu, C. Wang, G. Yang, Advanced Energy Materials 6 (2016) 1501865.

[288] J.F. de Brito, F. Tavella, C. Genovese, C. Ampelli, M.V.B. Zanoni, G. Centi, S. Perathoner, Applied Catalysis B: Environmental 224 (2018) 136.

[289] S. Velmurugan, T.C.-K. Yang, J.-N. Chen, L. Zhi-Xiang, Microchimica Acta 188 (2021) 1.

[290] X. Liang, T.-H. Kim, J.-W. Yoon, C.-H. Kwak, J.-H. Lee, Sensors and actuators B: chemical 209 (2015) 934.

[291] H. Zhang, L.V. Besteiro, J. Liu, C. Wang, G.S. Selopal, Z. Chen, D. Barba, Z.M. Wang, H. Zhao, G.P. Lopinski, Nano Energy 79 (2021) 105416.

[292] G.S. Selopal, M. Mohammadnezhad, F. Navarro-Pardo, F. Vidal, H. Zhao, Z.M. Wang, F. Rosei, Nanoscale Horizons 4 (2019) 404.

[293] K.T. Dembele, G.S. Selopal, R. Milan, C. Trudeau, D. Benetti, A. Soudi, M.M. Natile, G. Sberveglieri, S. Cloutier, I. Concina, Journal of Materials Chemistry A 3 (2015) 2580.

[294] Z. Yin, S. Wu, X. Zhou, X. Huang, Q. Zhang, F. Boey, H. Zhang, small 6 (2010) 307.

[295] X. Meng, C. Yu, X. Song, Y. Liu, S. Liang, Z. Liu, C. Hao, J. Qiu, Advanced Energy Materials 5 (2015) 1500180.

[296] N. Mohanty, D. Moore, Z. Xu, T. Sreeprasad, A. Nagaraja, A.A. Rodriguez, V. Berry, Nature communications 3 (2012) 1.

[297] R. Akilimali, G.S. Selopal, M. Mohammadnezhad, I. Ka, Z.M. Wang, G.P. Lopinski, H. Zhao, F. Rosei, Chemical Engineering Journal 435 (2022) 135037.

[298] X. Peng, L. Manna, W. Yang, J. Wickham, E. Scher, A. Kadavanich, A.P. Alivisatos, Nature 404 (2000) 59.

[299] L. Manna, D.J. Milliron, A. Meisel, E.C. Scher, A.P. Alivisatos, Nature materials 2 (2003) 382.

[300] E.V. Anokhina, M. Vougo-Zanda, X. Wang, A.J. Jacobson, Journal of the American Chemical Society 127 (2005) 15000.

[301] W. Guo, X. Sun, C. Chen, D. Yang, L. Lu, Y. Yang, B. Han, Green Chemistry 21 (2019) 503.

[302] N. Bouazizi, R. Bargougui, A. Oueslati, R. Benslama, Adv. Mater. Lett 6 (2015) 158.

[303] Y. Yang, D. Xu, Q. Wu, P. Diao, Scientific reports 6 (2016) 1.

[304] M.E. Aguirre, R. Zhou, A.J. Eugene, M.I. Guzman, M.A. Grela, Applied Catalysis B: Environmental 217 (2017) 485.

[305] E. Kraut, R. Grant, J. Waldrop, S. Kowalczyk, Physical Review Letters 44 (1980) 1620.

[306] B. Sharma, R. Purohit, Semiconductor heterojunctions, Elsevier, 2015.

[307] G.M. Kumar, A.M. Kumar, P. Ilanchezhiyan, T. Kang, Nanoscale 6 (2014) 11226.

[308] W. Wang, Z. Zeng, G. Zeng, C. Zhang, R. Xiao, C. Zhou, W. Xiong, Y. Yang, L. Lei, Y. Liu, Chemical Engineering Journal 378 (2019) 122132.

[309] S. Li, J. Pan, H. Li, Y. Liu, W. Ou, J. Wang, C. Song, W. Zhao, Y. Zheng, C. Li, Chemical Engineering Journal 366 (2019) 305.

[310] S. Jovanović, T. Da Ross, A. Ostric, D. Tošić, J. Prekodravac, Z. Marković, B.T. Marković, Physica Scripta 2014 (2014) 014023.

[311] H. Yang, J. Tian, Y. Bo, Y. Zhou, X. Wang, H. Cui, Journal of Colloid and Interface Science 487 (2017) 258.

[312] L. Wei, J. Zhang, M. Ruan, Applied Surface Science 541 (2021) 148431.

[313] L. Wu, S. Ma, J. Li, X. Li, Thin Solid Films 724 (2021) 138600.

[314] F.-Y. Su, W.-D. Zhang, Materials Letters 211 (2018) 65.

[315] R. Li, L. Sun, W. Zhan, Y.-A. Li, X. Wang, X. Han, Journal of Materials Chemistry A 6 (2018) 15747.

[316] H. Sohrabi, S. Javanbakht, F. Oroojalian, F. Rouhani, A. Shaabani, M.R. Majidi, M. Hashemzaei, Y. Hanifehpour, A. Mokhtarzadeh, A. Morsali, Chemosphere 281 (2021) 130717.

SOMMAIRE RÉCAPITULATIF

L’introduction

En raison de l'utilisation excessive des combustibles fossiles, des problèmes environnementaux toujours plus nombreux et de la croissance démographique mondiale, la recherche de sources d'énergie vertes et renouvelables est impérative et urgente. L'énergie solaire est apparue comme une alternative prometteuse aux combustibles fossiles limités et son utilisation efficace est tout aussi attrayante, mais aussi un défi. Le fractionnement de l'eau par voie photoélectrochimique (PEC), qui permet de récolter et de convertir directement l'énergie solaire en hydrogène (H_2), est une approche idéale pour répondre aux problèmes énergétiques et environnementaux mondiaux. Dans ce processus, l'énergie transmise par le rayonnement solaire est stockée dans les liaisons chimiques de l'hydrogène diatomique avec l'eau comme seule émission ou comme réactif. Étant donné que l'efficacité des systèmes PEC dépend principalement de l'activité photocatalytique des matériaux d'électrode, il est essentiel de concevoir des photocatalyseurs stables à long terme, peu coûteux et très performants. L'article présente ensuite les principes de fonctionnement de la séparation de l'eau par PEC ainsi que les exigences et les défis actuels des photocatalyseurs.

Le photoélectrode semi-conducteur d'une cellule de fractionnement de l'eau PEC doit permettre l'absorption de la lumière, la séparation des charges, la migration et le transfert vers la solution électrolytique pour les réactions d'oxydoréduction. Parmi les semi-conducteurs couramment utilisés pour la photoélectrode, l'oxyde métallique (MO) est souvent considéré comme la catégorie de matériaux adaptée à la séparation de l'eau solaire. Cependant, certains d'entre eux ne présentent pas de très bonnes propriétés semi-conductrices, comme la mobilité des porteurs, par rapport aux semi-conducteurs III-V ou même au Si. Le défi est alors de surmonter ces limitations tout en profitant des propriétés du MO. Cependant, les méthodes traditionnelles de synthèse de ces MO sont principalement produites par voie chimique humide, ce qui implique des processus complexes et nécessite une température de réaction élevée. De plus, les MO synthétisés par les techniques conventionnelles sont insuffisants pour synthétiser des matériaux ayant les propriétés de séparation de l'eau souhaitées. Par conséquent, il serait hautement souhaitable de développer une procédure simple de synthèse de MO qui satisfasse à toutes les exigences.

Au cours des deux dernières décennies, les cadres métallo-organiques (MOF), un nouveau type de matériaux hybrides inorganiques-organiques et cristallins de haute porosité, ont suscité un vif intérêt académique. Outre l'utilisation directe, la transformation thermique des MOF crée une variété de matériaux nanostructurés beaucoup plus stables et conducteurs, notamment des matériaux à base de carbone, des MO, des chalcogénures métalliques, des phosphures métalliques et des carbures métalliques. La méthode de

synthèse par modèle de MOF offre une méthode alternative pour préparer des MO diversifiés qui présente de nombreux avantages par rapport aux méthodes de synthèse chimique et physique traditionnelles. En outre, en raison de l'effet synergique entre les différents composants, les composites de MO mixtes dérivés de MOF possèdent généralement des propriétés améliorées par rapport à leurs homologues individuels.

Objectif de la thèse

A ce jour, même si de nombreuses nanostructures de MOF ont été dérivées avec succès, leurs applications dans la séparation solaire de l'eau sont encore limitées. Ainsi, les objectifs de cette thèse sont les suivants :

(1) Synthétiser une phase mixte anatase/rutile TiO_2 par MOF-template, l'existence à l'intérieur de cette jonction de phase dans la photoanode offrira un meilleur alignement de bande électronique favorable et un transfert de charge plus rapide.

(2) L'introduction de matériaux carbonés à l'intérieur de la photocathode à base de NiO par le biais d'un modèle de MOF, ce qui permettra de surmonter tous les inconvénients de la photocathode NiO traditionnelle, et la présence de matériaux carbonés favorise un transfert de charge rapide.

(3) Utilisation d'une structure MOF sur MOF pour construire une photoanode nanocomposite à jonction p-n afin d'utiliser plus efficacement l'énergie solaire pour produire de l'hydrogène, sans aucune sensibilisation.

Section expérimentale

Le chapitre 2 fournit les détails expérimentaux. Les méthodes de synthèse de tous les échantillons de MOF et de MO connexes, les informations de caractérisation, le test PEC et la production de H_2. Tous les dispositifs sont également décrits dans ce chapitre.

Résultats et discussions

Le chapitre 3 correspond à mon premier projet. Un TiO_2 à phase mixte anatase/rutile avec une structure octaédrique a été subtilement conçu et synthétisé en utilisant un MOF comme modèle sacrificiel. Après sensibilisation avec des points quantiques, la performance PEC de la photoanode TiO_2 dérivée du MOF est systématiquement étudiée. La publication liée à ce chapitre est :

L. Shi, D. Benetti, F. Li, Q. Wei, F. Rosei, Phase-junction design of MOF-derived TiO_2 photoanodes sensitized with Quantum Dots for efficient hydrogen generation. Applied Catalysis B: Environmental, 263 (2020) 118317.

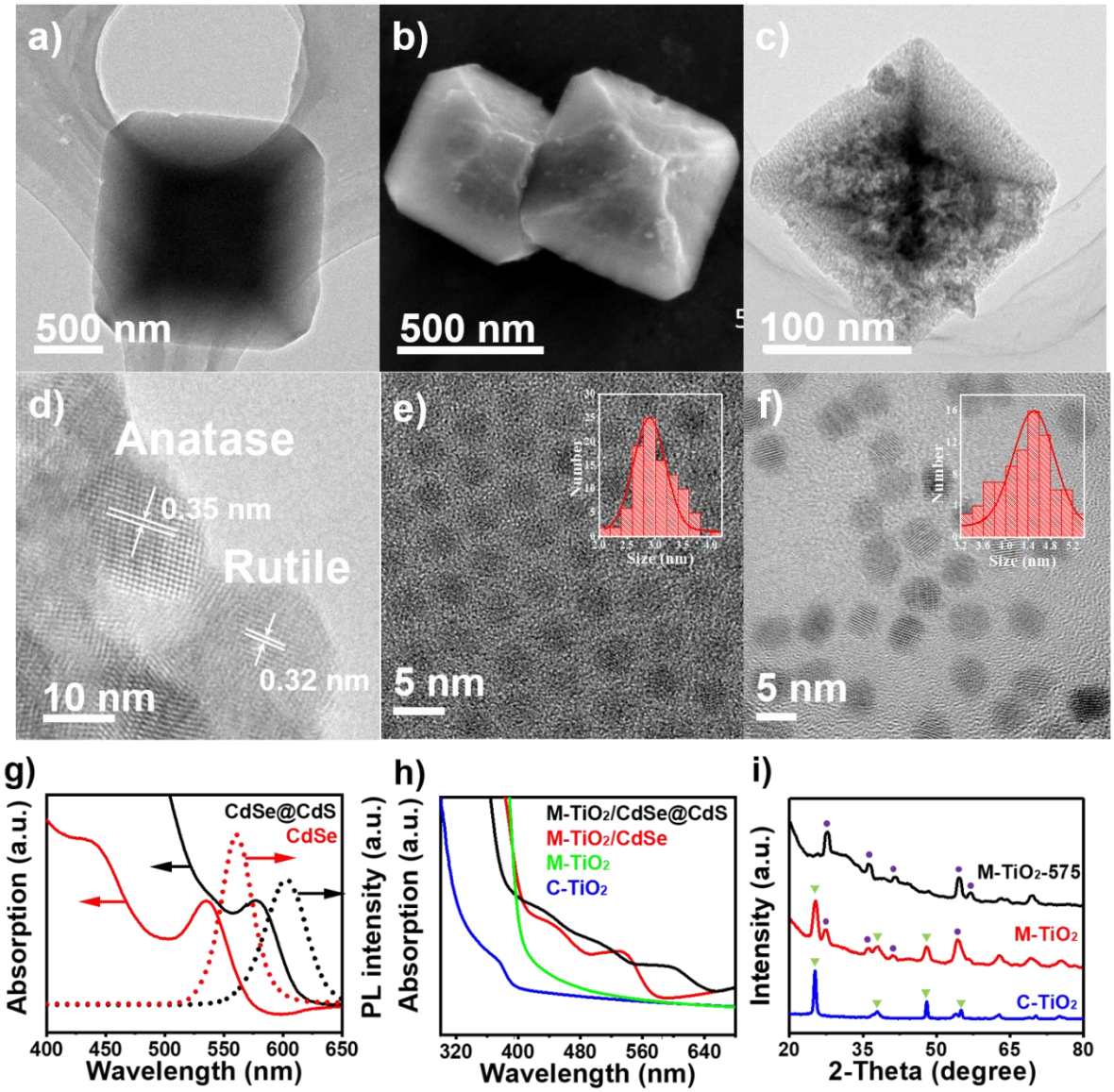

Figure R1 Image TEM du précurseur NH_2-MIL-125(Ti) (a); Images SEM (b) et TEM (c) de M-TiO_2 et image HRTEM de M-TiO_2 (d). (e) Image TEM de CdSe. L'image en médaillon montre la taille moyenne de CdSe; (f) Image TEM de CdSe@CdS. L'image en médaillon montre la taille moyenne du CdSe@CdS. (g) Adsorption UV et intensité PL de CdSe et CdSe@CdS. (h) Spectres DRS-UV de C-TiO_2, M-TiO_2, M-TiO_2/CdSe et M-TiO_2/CdSe@CdS. (i) le M-TiO_2 (rouge), le C-TiO_2 (bleu) et le M-TiO_2-575 (noir) (triangle vert: TiO_2 en phase anatase; point violet: TiO_2 en phase rutile).

Nous avons synthétisé NH_2-MIL-125(Ti) et l'avons utilisé comme précurseur sacrificiel et modèle idéal pour synthétiser les jonctions de phase anatase-rutile du TiO_2 (M-TiO_2). Le M-TiO_2 à phase mixte anatase et rutile a été obtenu par le contrôle de la décomposition thermique de NH_2-MIL-125(Ti) à 500 °C dans l'air. La figure R1 montre les images TEM du MO et des QDs, les spectres UV et DRS, et les schémas XRD

des échantillons préparés. Tous les résultats montrent que la jonction de phase anatase-rutile a été construite avec succès.

L'activité PEC des différentes photoanodes M-TiO_2 et TiO_2 commercial (C-TiO_2) sensibilisées par les QDs a été testée, comme le montre la Figure R2. En particulier, la densité de photocourant saturée la plus élevée du système PEC basé sur la photoanode M-TiO_2/CdSe était de 7,55 mA/cm^2 (à 0,9 V contre RHE), ce qui était environ 10% plus élevé que la photoanode C-TiO_2/CdSe (6,87 mA/cm^2). En utilisant les QDs core-shell, la photoanode M-TiO_2/CdSe@CdS a atteint 10,72 mA/cm^2 dans les mêmes conditions, soit une amélioration de 47,6% par rapport à la photoanode C-TiO_2/CdSe@CdS (7,24 mA/cm^2). La densité de courant n'était que de 5,26 mA/cm^2, valeur inférieure à celle du M-TiO_2 et du C-TiO_2. La raison, comme indiqué ailleurs, est que le rutile en phase pure est normalement inactif pour les photocatalyseurs en raison des taux de recombinaison rapides. En utilisant le substrat M-TiO_2, une densité de courant plus élevée peut être obtenue.

Un autre aspect important pour les dispositifs PEC est leur stabilité à long terme. La stabilité des dispositifs PEC à photo-anodes de TiO_2 sensibilisées par des QDs (photocourant par rapport à l'évolution dans le temps) a été mesurée à 0,4 V par rapport à RHE sous une illumination solaire AM 1,5 G (100 mW/cm^2) (Figure R2). Pour mieux visualiser les tendances de décroissance, les densités de photocourant des photoanodes ont été normalisées à leurs valeurs maximales. Le *J* des deux photoanodes C-TiO_2 sensibilisées par des QDs décroît rapidement en 180 s, ne conservant qu'environ 70% des valeurs initiales. Pour C-TiO_2/CdSe, le taux de décroissance était très rapide, ne conservant que 42,07% de sa valeur initiale après 7200 s. Pour le C-TiO_2/CdSe@CdS, le J a atteint une valeur assez stable après 3600 s, ne conservant que 57,5% de sa valeur initiale après 2 h.

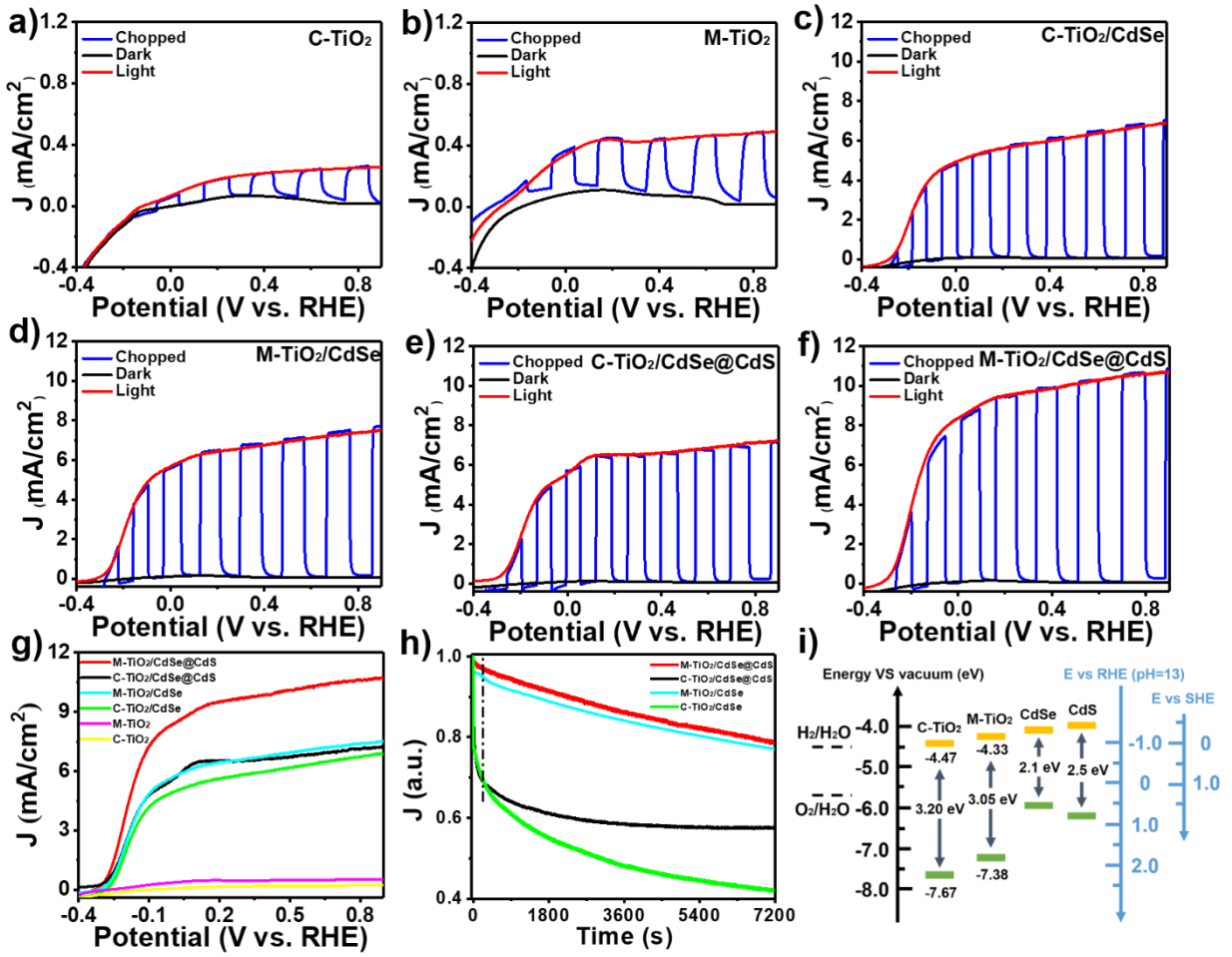

Figure R2 Performance PEC de tous les échantillons dans l'obscurité, sous illumination continue et sous illumination hachée. (a) C-TiO_2; (b) M-TiO_2; (c) C-TiO_2/CdSe(d) M-TiO_2/CdSe(e) C-TiO_2/CdSe@CdS et (f) M-TiO_2/CdSe@CdS. (g) Dépendance de la densité du photocourant par rapport au potentiel de M-TiO_2 et C-TiO_2 sensibilisés par CdSe et CdSe@CdS. (h) Mesures de stabilité (densité du photocourant en fonction du temps) de M-TiO_2 et C-TiO_2 sensibilisés par des photoanodes CdSe et CdSe@CdS à 0,4 V en fonction de RHE sous un éclairage AM 1,5 G (100 mW/cm^2). (i) Résumé des niveaux d'énergie obtenus à partir des mesures UPS. Les niveaux d'énergie du CdSe et du CdS.

La raison pourrait être attribuée à un effet synergique : (i) Bénéficiant de l'alignement favorable de la bande électronique des M-TiO_2/QDs, un plus grand nombre d'électrons et de trous peuvent être extraits des QDs vers le M-TiO_2, contribuant ainsi à la densité de courant. En raison de l'efficacité du transfert d'électrons, l'accumulation d'électrons et l'oxydation ont été largement supprimées. (ii) Selon l'analyse de la dynamique des charges, avec l'existence d'une phase mixte de TiO_2, la séparation spatiale des électrons et des trous augmente, ce qui réduit davantage les effets de recombinaison (Figure R3). Ces résultats fournissent des informations fondamentales sur l'importance du contrôle de l'alignement de la bande du métal oxyde semi-conducteur. En particulier, les orientations futures pour les cellules PEC basées sur des QDs colloïdaux

peuvent se concentrer sur le contrôle de la séparation des charges photogénérées en introduisant une jonction de phase dans un semi-conducteur polymorphe, tel que le TiO_2, afin d'améliorer leurs performances et leur stabilité.

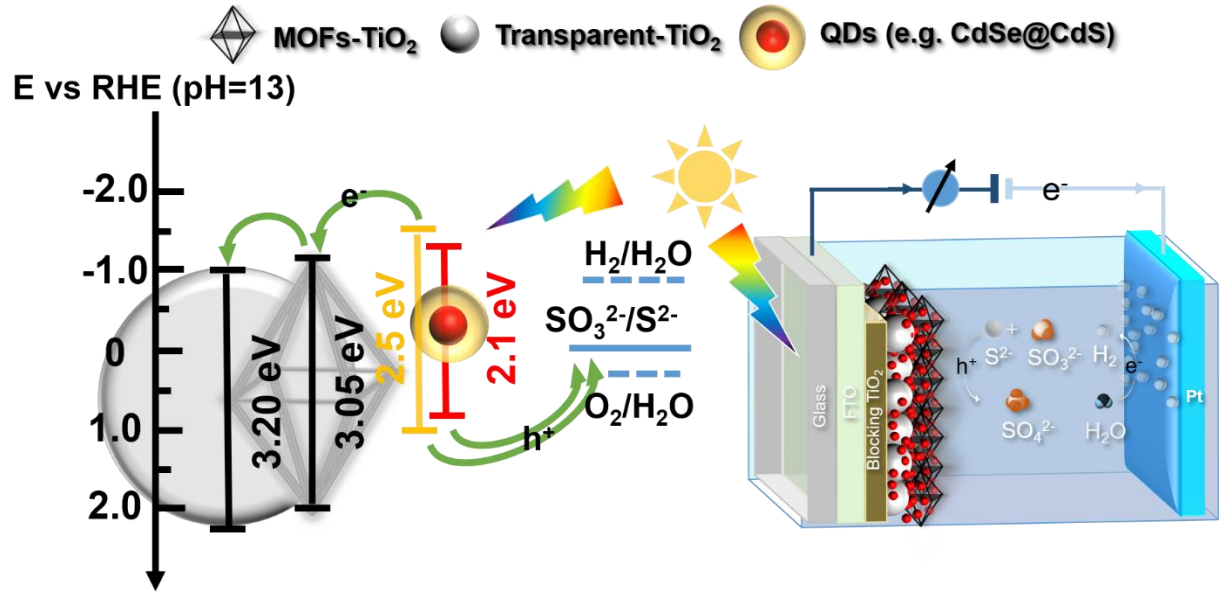

Figure R3 Alignement des bandes et schéma de la cellule PEC.

Le chapitre 4 correspond à mon deuxième projet. Un MOFs à base de nickel a été utilisé comme précurseur pour synthétiser une photocathode nanohybride NiO/carbone à structure de boule creuse. Après sensibilisation avec des points quantiques, la performance PEC de ces photocathodes a été étudiée à pH neutre et sans aucun réactif sacrificiel, cocatalyseur ou lieur moléculaire. La publication liée à ce chapitre est :

L. Shi, D. Benetti, F. Li, Q. Wei, F. Rosei, Design of MOF-Derived NiO/carbon Nanohybrids Photocathodes Sensitized with Quantum Dots for Solar Hydrogen Production. *Small*, (2022) 2201815.

Une photocathode hybride NiO/carbone à structure de boule creuse a été synthétisée par la méthode du modèle MOF. Cette approche peut nous aider à surmonter les inconvénients du NiO synthétisé par des méthodes de synthèse traditionnelles, tels que la faible diffusion des trous, la mauvaise conductivité électrique et la faible surface spécifique. De plus, l'incorporation d'allotropes de carbone facilite le transfert de charge à l'intérieur de la photocathode NiO/C. Après sensibilisation avec des QDs CdSe@CdS core@shell par la méthode SILAR, le dispositif optimisé a présenté une meilleure performance PEC et une meilleure stabilité par rapport au NiO nu (Figure R4).

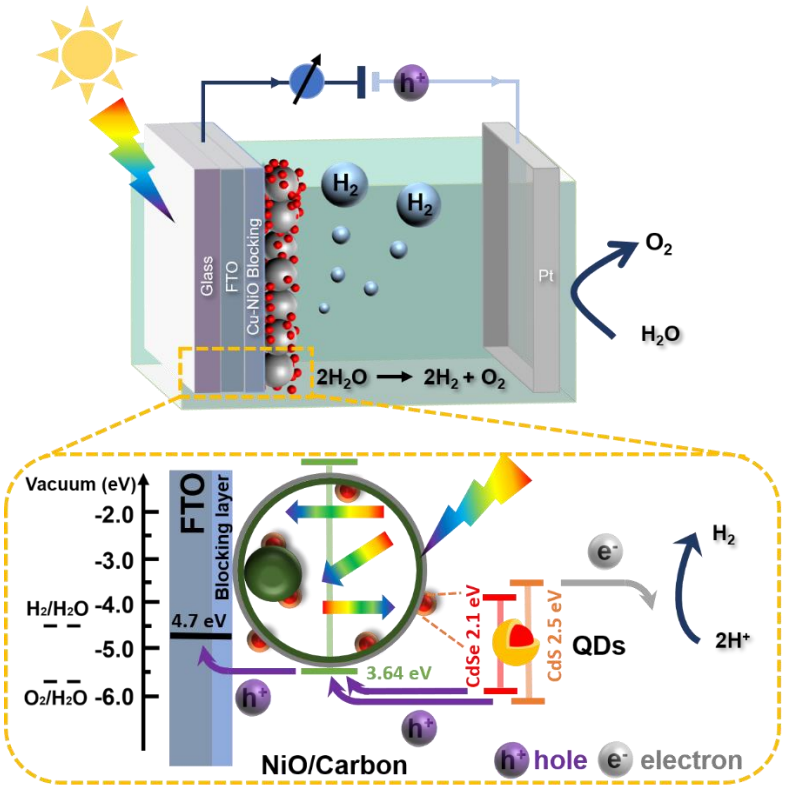

Figure R4 Illustration schématique de la photocathode NiO/C assemblée dans un montage PEC et de la migration des excitons photogénérés aux interfaces.

Comme le montre la figure R5a, le Ni-MOF présente une morphologie sphérique avec une surface lisse et des diamètres moyens autour de 1-2 µm. Après la première étape de calcination dans une atmosphère inerte, la surface est devenue rugueuse après la pyrolyse, mais aucun changement de morphologie n'a été détecté (Figure R5b et Figure R5c). Dans la deuxième étape, un recuit est effectué à l'air pour oxyder le nickel métallique. Le composite NiO/C résultant hérite de la morphologie du Ni-MOF et révèle une structure creuse hiérarchique. La SAED (Figure R5d) montre un groupe d'anneaux de diffraction qui sont indexés aux (111), (200) et (220) du NiO, ce qui correspond aux espacements d de 2,4 Å et 2,1 Å du NiO (Figure R5e). La figure R5f indique les distributions relativement uniformes des éléments de nickel, d'oxygène et de carbone qui semblent plus concentrés dans l'enveloppe extérieure de la structure creuse. L'analyse du spectre XRD (Figure R5g et h) confirme que tous les Ni/C se convertissent en NiO/C. La TGA peut également estimer la teneur finale en carbone du NiO/C ; dans nos échantillons, elle s'est avérée être d'environ 2% en poids (Figure R5i). Analyse Raman (encart dans la Figure R5i) réalisée sur l'échantillon de NiO/C. Les pics caractéristiques du carbone autour de 1136 et 1387 cm^{-1} sont clairement visibles. La plus faible intensité des pics dans NiO/C suggère une plus faible quantité de carbone dans l'échantillon.

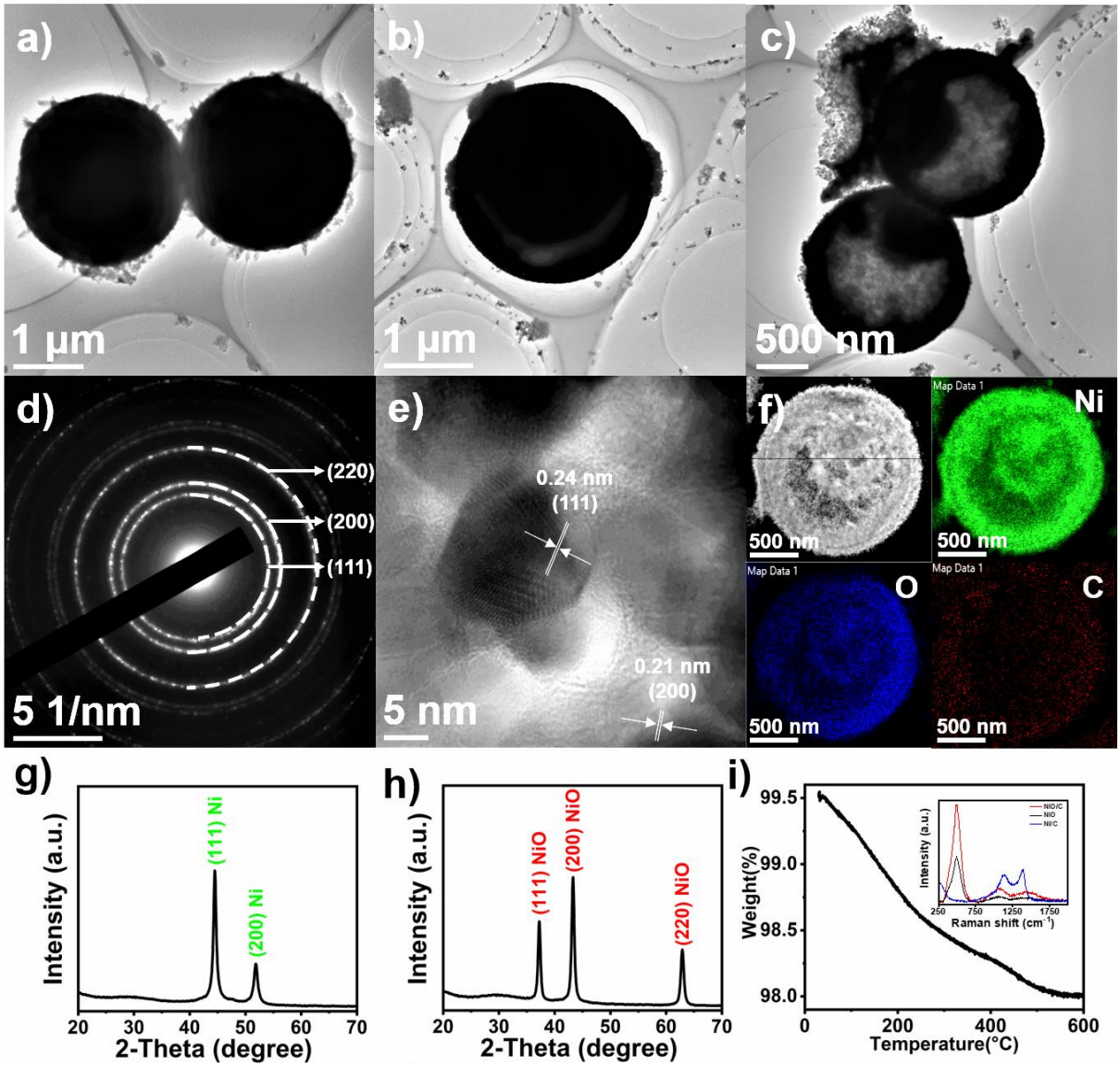

Figure R5 Images TEM des précurseurs Ni-MOF (a), Ni/C (b), et NiO/C (c). (d) Modèle SAED de NiO/C. (e) Image HRTEM de NiO/C. (f) Image STEM, nickel, oxygène et carbone. Diagrammes XRD de (g) Ni/C et (h) NiO/C. Résultats TGA de NiO/C (i). Spectres Raman de NiO purs, Ni/C et NiO/C (insérer la figure i).

Comparé à la Figure R6a et b, le résultat montre que la présence de la couche de blocage peut réduire l'accumulation de charges aux interfaces et ainsi permettre une réponse transitoire plus rapide. Pour étendre davantage la réponse spectrale de la photocathode, des CdSe/CdS QDs core@shell ont été déposés sur NiO/C. Pour une comparaison équitable, des NiO/C/CdS QDs ont également été préparés. Comme on peut le voir sur la figure R6c, le photocourant à 0 V en fonction de la RHE de NiO/C/CdSe@CdS (-93,59 µA/cm^2) est nettement supérieur à ceux obtenus avec seulement du CdSe (-51,87 µA/cm^2) ou des CdS QDs (-27,63 µA/cm^2) (Figure R6d), atteignant un maximum de -285 µA cm^{-2} à -0,4 V en fonction de la RHE.

En employant les QDs cœur-coquille (CdSe@CdS), une amélioration maximale de +225% du photocourant peut être obtenue par rapport aux QDs cœur (CdSe). De plus, afin d'observer l'influence de la présence de carbone sur les propriétés de la photocathode, les mêmes expériences ont également été réalisées en utilisant comme référence une photocathode à base de film de NiO pur préparée à l'aide d'une technique similaire à celle du MOF. Lorsque le film de NiO pur a été sensibilisé avec des QDs de CdSe, le J_{ph} n'était que de -13,97 µA/cm^2 (figure R6e). Ainsi, la présence de carbone dans l'enveloppe de NiO peut améliorer la collecte des charges et les performances PEC en raison d'une meilleure conductivité du film. Un phénomène similaire a été précédemment observé pour d'autres électrodes d'oxydes métalliques mésoporeux.

La stabilité des dispositifs PEC à photocathodes NiO sensibilisés par des QDs a été mesurée (Figure R6f). Le J_{ph} du dispositif basé sur le NiO nu sensibilisé par des QDs décroît rapidement en 180 s, se réduisant à environ 65% des valeurs initiales, et décroissant encore à environ 40% de la valeur initiale après 7200 s. Pour les photocathodes NiO/C/CdSe QDs, après 2 h, le J_{ph} a diminué à 60,1% de sa valeur initiale. D'autre part, les valeurs de photocourant de NiO/C/CdSe@CdS dans les 180 premières secondes n'ont pas diminué, maintenant 99,61%, de leur valeur initiale. Même après 2 heures de fonctionnement continu, l'échantillon NiO/C/CdSe@CdS a remarquablement conservé plus de 93,2 % de sa valeur initiale.

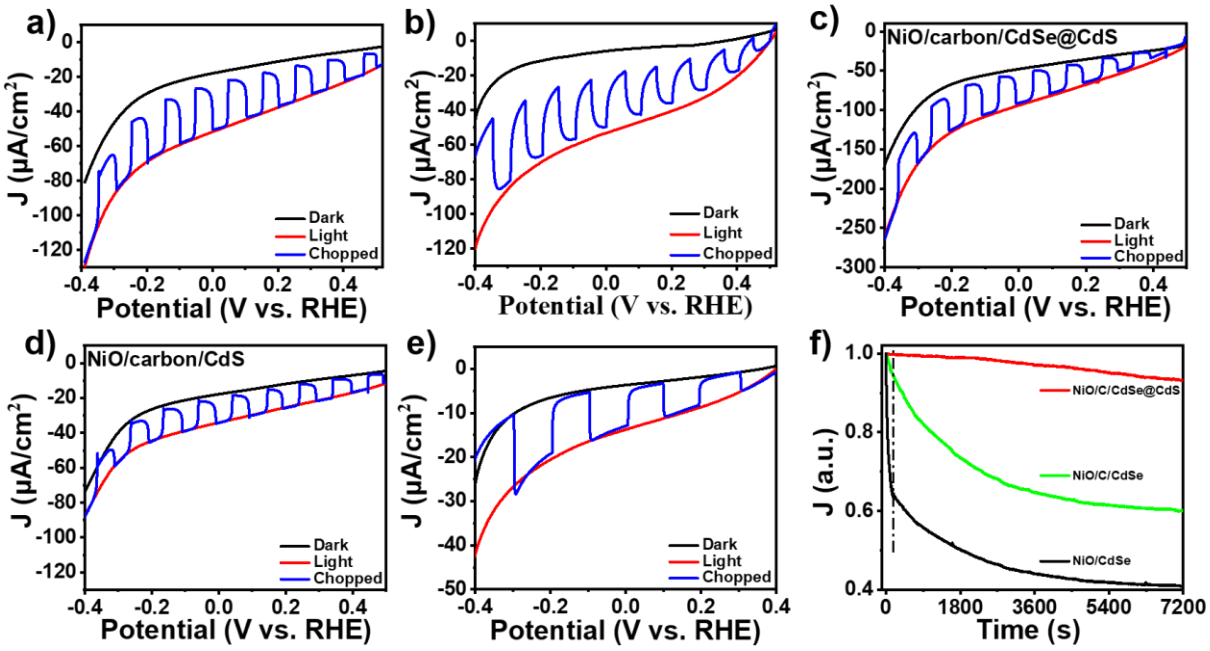

Figure R6 Performance PEC sous éclairage sombre, continu et haché. (a) NiO/C/CdSe avec couche de blocage. (b) NiO/C/CdSe sans couche de blocage. (c) NiO/C/CdSe@CdS. (d) NiO/C/CdS. (e) NiO/CdSe. (f) Mesures de stabilité (chronoampérométrie) de NiO/C sensibilisé par des photoanodes CdSe et CdSe@CdS à 0 V en fonction de RHE sous illumination AM 1,5 G (100 mW/cm^2).

Pour clarifier le mécanisme de fonctionnement des photocathodes NiO/C/QDs et l'effet de la présence d'une matrice de carbone conductrice, nous avons étudié les alignements d'énergie de bande des matériaux par analyse UPS et les caractéristiques de transfert de charge par EIS (Figure R7a et b). Les résultats montrent que l'activité accrue et la stabilité améliorée de la photocathode sont attribuées à une plus grande surface de chargement des sensibilisateurs, à une meilleure diffusion de la lumière et à une matrice de carbone conductrice continue pour faciliter le transfert de charge rapide. Bien qu'il reste de nombreux défis à relever avant de pouvoir les utiliser à grande échelle pour la séparation de l'eau par CEP, les progrès récents devraient inspirer d'autres recherches dans ce domaine et conduire à des architectures de MOF plus avancées pour les applications de conversion énergétique.

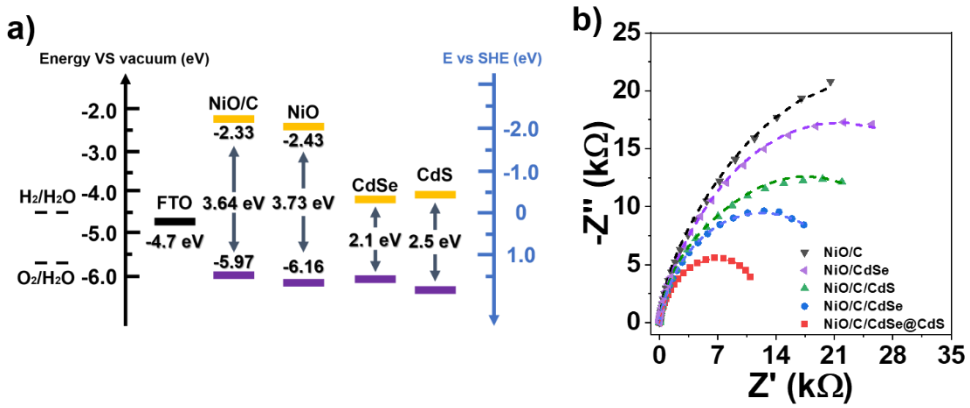

Figure R7 (a) Summary of the energy levels obtained from UPS measurements. (b) Nyquist plots of all samples recorded at 0 V versus RHE under 1 Sun (100 mW/cm^2).

Le chapitre 5 correspond à mon troisième projet. Nous avons développé une synthèse facile d'une jonction p-n à hétérojonction composite In_2O_3/CuO avec une structure creuse en forme de tige hexagonale en utilisant une structure MOF sur MOF comme modèle sacrificiel. En incorporant de petites quantités de nanorubans de graphène, la photoanode a montré une remarquable densité de photocourant et une bonne stabilité. La publication liée à ce chapitre est :

> **L. Shi**, D. Benetti, F. Li, Q. Wei, F. Rosei, MOF-derived In_2O_3/CuO p-n heterojunction photoanode incorporating with graphene nanoribbon for solar hydrogen generation, *Advanced Functional Materials*, submitted.

En raison de l'utilisation de métaux lourds, les QDs constituent toujours un gros problème pour l'environnement. Pour répondre à cette préoccupation et afin d'utiliser l'énergie solaire d'une manière plus respectueuse de l'environnement, sans introduire de matériaux contenant des métaux lourds, une hétérostructure MOF-sur-MOF comme précurseur pour la synthèse du composite MO avec hétérojonction p-n a été développée. La méthode du modèle MOF a été présentée pour obtenir un contact uniforme entre

deux MO simples, mais aussi pour conserver les avantages ci-dessus dans l'hétérojonction MO obtenue. Afin de surmonter l'instabilité électrochimique du CuO, des allotropes de carbone ont été incorporés dans le composite MO.

La procédure de synthèse utilisée pour obtenir un composite In_2O_3/CuO avec la morphologie d'une tige hexagonale creuse est représentée schématiquement dans la Figure R8a. Les morphologies et les caractéristiques structurelles du MIL-68(In)/Cu-BDC et du In_2O_3/CuO ont été caractérisées par SEM et TEM. Comme observé sur la Figure R8b, c et d, le MIL-68(In)/Cu-BDC présente également une morphologie hexagonale en forme de tige avec une surface lisse. Après la calcination dans l'air, le composite In_2O_3/CuO conserve sa forme hexagonale originale et révèle une structure hiérarchique creuse (Figure R8e et f). L'image TEM haute résolution (HRTEM) révèle des franges de réseau de 2,92 Å et 2,52 Å qui peuvent être indexées au plan (222) de In_2O_3 et au plan (110) de CuO, respectivement (Figure R8g). Les images de cartographie élémentaire (figure 2h-l) obtenues en mode STEM indiquent clairement des distributions relativement uniformes des éléments In, Cu, O et C.

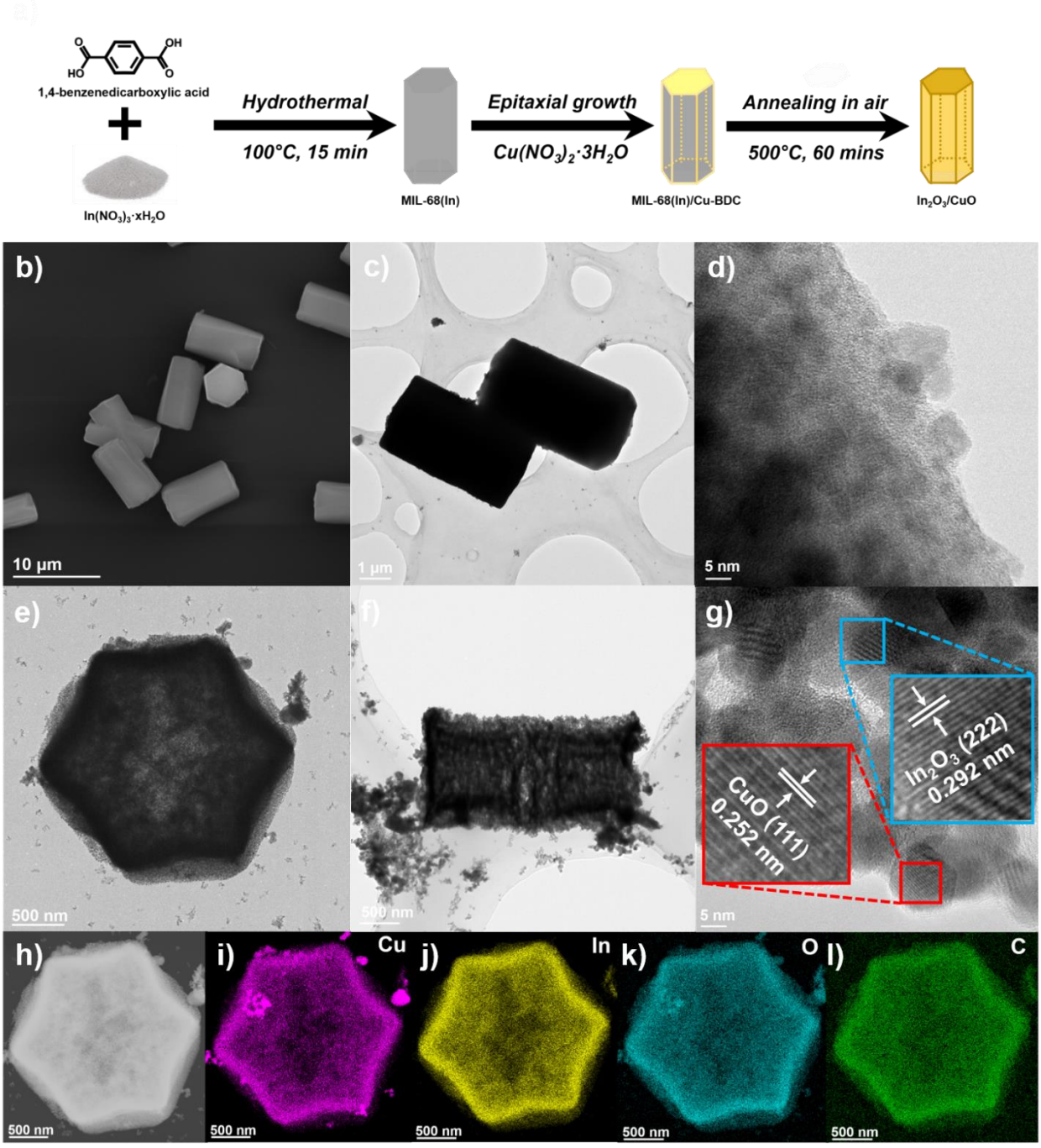

Figure R8 (a) Illustration schématique de la formation des composites In_2O_3/CuO ; images SEM (b) et TEM (c) des précurseurs MIL-68(In)/Cu-BDC. (d) Vue agrandie d'une partie de (c). (e, f) Images TEM de In_2O_3/CuO vues de différentes directions. (g) Image HRTEM de In_2O_3/CuO. (h-l) Image HAADF-STEM et cartographie élémentaire EDX correspondante des éléments In, Cu, O et C pour le composite In_2O_3/CuO.

La mesure des positions des bords de bande de CuO et In_2O_3 et des alignements de bande est importante pour étudier le processus de transfert d'électrons à l'hétérojonction. Les spectres UV-DRS de CuO, In_2O_3 et

In_2O_3/CuO sont présentés dans la Figure R9a. Ils présentent tous une absorption dans la région UV-visible. Selon la formule classique de Tauc, les bandes interdites optiques de l'E_{BG}(CuO) et de l'E_{BG}(In_2O_3) sont respectivement de 1,79 eV et de 2,70 eV (Figure R9b). L'UPS a été utilisé pour estimer le niveau de Fermi (E_F) et le niveau d'énergie maximal de la bande de valence (VBM). La combinaison des informations recueillies lors des spectres XPS et UV-DRS indique que pour le nanocomposite In_2O_3/CuO, ΔE_{VBO} = 1,03 eV et ΔE_{CBO} = 0,12 eV. Comme le montrent les figures R9c et d, la flexion de bande associée a été mise en évidence, et une hétérostructure d'alignement de bande de type II (décalée) a été construite avec succès, dont la bande de conduction hautement énergétique favorise la réduction de H_2 par les électrons photogénérés.

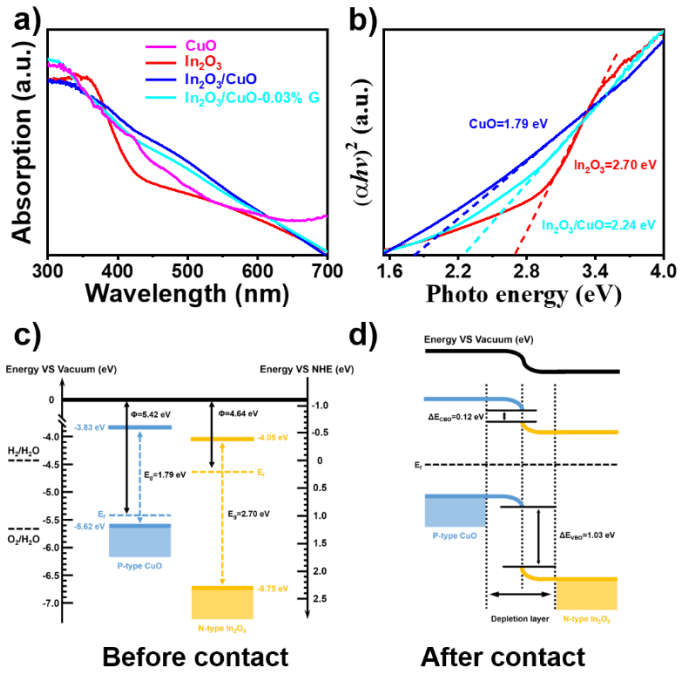

Figure R9 (a) Spectres UV-DRS de CuO, In_2O_3, composite In_2O_3/CuO et In_2O_3/CuO-0,03% en poids de GNRs. (b) Extrapolation des tracés de Tauc ($(\alpha h\nu)^2$ en fonction de l'énergie photonique ($h\nu$)) pour CuO, In_2O_3 et composite In_2O_3/CuO. Diagrammes de bandes d'énergie pour (c) CuO et In_2O_3 avant contact et (d) l'alignement des bandes d'énergie de l'hétérojonction CuO/In_2O_3.

Les mesures de LSV sur les différentes concentrations de GNRs et la photoanode In_2O_3/CuO comme référence sont rapportées dans la Figure R10. Tous les échantillons présentent de faibles densités de courant d'obscurité, ce qui indique que les photocatalyseurs sont presque inactifs sans irradiation lumineuse. En outre, la réponse instantanée du photocourant à l'illumination coupée indique une séparation efficace des paires électron-trou dans le système induite par la lumière visible. La densité de photocourant (J_{ph}) pour tous les échantillons augmente progressivement avec l'augmentation de la concentration de GNRs dans le composite In_2O_3/CuO au début. La figure R10g résume la variation des valeurs de densité de photocourant

saturé en fonction de la concentration de GNRs dans la photoanode In_2O_3/CuO à 1,6 V RHE. Afin d'observer l'influence du CuO sur les propriétés de la photoanode, la même expérience a également été réalisée en préparant un film d'In_2O_3 pur via la méthode du modèle MOF (Figure R10h). Enfin, le tracé comparatif du LSV de l'In_2O_3 pur, de l'In_2O_3/CuO et de l'In_2O_3/CuO-0,03 % en poids de GNR est présenté dans la Figure R10i et les données d'illumination hachée sont également présentées dans la Figure R10j. La densité de photocourant limite des GNR In_2O_3/CuO-0.03% en poids est ~4,03 et 0,7 fois plus élevée que celles de l'In_2O_3 pur et de l'In_2O_3/CuO, respectivement. Par conséquent, l'In_2O_3/CuO-0,03 % en poids de GNRs est considéré comme la meilleure photoélectrode dans la séparation de l'eau PEC. Il est vérifié que l'incorporation de CuO dans In_2O_3 peut former une jonction p-n, ce qui peut améliorer l'efficacité des paires électron-trou photogénérées, faciliter la migration des porteurs et supprimer la recombinaison des charges.

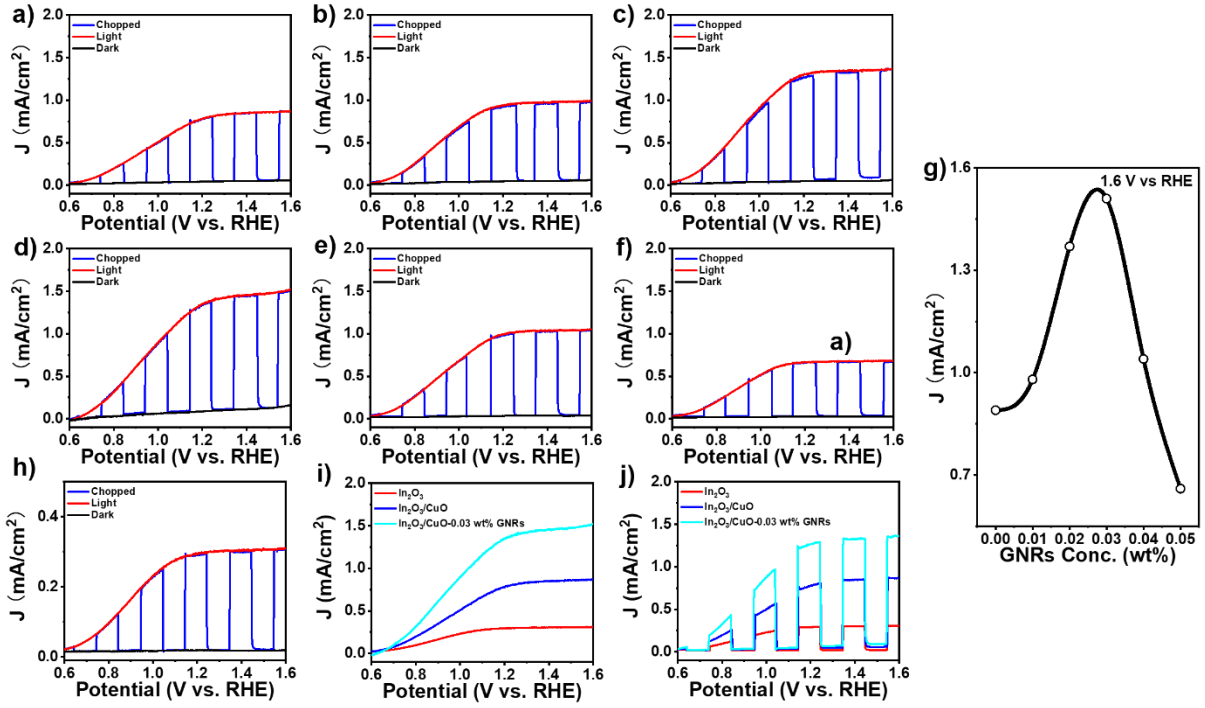

Figure R10 Photocurrent density-potential curves of PEC devices based on In_2O_3/CuO-GNRs hybrid photoanodes with different concentrations of GNRs under dark, continuous and chopped illumination (AM 1,5G, 100 mW cm^{-2}): (a) 0,00 wt%;(b) 0,01 wt%; (c) 0,02 wt%; (d) 0,03 wt%; (e) 0,04 wt% and (f) 0,05 wt%. (g) Variation of current density at 1,6 V vs. RHE under 100 mW cm^{-2} illumination with the concentration of GNRs. Photocurrent density of (h) In_2O_3. (i) Comparative LSV curve of bare In_2O_3, In_2O_3/CuO, and In_2O_3/CuO-0,03 wt% GNRs. (j) chopped illumination of bare In_2O_3, In_2O_3/CuO, and In_2O_3/CuO-0,03 wt% GNRs.

Des études structurelles ont confirmé que le In_2O_3/CuO a conservé la morphologie MOF. En formant l'hétérojonction p-n, la photo-anode In_2O_3/CuO a montré une densité de courant accrue de 196%, par rapport à la photo-anode In_2O_3 pure. Ceci est principalement attribué à l'efficacité de séparation améliorée des paires

électron-trou photogénérées dans la photo-anode In_2O_3/CuO. D'autre part, une concentration optimisée de GNRs dans une photo-anode In_2O_3/CuO a donné la densité de photocourant la plus élevée de 1,51 mA cm^{-2}, ce qui est 70% plus élevé que les photo-anodes In_2O_3/CuO. Cela montre qu'une concentration optimale de GNRs dans la photo-anode In_2O_3/CuO améliore le transport des électrons (en réduisant le R_{ct}), grâce au chemin directionnel des GNRs pour les électrons photo-injectés vers le FTO, sans affecter les propriétés optiques/structurelles, comme l'indiquent l'EIS et l'UV-DRS. Ces résultats fournissent des indications fondamentales sur le fait que les nanostructures d'oxydes métalliques dérivées de MOF offrent des performances prometteuses en tant que matériaux photoélectrodes pour la production d'hydrogène PEC.

Conclusions

Le chapitre 6 résume brièvement les principales conclusions et évoque les défis et perspectives futurs dans ce domaine.